Borohydride, a Next-Generation Material for Energy Storage and Conversion, and the First Description of a Borohydride / Dichromate Fuel Cell

A Dissertation

Presented to the Faculty of the Graduate School

of Cornell University

In Partial Fulfillment of the Requirements for the Degree of

Doctor of Philosophy

by

David Alan Finkelstein

August 2011

Borohydride, a Next-Generation Material for Energy Storage and Conversion, and the First Description of a Borohydride / Dichromate Fuel Cell

David Alan Finkelstein, Ph. D.

Cornell University 2011

Borohydride (BH_4^-), a promising new fuel for fuel cell applications, is rigorously analyzed and explored in the context of a membraneless, microfluidic fuel cell. Though MeOH and H_2 have been studied much more thoroughly than BH_4^-, BH_4^- possesses important advantages relative to these more common fuels. Due to a faster reaction rate, BH_4^- offers over 200 times the current density per mole achievable with MeOH. With a room temperature solubility 90 times higher than H_2 at 3000 psi, BH_4^- has a theoretical maximum current density 170 times that of pressurized H_2. BH_4^-'s main drawback is a hydrolytic decomposition to H_2, which occurs in bulk solution and at Pt surfaces. We describe a low-potential (high voltage), hydrolysis-free oxidation mechanism at Pt, while hydrolysis-prone, low-voltage oxidation is described for Au, in direct contrast to prevailing opinions in the literature. BH_4^- oxidation is described for the first time, for modern literature, in nonaqueous solvents, where bulk hydrolysis is eliminated, but oxidative activity detrimentally affected. To balance BH_4^-'s tremendous current, common oxidants alternative to O_2 are examined, and none found to be suitable. The high-voltage, side-reaction free reduction of cerium ammonium nitrate (CAN) is employed to develop a fuel cell with the highest Pt utilization yet recorded for a non-H_2 fuel cell, and which exceeds the Pt utilization of a typical H_2 fuel cell by 50%. This is achieved at room temperature with a fuel concentration of 0.15 M, which represents only 1% of BH_4^-'s solubility in aqueous

solution. From an array of unconventional fuel cell oxidants, dichromate ($Cr_2O_7^{2-}$) is characterized, and found to deliver an order of magnitude more current than CAN at a small cost to fuel cell voltage. Preliminary results indicate that a BH_4^- / $Cr_2O_7^{2-}$ fuel cell may deliver five times the power density of the BH_4^- / CAN system. For the first time, poisoning mechanisms for BH_4^- at Pt and Au catalysts are described, and an *in-situ* cleaning method developed, which is demonstrated to operate in a BH_4^- / $Cr_2O_7^{2-}$ fuel cell for >7 hours. Finally, oxidative activity for BH_4^- and reductive activity for $Cr_2O_7^{2-}$ are demonstrated at catalysts of significantly lower cost than Pt or Au, including Pd, Ag, and Ni, providing an important cost flexibility for the BH_4^- / $Cr_2O_7^{2-}$ fuel cell that is often unachievable for conventional H_2 / O_2 and MeOH fuel cells.

Biographical Sketch

David Finkelstein has worked and studied in the areas of alternative energy and environmental engineering for over 10 years. He received his B.S. in Biological and Environmental Engineering Technology and Biology from Cornell in 2002. For his undergraduate research, he designed a microbial biofilter for methane-producing, plug-flow digesters with Dr. Norman Scott and Dr. Jean Hunter. He also implemented a project in fluvial geomorphology for streambank restoration with Dr. Jose Lozano of the City of Ithaca Environmental Laboratories. His interests turned to energy exclusively, and he pursued microbial fuel cells for his first M.S. (Professional) in Industrial Microbiology at Michigan State with Dr. J. Gregory Zeikus, collaborating with Dr. Leonard Tender of the Naval Research Lab. He later worked in solar energy for his second M.S. in Biophysics by designing artificial proteins for Pt-free H_2 production, studying at the University of Pennsylvania with Dr. P. Leslie Dutton. Finally, desiring to work on nearer-term technologies, he joined the Cornell Fuel Cell Institute (CFCI), now the Energy Materials Center at Cornell (emc^2), to pursue membraneless, microfluidic fuel cells with Dr. Héctor Abruña in the Department of Chemistry, collaborating with Dr. Abraham Stroock of the Department of Chemical Engineering.

In addition to his interests in alternative energy, David maintains a hobby of political awareness, for without the right governmental climate, energy technology becomes trivialized, rather than cultivated, and never effects the change intended by its designers.

Dedication

This Thesis is dedicated to Dr. Leonard Tender of the Naval Research Laboratory, known as "Lenny" not only to his friends, but to essentially everyone he's ever met. Lenny provides a kind and supportive environment to his research team, assisting those in need with what limited time he has, and treating everyone with the same respect he gives to the Congressional lawyers and military brass that provide much of his funding. He expects the best from his staff, but that's because he gives them his best every day, genuinely listening to their concerns and taking their suggestions, while dispensing expert advice in a stress-free atmosphere. Lenny is driven by a passion to do quality research that has an impact on society, and he insists, in his characteristic nonaggressive way, that his team members enjoy their time in the process.

I am personally indebted to Lenny for promoting both my career as an energy scientist and my first paper, on which he served as a co-principal investigator. He helped to inspire my interest for electrochemistry and set a standard for how to treat the people that one depends on, which has been enormously helpful in working with the six undergraduate students that I have mentored during my Ph.D. program.

Acknowledgments

This work was supported by the Office of Basic Energy Sciences, Division of Materials Sciences, U.S. Department of Energy, under Grant DE-FG02-05ER46250.

This work was additionally supported by the Cornell Center for Materials Research (CCMR) with funding from the Materials Research Science and Engineering Center program of the National Science Foundation (NSF) (cooperative agreement DMR 0520404). The NSF Research Education for Undergraduates program, administered through the CCMR, provided funding for Kenneth Hernandez-Burgos, David Jones, Claudia Rodriguez, Lori Sandberg, and David Watts, who each made significant contribution to the work presented.

The research presented was performed in the laboratory of Prof. Héctor Abruña, with Prof. Abraham Stroock serving as a collaborator. Dr. Jamie Cohen, Dr. Nicolas Da Mota, Dr. Joseph Kirtland, and Corey Letcher provided key support and contribution, as noted in the relevant chapters.

I would like to thank Prof. Abruña for providing an excellent research atmosphere. He regularly attracts top talent, and personalities, from around the world. At a time when I was disenchanted with research science, having completed two graduate programs with few publications to show for the effort, Prof. Abruña took a chance on me, and gave me the green light for my third endeavor in energy research. He has allowed me exceptional independence in steering my project, and with his guidance, I have learned a great deal about science management, from the art of grant writing to the politics of peer review. Should I continue my career in electrochemistry, I will owe much of its foundation to him.

Prof. Stroock has also played a critical role in my graduate studies. He provided endless support and enthusiasm for the project, acting on team concerns to continually improve the quality of our research, and translated industry goals into specific research objectives. Through his expertise in materials transport, he legitimized our efforts to develop a functional fuel cell.

Though Prof. DiSalvo is one of the busiest professors in the Department of Chemistry and Chemical Biology, he has always made time to meet with students. He has provided me with a kind sounding board for new ideas, and encouraged me to consider the underlying chemical properties behind electrocatalysis. Through his efforts as a co-leader of intergroup meetings for the Cornell Fuel Cell Institute and its successor, the Energy Materials Center at Cornell, I have had the opportunity to meet with many of the leading experts in fuel cell and battery technology.

I would also like to thank the many people at the Abruña lab who created a friendly and supportive atmosphere, which made each day at work that much more enjoyable and relaxing. Various lab members, such as Dr. Nicolas Da Mota and Dr. Yasuyuki Kiya, also taught me some of the advanced electrochemistry that later became integral to understanding and establishing unique fuel cell chemistries. I greatly appreciate the work put in by my many undergraduate students over the years, as their work at the bench freed my time to publish our findings and maintain our funding.

Table of Contents

Chapter 1: Introduction to BH_4^- and Membraneless (Laminar-Flow) Fuel Cells

The borohydride BH_4^- fuel cell represents an important new energy conversion technology that addresses concerns of energy storage, fuel activity, and catalyst cost, while the laminar-flow fuel cell circumvents one of the major obstacles of low-temperature fuel cells, that being the proton exchange membrane. Since introductions are provided individually in each of the following chapters, this general introduction will be kept brief, and serves primarily to introduce the reader to nature of BH_4^- as a fuel, and the trademark membraneless, dual electrolyte fuel cell design used in the laboratories of Dr. Héctor Abruña and Dr. Abraham Stroock.

1.1 Membraneless Fuel Cells

The proton exchange membrane, or polymer electrolyte membrane (PEM) of low-temperature fuel cells is near-universally made of Nafion©, an expensive polymer manufactured by DuPont, Inc. Nafion is so pricy that it often outranks Pt as the most expensive component of PEM fuel cells.[1] Despite its cost, Nafion is far from an ideal separator, allowing crossover of fuels such as MeOH, which can result in cathode poisoning. It also dehydrates at common fuel cell operation temperatures, and requires fuel and oxidant streams kept at strict hydration levels to function. Elimination of the membrane solves many of these drawbacks to typical fuel cells.

Microfluidic fuel cells are able to operate without a membrane by employing laminar flow of liquids, in which layers of solution slip past one another without mixing by convection

(Figure 1.1.1). This occurs when the Reynolds number, a dimensionless ratio of geometric parameters, for the fuel cell channel is lower than 1000. Solutes in the anolyte and catholyte can still mix by diffusion, and this is in fact required for fuel cell operation, as ions must cross between these solutions to maintain charge balance during flow of current.

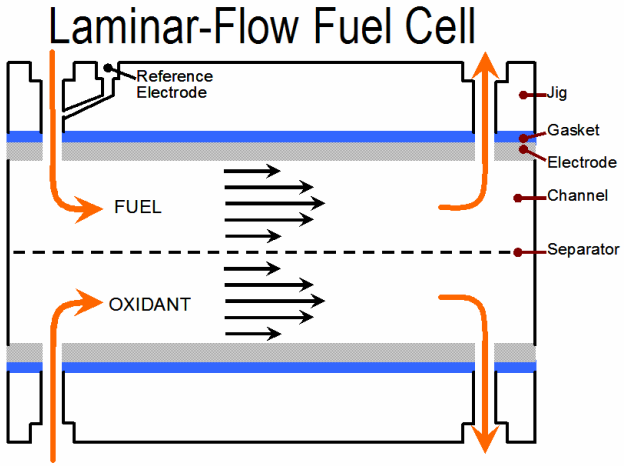

Figure 1.1.1: Schematic of laminar-flow fuel cell. Black arrows represent vector fluid flows, with longer tails indicating greater magnitude of flow. Flow patterns follow the typical parabolic flow in a duct.

Unlike an acidic or alkaline fuel cell membrane, the hydrodynamic boundary in a laminar flow fuel cell is completely pH-insensitive, without explicit need for H^+ or OH^- to be present in abundance to maintain conductivity. Thus, dual electrolytes at separate pH's can be implemented in this design. This allows the fuel to be dissolved in base, lowering its potential via the Nernst equation,[2] while the oxidant can be dissolved in acid to raise its potential. Assuming a 59 mV change in potential for each pH unit, a pH 0 / 14 fuel cell is expected to generate an extra 0.84 V from the pH gradient, allowing significantly higher voltage than the 1.2 V voltage window

typically ascribed to aqueous electrolyte. This type of system has been developed and described previously by the Abruña group.[3]

While the laminar flow design offers many advantages, it cannot take advantage of gaseous transport of fuel or oxidant. Both must be fully dissolved in electrolyte at all times, and solubility in aqueous solution quickly becomes an important determinant of maximum current density. Both H_2 and O_2 have solubilities on the order of 1 mM in water at room temperature, and are therefore expected to have minimal performance in such a fuel cell. Fuels like MeOH and BH_4^- have aqueous solubilities >10 M,[4] and are therefore fundamentally much better suited to laminar-flow fuel cells than H_2.

1.2 Employment of BH_4^- in Fuel Cells

BH_4^- has long been a common reduction reagent in organic synthesis, but has only in recent years been seriously considered as a fuel for fuel cells.[5] $NaBH_4$ has considerable solubility in aqueous solutions (>14 M), a high electron recovery per molecule ($8e^-$, Reaction [1.2.a]), a very low potential for oxidation in base (–1.44 V vs. Ag/AgCl), and extremely fast kinetics at room temperature. These traits make BH_4^- an ideal fuel for laminar-flow fuel cell systems.

$$BH_4^- + 8OH^- \leftrightarrows 8e^- + H_2BO_3^- + 5H_2O \qquad \textbf{[1.2.a]}$$

BH_4^- has approximately the same low onset potential for oxidation as H_2, allowing for high voltage systems. However, because of its very high solubility, about 17,500 times that of H_2 (0.75 mM), and four times higher electron content per mole (8 vs. 2 e^-), its theoretical

maximum current density (via Levich analysis) is about five orders of magnitude greater. Such high current densities may be unattainable, as saturation of catalyst active sites may occur, but achieving even a fraction of this current would significantly increase Pt utilization and potentially decrease fuel cell cost.

$NaBH_4$ also has significant specific and volumetric energy density (9.4 kWh/kg, 10 kWh/L for combustion with O_2; see Table 1.2.1 for a comparison of BH_4^- with other energy technologies), exceeding the values for MeOH (6.1 kWh/kg, 4.8 kWh/L). While MeOH, which can provide up to $6e^-$ at –0.4 V vs. Ag/AgCl in base, appears similar to $NaBH_4$ based on these thermodynamic, theoretical measures, a comparison of activity yields a very different conclusion. Figure 1.2.1 shows RDE voltammograms for the room-temperature oxidation of $NaBH_4$ and MeOH at their best known catalysts, Pt and PtRu, respectively. $NaBH_4$ exhibits a current density *200 times greater* than MeOH, producing 10 times the current at 20 times lower concentration, and deliver 0.5 A/cm^2 at a concentration of just 50 mM (Figure 1.2.2). Thus, it is clear that thermodynamics alone cannot predict the activity of a fuel, and that $NaBH_4$ represents a significantly more power-dense fuel than either H_2 or MeOH. In addition to power, BH_4^- also represents an excellent energy storage material as a dry salt, rivaling even a Li ion primary battery, and greatly exceeding Li ion secondary batteries, which require inactive intercalation materials (i.e., graphite) for operation.[5-7]

Fuel	E^0 (V)	Energy Density (kWh/kg)	Energy Density (kWh/L)
$NaBH_4$	-1.2	9.4	5.2
MeOH	-0.6	6.1	4.8
H_2	-0.8	33	0.003
Li Ion	-3	0.6	0.6
Li Primary	-3	9.7-13.5	5.2-7.2

Table 1.2.1: Comparison of gravimetric and volumetric energy density of select energy conversion technologies.

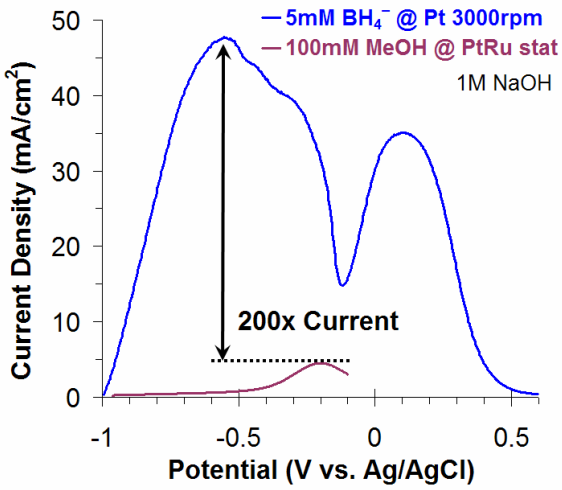

Figure 1.2.1: Comparison of 5 mM BH_4^- vs. 100 mM MeOH, both in 1 M NaOH.

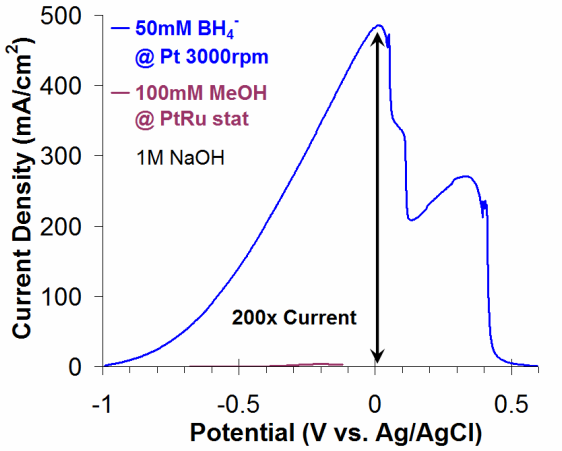

Figure 1.2.2: Comparison of 50 mM BH_4^- vs. 100 mM MeOH, both in 1 M NaOH.

Though BH_4^- has many attractive features as a fuel, its utilization is hindered by its deleterious hydrolysis reaction, which decomposes the fuel to H_2 and boric acid (Reaction [1.2.b]).[8,9] Hydrolysis can proceed partially or completely, converting any number of BH_4^-'s eight reducing equivalents to H_2 or partial fractions thereof. Hydrolysis occurs readily in bulk solution, in both acidic and neutral aqueous environments, as well as at the surfaces of various catalysts. Hydrolytic decomposition at electrode surfaces is especially detrimental, as H_2 bubbles block electrodes for further reaction, decreasing the effective surface area of fuel cell catalysts, and disrupt laminar flow across the electrode. Once H_2 is formed, the solubility of the reducing equivalents dramatically decreases, eliminating one of BH_4^-'s principal advantages as a fuel. Thus, hydrolysis must be avoided in BH_4^- fuel cell technologies.

$$BH_4^- + H^+ + 2H_2O \rightarrow HBO_2 + 4H_2 \qquad \textbf{[1.2.b]}$$

1.3 Summary of Chapter Contents

Chapter 2 provides an extensive discussion of rotating disk electrode (RDE) techniques for electrochemical analysis of redox reaction mechanisms. Rather than simply reviewing techniques in Bard & Faulkner, this chapter provides an experimentalist's point of view on implementing theory at the benchtop, and provides suggestions on obtaining accurate, precise data from complex systems.

Chapter 3 looks at the oxidation mechanism of BH_4^- and its first hydrolytic decomposition product, BH_3OH^-, at Pt and Au in great detail, with the aim of discerning the most effect means of utilizing BH_4^- in a fuel cell. Also discussed is poisoning of BH_4^- at Pt and

Au, and a method based on an analytical understanding of BH_4^-'s oxidation mechanism is developed for poison removal. Finally, alternative, less expensive catalysts, such as Ru, Ir, Pd, Ag, and Ni are examined for their oxidative activity toward BH_4^- oxidation.

Chapter 4 examines the oxidation of BH_4^- in nonaqueous solvents. The primary purpose of investigating BH_4^- under such conditions is to avoid its hydrolysis reaction by removing water from the system entirely.

Chapter 5 reviews a host of alternative oxidants found in the literature with the aim of replacing O_2 in a laminar flow fuel cell. Additionally, the oxidant cerium ammonium nitrate (CAN) is described. This oxidant was selected for study by Dr. Nicolas Da Mota, and though far from ideal, provided an important, unique alternative to the common, often troublesome oxidants used in the fuel cell community.

Chapter 6 reviews a series of highly potent oxidants that are uncommon in the fuel cell community. All of these oxidants offer current densities that dwarf that obtainable from CAN, but few are readily employable in a high-voltage fuel cell. The oxidant dichromate ($Cr_2O_7^{2-}$) is described, which provides ten times CAN's current density, faster kinetics, and greatly improved solubility, at a small cost to system voltage.

Chapter 7 describes the performance of a BH_4^- / CAN fuel cell, as well as a unique transport-enhancing flow pattern developed by Dr. Joe Kirtland and Dr. Abraham Stroock. The combination of chemistry and transport results in a fuel cell with better power density and Pt utilization than conventional H_2 or MeOH fuel cells, but lacking in efficiency.

Chapter 8 describes the preliminary performance of a BH_4^- / $Cr_2O_7^{2-}$ fuel cell. Long-term operation using the poison-cleaning method developed in Chapter 3 is investigated. Future directions for research on BH_4^- and laminar-flow fuel cells are suggested.

1.4 References

(1) Kakaç, S.; Pramuanjaroenkij, A.; Vasiliev, L. *Mini-Micro Fuel Cells: Fundamentals and Applications*; Springer: Dordrecht, The Netherlands, 2008.

(2) Bard, A. J.; Faulkner, L. R. *Electrochemical Methods*; 2nd ed.; John Wiley & Sons, Inc.: New York, NY, 2001.

(3) Cohen, J. L.; Volpe, D. J.; Westly, D. A.; Pechenik, A.; Abruña, H. D. *Langmuir* **2005**, *21*, 3544-3550.

(4) *CRC Handbook of Chemistry and Physics*; 86th ed.; Lide, D. R., Ed.; CRC Press: Boca Raton, FL, 2005.

(5) Ma, J.; Choudhury, N. A.; Sahai, Y. *Renewable and Sustainable Energy Reviews* **2010**, *14*, 183-199.

(6) Dillon, R.; Srinivasan, S.; Aricò, A. S.; Antonucci, V. *Journal of Power Sources* **2004**, *127*, 112-126.

(7) Linden, D.; Reddy, T. B.; McGraw-Hill, 2002.

(8) Morris, J. H.; Gysling, H. J.; Reed, D. *Chem. Rev.* **1985**, *85*, 51-76.

(9) Pecsok, R. L. *J. Am. Chem. Soc.* **1953**, *75*, 2862-2864.

Chapter 2: Electroanalytical Methodology

The following chapters present data that were obtained following a strict set of quantitative analyses for rotating disk electrode (RDE) voltammetry. Any deviation from these methods, or unique procedures for a given experimental work, are included within the chapter. The publications resulting from the work in select chapters include summary methods sections. This chapter aims to present a rigorous overview of these methods, but also provide some added clarification and tips for those beginning their training in electrochemistry.

2.1 Electrochemical Setup

Experiments were carried out in a three-chambered electrochemical cell, with compartments separated by medium porosity glass frits, using a Ag/AgCl reference electrode and a Pt-mesh counter electrode. Electrochemical experiments using a modern potentiostat or galvanostat use three electrodes (working, counter, and reference). The counter electrode must be separated from the working electrode; its potential is neither controlled nor readily known, and it generates an unknown quantity and variety of chemical species (such as H_2O_2, H_2, or O_2 in an aqueous electrolyte) that can generate current at the working electrode or contaminate it. Ag/AgCl reference electrodes are very convenient, as they offer a stable potential independent of the pH or solvent (provided the Ag/AgCl wire is encased in a glass electrode containing saturated KCl or NaCl). Minute amounts of Cl^- slowly leak from the porous Vycor© frit (or Abruña lab constructed Kimwipe frit) that will poison a Pt electrode. Separating the Ag/AgCl reference electrode via a separate compartment and a second glass frit provides two barriers to Cl^- diffusion, greatly reducing its concentration in the working electrode compartment. In more

sensitive setups, non-poisoning, pH-dependent reference electrodes must be used, such as NHE/SHE (normal or standard H_2 electrode), RHE (reversible H_2 electrode, like NHE, but with H_2 trapped in a glass electrode encasement), Pd hydride, or even just a Pt wire pseudoreference. A Pt pseudoreference will maintain a steady potential so long as it is NOT flame-polished, since it generally adopts a constant oxide coverage, generating a Pt/PtO_x equilibrium, much like a Ag/AgCl electrode (flame-polishing removes all oxides, and a new oxide layer of unique surface coverage and thickness develops as the Pt cools).

Rotating disk electrode voltammetry was performed using a Pine bipotentiostat (Model AFCBP1) and analytical rotor (Model AFMSRX). Electrodes were rotated between 50 and 3000 rpm, using a generally logarithmic distribution of rotation rates, with additional slower rotation rates selected to obtain more reliable Levich and Koutecký-Levich plots. Many inexperienced research groups will use rotation rates starting at 200 or 500 rpm, and select simple squares numbers, such as 200, 400, 900, 1600, and 2500 rpm. In these experiments, a great deal of valuable data is lost. Lower rotation rates will help reveal coupled chemical processes (EC, CE, ECE, etc.), and a number of lower rotation rates will generate multi-point linear Levich plots. This is especially useful when an electrochemical process is slow, and the Levich plot appears to be kinetically limited at moderate and high rotation rates. The Levich plots including only the lower rotation rates, which exhibit linearity, are still perfectly valuable for analysis (Figure 2.1.1).

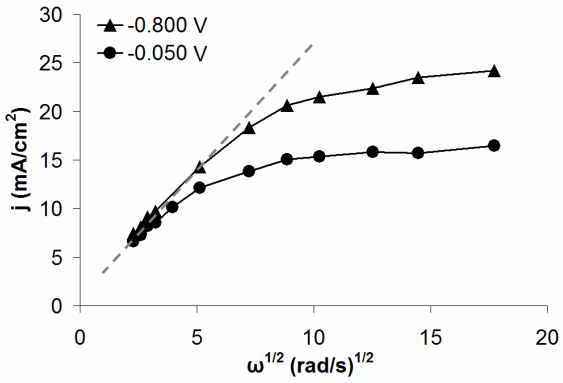

Figure 2.1.1: Levich plot for 5 mM BH_4^- in 1 M NaOH at Pt, sampled at the potentials indicated.

CV's were carried out at 20 mV/s to obtain pseudo steady-state sweeps, decreasing the time for decomposition of reactive fuels and oxidants. Sweep rates of 20 mV/s generally produce steady-state RDE voltammograms that do not differ significantly from those at 5 mV/s. All experiments were run at room temperature and pressure (25°C, 1 atm).

2.2 Electrode Cleaning

The 3 mm Pt rotating disk electrode was polished using 1μm Buehler Metadi diamond paste on a Buehler Microcloth polishing cloth, then electrochemically cleaned from –0.2 to +1.2 V vs. Ag/AgCl in 0.1 M H_2SO_4 until the characteristic voltammetric profile of polycrystalline Pt was obtained (Figure 2.2.1). The 5 mm Au rotating disk electrode was polished using 0.05 μm Buehler Micropolish II, γ-alumina, on a Buehler Microcloth, and electrochemically cleaned from 0.0 to +1.35 V vs. Ag/AgCl in 0.1M H_2SO_4 until the characteristic voltammetric profile of polycrystalline Au was obtained (Figure 2.2.2). Cycling Au higher than +1.35 V, or simply letting it cycle too long, will etch the surface and significantly affect not only Au's

voltammogram in 0.1 M H_2SO_4, but its catalytic properties as well. The 5 mm GC rotating disk electrode was polished using a series of 1 and 0.3 μm α-alumina and 0.05 μm γ-alumina on a Buehler Microcloth, sonicated in 1M NaOH for 15 min, and electrochemically cleaned from –0.2 to +0.8 V vs. Ag/AgCl in 0.1M H_2SO_4 until broad, anodic and cathodic semiquinone peaks at +0.3 V were observed (Figure 2.2.3). It is notable that the capacitances of Pt, Au, and GC vary appreciably.

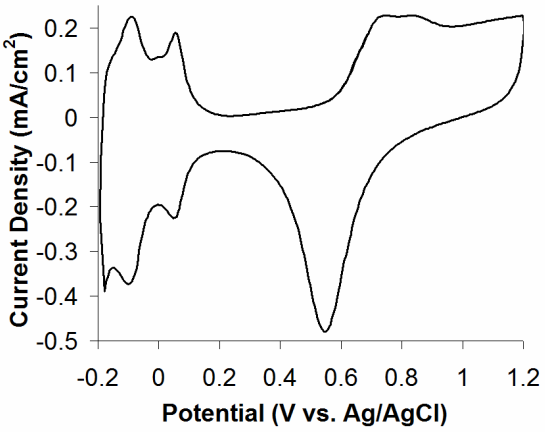

Figure 2.2.1: Stationary CV of a 3 mm Pt RDE in 0.1 M H_2SO_4, 100 mV/s.

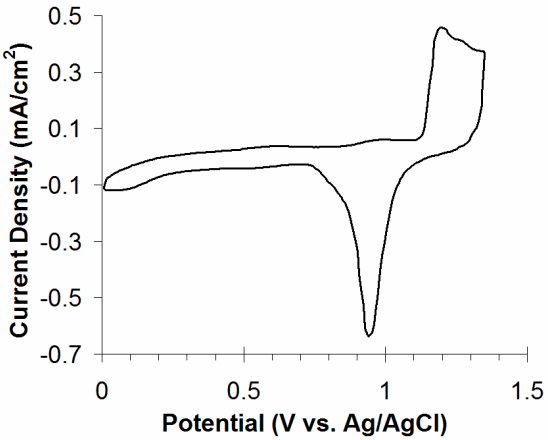

Figure 2.2.2: Stationary CV of a 5 mm Au RDE in 0.1 M H_2SO_4, 100 mV/s.

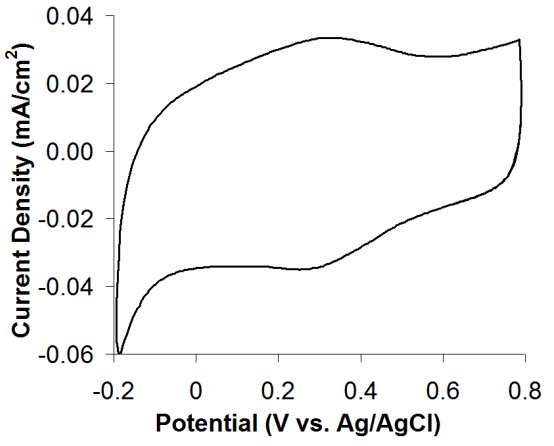

Figure 2.2.3: Stationary CV of a 5 mm GC RDE in 0.1 M H_2SO_4, 100 mV/s.

2.3 Electrochemical Equations

In rotating disk electrode (RDE) voltammetry, the number of electrons involved in an oxidation reaction at a chosen potential can be obtained from the Levich equation (Equation 2.3.1):[1]

$$i_{l,c} = 0.62nFAD_O^{2/3}\omega^{1/2}\nu^{-1/6}C_O^* \qquad \textbf{[2.3.1]}$$

where $i_{l,c}$ is the limiting anodic current (A) at a given rotation rate (ω)

n is the number of e^- transferred

F is Faraday's constant (C/mol)

A is the electrode area (cm^2)

D_O is the diffusion coefficient of the oxidized species (cm^2/s)

ω is the electrode rotation rate (rad/s)

ν is the kinematic solution viscosity (cm^2/s)

C_O^* is the bulk concentration of the oxidized species (mol/cm^3)

The Levich equation is valid when the system is mass-transport limited at all rotation rates used in the calculation, and this is evidenced by linearity in the Levich plot ($i_{l,c}$ vs. $\omega^{1/2}$). Deviations from linearity indicate a kinetic limitation, where the system can be described by the Koutecký-Levich (K-L) equation (Equation 2.3.2):[1]

$$\frac{1}{i} = \frac{1}{i_K} + \frac{1}{i_{l,c}} = \frac{1}{nFAk_f(E)C_O^*} + \frac{1}{0.62nFAD_O^{2/3}\omega^{1/2}\nu^{-1/6}C_O^*} \qquad \textbf{[2.3.2]}$$

$$\text{and } k_f(E) = k^0\exp[-\alpha f(E - E^0)] \qquad \textbf{[2.3.3]}$$

where i_K is the kinetically limited current (A)

k^0 (also as k_s) is the standard heterogeneous charge-transfer rate constant (cm/s)

k_f is the heterogeneous rate constant for reduction (cm/s)

α is the transfer coefficient (dimensionless)

$f = F/RT$ (with R as the universal gas constant, J/(K•mol) and T the temperature, K)

E is the potential sampled for K-L analysis (V)

E^0 is the standard reduction potential (V)

There may exist complications in applying the Butler-Volmer model to a multi-step, multiple-electron transfer reaction,[1] yet it remains a useful tool to describe the current response as a function of potential when RDE analysis shows the electrochemical reaction to be a single wave.

It should be noted that K-L analysis is a non-trivial procedure. Every RDE analysis should begin with analyzing the voltammograms and the Levich plots. If the system is not well-

behaved, or if any coupled chemistry process is evident, a K-L analysis will not readily provide any useful data. Furthermore, Levich plots are superior for obtaining mass-transport parameters. While these parameters appear to be readily available from the slope of a K-L plot, the data are more transformed than in a Levich plot, which magnifies the error in the measurements.

A good K-L analysis requires sampling multiple potentials from RDE data. Quality data will exhibit parallel plots between different sampled potentials (Figure 2.3.1, excluding potentials –0.487 and –0.520 V). This indicates that all mass-transport properties and n have not changed at different potentials, and the only change is in the intercept, reflecting that k_f is changing, as expected from Equation 2.3.3, with the overpotential applied.

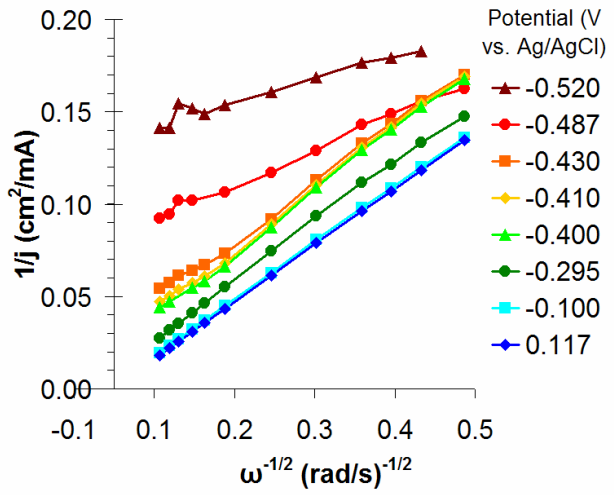

Figure 2.3.1: Koutecky-Levich plots from RDE voltammograms of 5 mM BH_4^- at Au in 1 M NaOH, 25 mV/s, sampled at the potentials indicated.

Values for α were determined from the slope of $\ln[i / (i_{l,c} - i)]$ vs. E plots.[2] Substituting in i from the K-L equation, the expression $\ln[i / (i_{l,c} - i)]$ simplifies to $\ln(i_K / i_{l,c})$, where i_K and $i_{l,c}$ are as described above. Using terms from Equation 2.3.2 and 2.3.3 to substitute in for i_K, we can make the following equality:

$$\ln\left[\frac{i}{(i_{l,c}-i)}\right]=\ln\left(\frac{i_{\mathrm{K}}}{i_{l,\mathrm{c}}}\right)=-\alpha f E+\alpha f E^{0}+\ln\left(\frac{nFAk^{0}C_{\mathrm{O}}^{*}}{i_{l,\mathrm{c}}}\right) \qquad \textbf{[2.3.4]}$$

Thus, the slope of this term vs. E becomes $-\alpha f$ and $\alpha f E^{0} + \ln(nFAk^{0}C_{\mathrm{O}}^{*}/i_{l,\mathrm{c}})$ becomes the intercept.

Generating these plots is extremely time-consuming, and interpreting the plots can become arbitrary. Thus, calculating α has a low efficiency for production of new information, and should only be performed when reproducible RDE voltammograms have already been obtained. That is, it represents the last analytical step of basic RDE analysis, and should not be attempted during early experimental trials. The effort proved strongly worthwhile, as we frequently found that α differed significantly from 0.5, with various oxidants in Chapter 5 having values of 0.2 to 0.8 (Table 5.3.2).

These plots quickly become numerous and were not included in our publications, but they can be found in the appropriate enclosed data disk for a given publication. To ensure accuracy, the plots should be generated at multiple rotation rates. It is often unclear which rotation rates will yield the most linear plots, and if more than one linear region appears, which linear region best reflects the α of interest. For example, the plots for the reduction of cerium ammonium nitrate at GC are relatively uniform, with little difference between slopes at different rotation rates (Figure 2.3.2). In the reduction of MnO_4^- at GC (Figure 2.3.3), curvature is evident at low rotation rate, and lowly disappears toward higher rotation rates. The oxidation of BH_4^- at Au practically exhibits an inflection point that slowly changes potential across rotation rates (Figure 2.3.4). Assessing an accurate slope is not a simple process. It is important to keep in mind that

even determining an approximate value for α is better than not reporting a value at all, as inexperienced electrochemistry groups will gravitate toward an estimation of 0.5 for α, but could be directed otherwise by a single good paper.

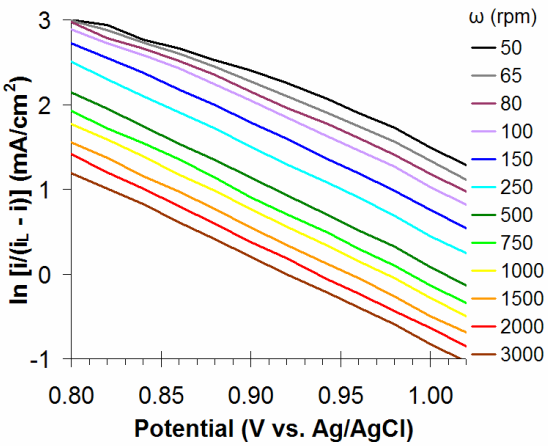

Figure 2.3.2: Plot of $\ln[i / (i_{l,c} - i)]$ vs. E, or $\ln(i_K / i_{l,c})$ vs. E, from RDE voltammograms of 5 mM cerium ammonium nitrate at GC in 1 M HNO_3, 20 mV/s. The potential was sampled every 20 mV in the range of 0.800 to 1.020 V vs. Ag/AgCl.

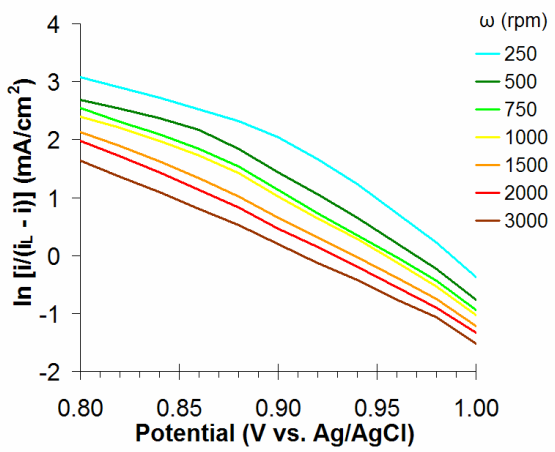

Figure 2.3.3: Plot of ln[i / ($i_{l,c}$ – i)] vs. E, or ln(i_K / $i_{l,c}$) vs. E, from RDE voltammograms of 5 mM MnO_4^- at GC in 0.5 M H_2SO_4, 20 mV/s. The potential was sampled every 20 mV in the range of 0.8 to 1.0 V vs. Ag/AgCl.

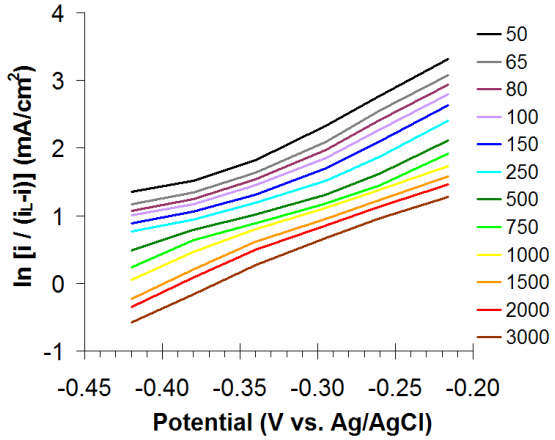

Figure 2.3.4: Plot of ln[i / ($i_{l,c}$ – i)] vs. E, or ln(i_K / $i_{l,c}$) vs. E, from RDE voltammograms of 5 mM BH_4^- at Au in 1 M NaOH, 25 mV/s. The potential was sampled every 20 mV in the range of –0.42 to –0.22 V vs. Ag/AgCl.

As a final suggestion, it is best to take the absolute value of the slope for these plots when calculating α. Determining a negative value for α is usually a sign of an error of convention in

whether anodic current is positive or negative, rather than a mistake in calculation.

In our experience working with fuel cells, which often rely on highly irreversible reactions with large values of *n*, we have found thermodynamic values of E^0 to be of little use in predicting the behavior of fuels and oxidants. Yet the reactions still exhibit exponential dependency of current on potential, reminiscent of Butler-Volmer kinetic behavior. To provide practical parameters that allow prediction of complex electrochemical reactions, we have substituted onset potentials for oxidation (E_{onset}) for E^0, and this value along with α are used to calculate effective values of k^0, or k^0_{eff}. While these terms differ significantly from a rigorous treatment of the Butler-Volmer model, we feel that they will have a higher utility for fuel cell and battery research.

2.4 References

(1) Bard, A. J.; Faulkner, L. R. *Electrochemical Methods*; 2nd ed.; John Wiley & Sons, Inc.: New York, NY, 2001.

(2) Kiekens, P.; Steen, L.; Donche, H.; Temmerman, E. *Electrochim. Acta* **1981**, *26*, 841-845.

Chapter 3: Rotating disk electrode (RDE) Investigation of BH_4^- and BH_3OH^- Electro-oxidation at Pt and Au: Implications for BH_4^- Fuel Cells

Publication: **2009** *J. Phys. Chem. C.*, *113*, 19700-19712

Personnel: David A. Finkelstein, Nicolas Da Mota, Jamie L. Cohen, Héctor D. Abruña.

Department of Chemistry and Chemical Biology, Baker Laboratory,
Cornell University, Ithaca, New York 14853-1301

We present a thorough electrochemical study of the mechanism of borohydride oxidation on gold and platinum surfaces via cyclic voltammetry and rotating disk and ring-disk electrode voltammetry. We have paid particularly close attention to the number of electrons transferred (from a theoretical maximum of $8e^-$), values of the heterogeneous charge transfer rate constant (k_b), the presence of coupled chemical reactions, and adsorbed intermediates. We find that the nature of the electrode (Pt, Au) plays an important role in all of these processes and we present a detailed mechanistic analysis in light of the above mentioned results. Our study suggests that Pt will significantly outperform Au for a direct borohydride fuel cell, providing similar electron recovery at much lower anode potentials.

3.1 BH_4^- Oxidation at Pt and Au Introduction

Borohydride is currently of great interest[1-8] for use as a fuel in fuel cells because of its theoretical capacity to deliver up to 8 e^- / molecule at very low-potential[9] (E^0 = –1.24V vs. NHE), which could generate high power with small quantities of fuel. Borohydride can also

quickly hydrolyze to H_2 at low and moderate pHs [10], and has therefore found interest as a hydrogen storage agent[11-15].

Unfortunately, these promising characteristics have yet to be fully realized in practice. Borohydride's reported E^0 value of –1.24V vs. NHE is essentially a thermodynamic construct[16] based on the combination of a series of reactions, including proton reduction and $NaBH_4$ dissociation, and has limited, if any, predictive value for how BH_4^- will behave at noble (or other) metal electrodes[17]. At these surfaces, BH_4^-'s potential in aqueous electrolyte, much like methanol and hydrazine, is largely governed by ionization of adsorbed surface hydrogen abstracted from BH_4^- following the adsorption of BH_4^- to the electrode[18]:

$$BH_4^- + Pt \leftrightarrows Pt—BH_3 + H^+ + 2e^- \qquad \textbf{[3.1.a]}$$

In fact, electrodes that are inactive for hydrogen ionization, including Cu, Ni, and graphite, do not oxidize BH_4^- until the electrode potential almost reaches that of O_2 evolution[17,19]. Thus, the effective potential for borohydride oxidation that is practical to fuel cell development will depend on the catalytic and surface properties of the electrode employed.

Similarly, the $8e^-$ / molecule available from BH_4^- is an ideal upper limit of current-carrying power, and does not take into consideration the multitude of possible reaction pathways. For example, at Pt surfaces, the oxidation reaction is complicated by the catalytic hydrolysis of BH_4^- to BH_3OH^- and H_2, which proceeds even at pH 14[17]. The oxidation of BH_3OH^- is thought to occur at potentials more negative than BH_4^- itself[19-21], while BH_4^- appears to exhibit an open-circuit potential more negative than H_2 at Pt[17,22]. Borohydride oxidation at Pt involves these CE-

type reactions[23] (chemical hydrolysis followed by electrochemical oxidation) as well as the direct oxidation of BH_4^- [24]:

The CE mechanisms of BH_4^- at Pt[24-26]:

$$(C)\ BH_4^- + H_2O \rightarrow BH_3OH^- + H_2 \qquad \textbf{[3.1.b]}$$

Followed by

$$(E)\ H_2 + 2OH^- \rightarrow 2H_2O + 2e^- \qquad \textbf{[3.1.c]}$$

and

$$(E)\ BH_3OH^- + 3OH^- \rightarrow BO_2^- + 3/2\ H_2 + 2H_2O + 3e^- \qquad \textbf{[3.1.d]}$$

The complete oxidations of BH_4^- to $H_2BO_3^-$ [17] or BO_2^- and BH_3OH^- to $B(OH)_4^-$ [25,27,28] follow stepwise mechanisms in which intermediates can either be hydrolyzed to H_2 or electrochemically oxidized, resulting is a varying number of electrons obtained from each original molecule of BH_4^-. Gyenge[24] has proposed that the oxidation pathways taken may depend on the surface adsorption of both BH_4^- and various reaction intermediates. A review of alternate pathways can be found in Morris et al.[19], and the pathways presented have been speculated upon in recent work.[1,22,29]. Summaries of proposed direct oxidations of BH_4^- at Pt ([3.1.e][25], [3.1.e][17]) are presented below.

$$BH_4^- + 8OH^- \rightarrow BO_2^- + 6H_2O + 8e^- \qquad \textbf{[3.1.e]}$$

$$BH_4^- + OH^- + 2H_2O \rightarrow H_2BO_3^- + 2H_2 + 3H^+ + 4e^- \qquad \textbf{[3.1.f]}$$

The oxidation pathways of BH_4^- at Au electrodes are likewise complex, although the reactions may be somewhat simplified since early reports indicated that Au did not catalyze BH_4^- hydrolysis[20,24]. At Au, the first stages of BH_4^- oxidation were proposed to follow an ECE reaction mechanism[20] (Reactions [3.1.g]-[3.1.i]):

$$(E)\ BH_4^- \leftrightarrows BH_4^\bullet + e^- \qquad \textbf{[3.1.g]}$$

$$(C)\ BH_4^\bullet + OH^- \leftrightarrows BH_3^- + H_2O\ (\text{very fast}) \qquad \textbf{[3.1.h]}$$

$$(E)\ BH_3^- \leftrightarrows BH_3 + e^- \qquad \textbf{[3.1.i]}$$

In cyclic voltammetric (CV) studies, Mirkin and Bard found a nonlinear i_p vs. $v^{1/2}$ plot, suggesting that the oxidation steps follow a complex reaction mechanism[30]. Subsequently, using fast CV techniques (v = 10 to 2000V/s), Mirkin et al. found an intricate $i_p/v^{1/2}$ vs. $v^{1/2}$ plot: At lower scan rates, the plot matched a theoretical prediction for an EC reaction mechanism, while at higher scan rates, it showed a strong linear trend (that is, $i_p \propto v$), indicating surface adsorption of reactants or reaction intermediates[20].

Despite a great deal of work and attention, the mechanism of BH_4^- oxidation at Au and Pt surfaces remains unresolved. In this manuscript, we attempt to gain a deeper understanding of the reaction mechanisms at play in BH_4^- oxidation at Pt and Au electrodes and provide insight into potential electrocatalyst choice for direct BH_4^- fuel cells. We have employed rotating disk electrode voltammetry to examine the number of electrons exchanged in the various oxidation steps, the kinetic rates of these reactions, and whether coupled-chemistry events are involved[23]. The first hydrolysis and oxidation product of BH_4^-, BH_3OH^-, was also studied to determine its

role in the oxidation pathways of BH_4^- and to consider the nature of the hydrolysis reactions. Finally, ramifications for BH_4^- fuel cells using Au and Pt anodes are discussed.

3.2 Experimental Methods

3.2.1 Reagents

All chemicals used were reagent grade, and included sodium hydroxide (Mallinckrodt Chemicals), sodium borohydride (Morton International), dimethylamine borane (Strem Chemicals), and high-purity (99.999%) sulfuric acid (Sigma-Aldrich). All solutions were prepared with deionized water purified with a Hydro purification system connected in series to a Millipore Milli-Q system (18 MΩ·cm).

3.2.2 Solutions Preparation

Solutions of sodium borohydride and sodium hydroxide were prepared by first dissolving sodium hydroxide in the full solution volume, allowing the solution to cool to room temperature, and deaerating the solution with nitrogen gas. Sodium borohydride was then added and the solution was mixed by gentle inversion. Further purging of the solution was avoided to minimize borohydride hydrolysis (loss of H_2 from solution accelerates hydrolysis). Solutions of dimethylamine borane were prepared in the same manner.

3.3 Results & Discussion

3.3.1 Oxidation of BH_4^- at Au

The oxidation of BH_4^- at Au electrodes has been studied extensively at both stationary[20,22,24,33,34] and rotating electrodes[35-38], as well as in fuel cells[29,39]. Even BH_4^-'s first hydrolysis or oxidation product, BH_3OH^-, has been studied (in the form of dimethylamine borane, or DMAB, as discussed below) at Au with stationary[26,27,40], rotating[26], and fuel cell electrodes[41]. While the literature is in near unanimity that BH_4^- can be oxidized at stationary Au electrodes to produce >7e^-/mol[20,24,29,39,42] (though Liu et al. report 4.5e^- [22]), studies using a Levich analysis (performed at a RDE) are in disagreement as to whether the oxidation is 7e^- [35] or variable, depending on the applied potential[36,38]. Even these studies can be misleading, as the linearity of the Levich plots can be in question. For example, some studies were based on very limited data sets[35,38], while others have employed an extremely high concentration of BH_4^- (>2M) that did not yield linear plots[36], likely due to the enhancement of bulk hydrolysis[35] and kinetic limitations[26,40] at high concentrations of BH_4^-. The range of rotation rates has also been limited. There is an evident lack of consensus with regards to Levich behavior of BH_4^- at Au.

In addition to disagreements over electron count, opinions also differ as to whether Au is "catalytic" for the hydrolysis of BH_4^- to H_2 and BH_3OH^- [3.1.b]. Earlier work indicated that Au would not enhance hydrolysis[20,24] while later papers observed vigorous formation of H_2 bubbles during BH_4^- [21,38] and ammonia borane (NH_3BH_3)[41] oxidation, leading to the conclusion that Au was indeed catalytic for the hydrolysis of hydrogenated boron species.

We have performed a very detailed RDE analysis of both BH_4^- and its first hydrolysis and oxidation product, BH_3OH^- (using the precursor DMAB), at Au to get a better assessment of electron count and extent of BH_4^- hydrolysis.

A representative CV of BH_4^- at Au is shown in Figure 3.3.1.1. In a polarographic study, values of –0.6 and –0.1V were reported for the peak oxidation potentials of BH_3OH^- and BH_4^-, respectively[25] (from this point on, all potentials, including those from the literature, are reported vs. Ag/AgCl). In one of the earliest studies of BH_4^- at Au, Okinaka used Gardiner and Collat's data to speculate that his observed onset of current at –0.8V was due to BH_3OH^- and that peaks observed at –0.1 and +0.3V were from BH_4^- [33]. In a more recent study of BH_4^- at Au, Mirkin et al. found a peak at –0.46V and attributed it to BH_4^- oxidation[20]. Based on this finding, Gyenge concluded that a peak observed at –0.42 was also due to BH_4^-, with oxidative intermediates producing current at higher potentials[24]. Using a Au rotating ring-disk electrode (RRDE) assembly, Krishnan et al. determined that BH_3OH^- oxidation begins at –1.0V, with BH_4^- oxidation beginning around –0.55V, and that BH_3OH^- is generated from BH_4^- as soon as BH_4^- oxidation begins[21]. Mirkin et al.'s and Gyenge's peaks correspond to the peak at –0.52V in Figure 3.3.1.1. Gyenge ascribed the cathodic peak at +0.3V (+0.1V in his study) also to BH_3OH^- oxidation.

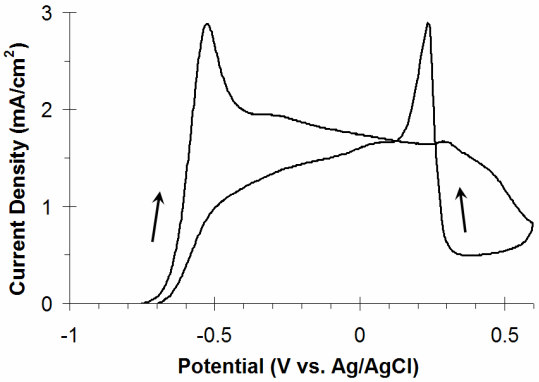

Figure 3.3.1.1: Stationary CV, 2nd scan, of 5mM $NaBH_4$ in 1M NaOH at a Au disk electrode, 25mV/s.

Additionally, there are as yet undescribed anodic peaks: a broad peak at –0.30V and sharp peaks at +0.30 and +0.46V. There are also 3 smaller peaks in the cathodic sweep. As described in detail below, we propose that some of these peaks may be analogous to those already described in the oxidation of DMAB, with the last two peaks corresponding to $BH_2(OH)_2^-$ and $BH(OH)_3^-$ [26].

3.3.2 RDE Analysis of BH_4^- at Au

RDE voltammograms of BH_4^- at Au are shown in Figures 3.3.2.1.a and 3.3.2.1.b (anodic and cathodic sweeps, respectively). The onset for BH_4^- oxidation is at about –0.640V, and two regions of mass-transport limited current are evident, from –0.450 to –0.350V and –0.200 to +0.280V. By Levich analysis, the high-potential wave yields $7e^-$ per molecule, whereas the low-potential wave shows $4.5e^-$, with the latter similar to Liu et al.'s stationary, carbon-supported Au results[22], and the presence of two waves the same as seen in recent literature[38]. The cathodic sweep also exhibited two waves with identical electron count values. These results are a bit surprising as they suggest that BH_4^- can take at least two different oxidation pathways at Au, and that the complete oxidation of BH_4^- occurs at potentials much more positive than the peak ascribed to direct and complete BH_4^- oxidation in previous findings[20,24]. Our results support previous literature findings in that the electron count obtained from BH_4^- oxidation is potential dependent [36], and are especially consistent with the qualitative conclusions of the recent work of Chatenet et al. in which they report a roughly 50% electron recovery at potentials lower than –0.2V[38].

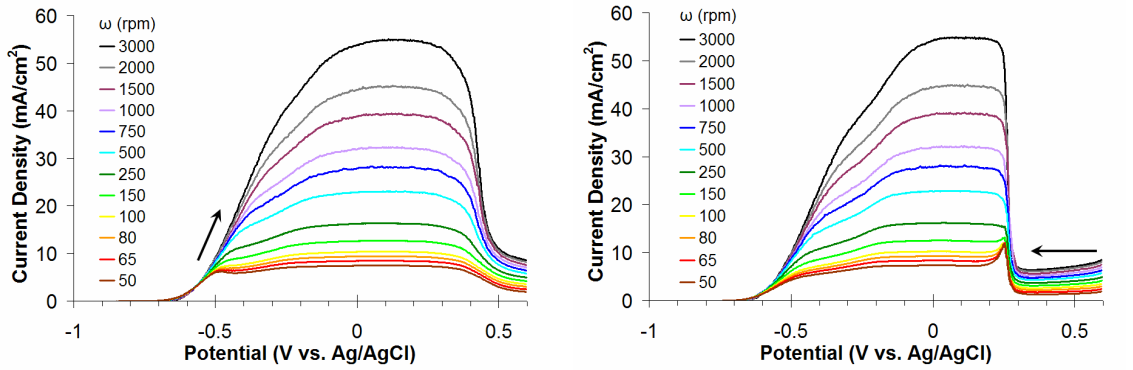

Figures 3.3.2.1.a & 3.3.2.1.b: RDE anodic (3.3.2.1.a) and cathodic (3.3.2.1.b) sweeps of 5mM $NaBH_4$ in 1M NaOH at a Au disk electrode, 25mV/s, rotated between 50-3000 rpm.

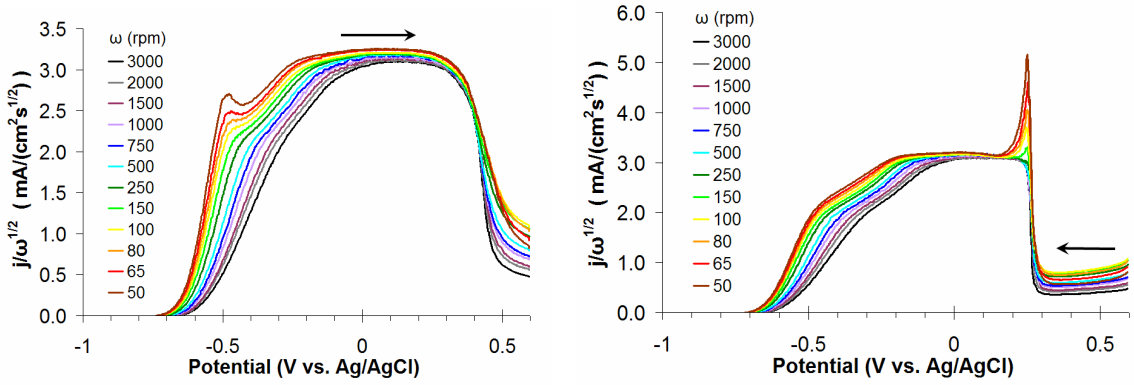

Figures 3.3.2.2.a & 3.3.2.2.b: RDE anodic (3.3.2.2.a) and cathodic (3.3.2.2.b) sweeps with current density normalized by the root of the rotation rate ($\omega^{1/2}$). Experimental conditions: 5mM $NaBH_4$ in 1M NaOH at a Au disk electrode, 25mV/s, rotated between 50-3000 rpm.

N-values for the low- and high-potential regions, as well as k_b at a suitable potential, are presented in Table 3.3.2.1. Estimates of α and k^0 are included, using the oxidation onset potential (–0.64V) as E^0.

	Au					
compound	potential (V vs. Ag/AgCl)	n (Levich)	n (Koutecký-Levich)	k_b (cm/s)	k^0 (cm/s)	$(1 - \alpha)$
BH_4^-	–0.430	-	6.9	1.2E-02	6.8E-02	0.22
	–0.400	4.5	6.5			
	+0.120	7.2	7.6			
DMAB (BH_3OH^-)	–0.670	-	2.1	4.4E-02	1.3	0.43
	–0.600	1.8	2.2			
	0.100	3.6	4			

Table 3.2.1: RDE results for BH_4^- and BH_3OH^- oxidation at Au

Our value of k_b, 0.012 cm/s, remained consistent at several potentials (–0.430, –0.410, and –0.400V). This value is an order of magnitude smaller than Gyenge's 0.14 cm/s[24]. However, Gyenge used chronocoulometry to arrive at this value, which requires corrections for charge from adsorbed species and double-layer charging. Because of these complications and limitations, chronocoulometry is not widely employed for quantitative assessment of kinetics[23]. Cheng and Scott presented a multitude of k_b values at different potentials, from 0.016 to 6.1 cm/s, with their RDE voltammograms exhibiting kinetic limitations at all potentials[36]. These numbers are difficult to compare to ours, as we only observed kinetic limitations around –0.45, which is 400 mV more negative than the potentials used in Cheng and Scott's analysis. We were unable to determine a consistent value of k^0, which was dependent on potential (0.068 to 0.13 cm/s from –0.430 to –0.400 V). This inconsistency likely reflects both the difficulty of choosing an appropriate E^0 as well as the nonlinearity of the ln $[i / (i_{l,a} - i)]$ vs. E plots used to determine α. These values are somewhat similar to Mirkin et al.'s estimate of 0.27 cm/s, which seems

coincidental considering that their value was obtained from quantitative modeling and used an E^0 that was 100mV more positive[20]. The estimated k^0 values are also close to those found in the Tafel plot of Chatenet et al. [38] (~10^{-2} cm/s) when using E^0 = –0.8V and assuming an irreversible reaction.

It is notable that Chatenet et al. [35], Krishnan et al.[21], and Cheng and Scott[36] observed just one oxidation wave in their studies of BH_4^- at a Au RDE. Our early attempts at generating RDE voltammograms at a 1mm diameter Au electrode produced similar results, where voltammetric profiles for 5mM BH_4^- at rotation rates around 1000 rpm, and higher, did not show separation between the two waves with the low-potential oxidation wave largely absent, as shown in Figure 3.3.2.3. We attribute this to the excessive H_2 bubble formation at the electrode, which blocks much of the surface and may add small, insulating layers of H_2 gas that hinder the kinetics of the already slow, low-potential wave. The H_2 bubbles are small and hydrophobic, and tend to adhere to the Teflon® perimeter of disk electrodes. Thus, a small diameter electrode can easily become occluded, while the 5mm diameter electrode used in this study allowed bubbles to collect at the perimeter of the Au disk and left most of the electrode exposed, generating more reproducible, better defined, and detailed voltammograms (Figures 3.3.2.1.a and 3.3.2.1.b). Colominas et al. also noticed a profound effect in switching to a 6mm Au electrode from a 1mm electrode in their CV studies of BH_4^- [43]. Both Chatenet et al.[34] and Krishnan et al.[21] used ~2mm diameter electrodes and present data at 900 rpm or higher.

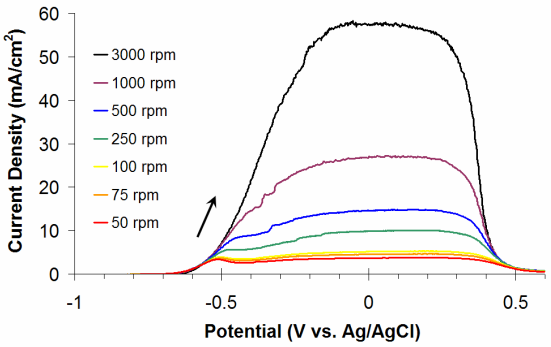

Figure 3.3.2.3: RDE anodic sweep of 5mM $NaBH_4$ in 1M NaOH at a 1mm Au disk electrode, 25mV/s, rotated between 50-3000 rpm.

Our experiments at higher concentrations of BH_4^-, such as 50mM, showed extreme kinetic limitations in approaching the mass-transport limited current, with currents at 500 rpm not showing steady-state behavior until +0.3V, and currents at 1500 rpm not showing steady-state behavior at all within the potential window of study (from –1.0 to +0.6V; see Figure 3.3.2.4). Only for rotation rates of 150 rpm and below could we generate a mass-transport limited plateau in the voltammogram by +0.1V. Cheng and Scott used 270mM BH_4^- and produced similar RDE voltammograms, also with a 5mm diameter electrode. Much of the apparent kinetic limitations in these experiments may also stem from H_2 bubbles blocking the electrode surface, which inhibits diffusive reactant transport, and the presence of bubbles may be responsible, at least in part, for the noise in this study's voltammograms. The formation of H_2 bubbles at high BH_4^- concentrations (≥50mM) is profuse enough to cover even a 5mm electrode, and this is expected, as the hydrolysis of BH_4^- to H_2 is first order with respect to BH_4^- concentration[19,35,44].

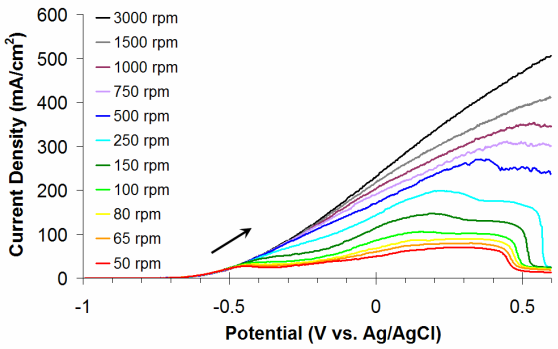

Figure 3.3.2.4: RDE anodic sweep of 50mM $NaBH_4$ in 1M NaOH at a 5mm Au disk electrode, 25mV/s, rotated between 50-3000 rpm.

These studies at higher concentrations also do not exhibit the two separate oxidation waves, and the disappearance of the first wave at higher concentrations has been observed for BH_4^- [38], DMAB[27], and NH_3BH_3[28].

Some of our early trials duplicated the unphysical $9.7e^-$ per molecule reported previously at more positive potentials in Levich analyses[36]. The small geometric electrode area (1mm dia.) and high BH_4^- concentrations (15-50 mM) led to extensive surface coverage by bubbles, which were rapidly produced upon the onset of oxidative current, but could be swept away at high rotation rates. The Levich plots for our preliminary experiments often appeared linear, but the error in these experiments became very evident in the rotation rate-normalized current plots (Figure 3.3.2.5), which showed lower-than-expected currents at slow and moderate rotation rates for the high-potential oxidation. This effect is likely due to surface coverage by bubbles at slow rotation rates, which decreases the electroactive area of the electrode and thus the observed limiting current value as well. Decreased limiting current values at low rotation rates in a Levich plot will cause an artificial increase in the overall slope, which may explain the aforementioned unphysical values of n.

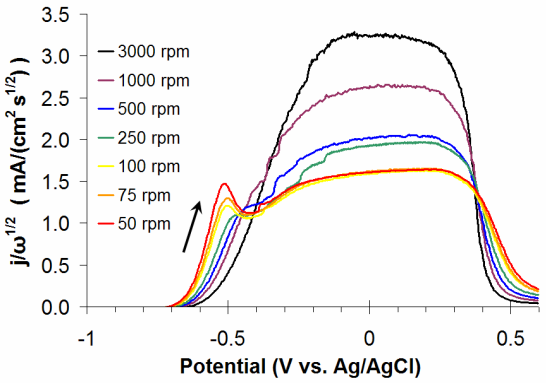

Figure 3.3.2.5: RDE anodic sweep with current density normalized by the root of the rotation rate ($\omega^{1/2}$). Experimental conditions: 5mM $NaBH_4$ in 1M NaOH at a 1mm Au disk electrode, 25mV/s, rotated between 50-3000 rpm.

The results of Chatenet et al.[37] are somewhat perplexing in that they also exhibit two waves in the anodic sweep but have limiting current density values very disparate to those presented here. While their values of n (4, 8) observed in the two waves are essentially identical to ours (4.5, 7.2), their values were calculated using their determined BH_4^- diffusion coefficient of 3.2×10^{-5} cm^2/s [45], which is about double the literature value determined by Denuault et al.[31], and therefore the similarity in n must be regarded as coincidental. The diffusion coefficients determined in the subsequent study had moderate error, and the value most applicable to our system ($2.59 \pm 0.68 \times 10^{-5}$ cm^2/s for 1M NaOH, 1mM BH_4^- [45]) has a large uncertainty (26%) that nearly encompasses the existing literature value (1.67×10^{-5} cm^2/s[31]). The new values were also determined using the transit-time technique[23,46,47] on an Au-electroplated Pt RRDE that showed significant character for Pt surface oxides and hydroxides, likely from etching of deposited Au. If the ring and disk had different compositions of Pt and Au, the value of n would not be uniform at the two electrodes, which may have interfered with the assessment of interruption in the ring's

steady-state current vital to a transit-time measurement. Thus, we have chosen to use the existing literature value of the diffusion coefficient.

The consequence of Chatenet et al.[38] using a different diffusion coefficient for the same n-value is that their limiting current values are 50% higher than those found in this study. While knowledge of n and diffusion coefficient may change over time, limiting current densities should not. We note that our 5mm Au RDE used for BH_4^- analysis was also used to study BH_3OH^-, and our n-values for the latter experiment were in agreement with microelectrode studies when using the same diffusion coefficient[27,28], as discussed below. Additionally, approximately the same limiting current densities for BH_4^- oxidation were observed at both our Au and Pt electrodes in identical electrolyte (see Tables 3.3.2.1 and 3.3.6.1 and details for Pt below). Moreover, we had very little variance in rotation-rate-normalized, limiting current densities (Figures 3.3.2.2.a and 3.3.2.2.b). Since both concentration and rotation rate vary among experiments, we compared our rotation-rate- *and* concentration-normalized, limiting current densities, with several studies from Chatenet's group. For our $7.2e^-$ oxidation of BH_4^- at Au, our average values are 0.64 and $0.65 mA/(cm^2 s^{1/2} mM)$ for 5mM and 50mM BH_4^-, respectively. Across works, Chatenet's values are 0.65[35] and 1.07[38] for RDE studies, and 0.67 to 1.55 for an RDE and 0.48 to 0.98 for an RRDE within the same study[45]. Given this variance in limiting current density, we cannot make a meaningful comparison with the results presented here.

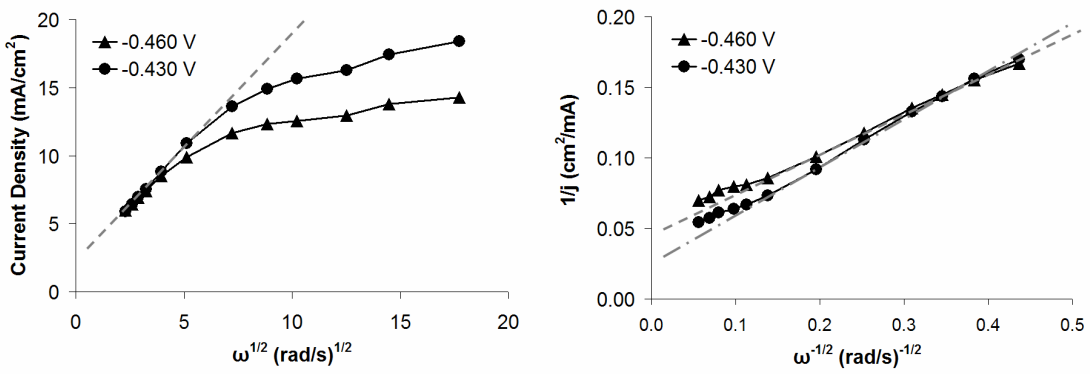

Figures 3.3.2.6.a & 3.3.2.6.b: Levich (3.3.2.6.a) and Koutecký-Levich (3.3.2.6.b) plots reflecting a CE process for the anodic sweep of 5mM $NaBH_4$ in 1M NaOH at a Au disk electrode sampled at the potentials indicated (in V vs. Ag/AgCl).

The RDE voltammograms (Figure 3.3.2.1.a) show a peculiar peak in the anodic sweep at –0.460V that gradually disappears at higher rotation rates. The rotation rate-normalized current plot (Figure 3.3.2.2.a) suggests that it represents a CE process, showing that the rotation rate-normalized current decreases below its steady-state value at higher rotation rates, as would be expected for a CE reaction rather than a simple kinetic limitation. This result is supported by both the Levich (Figure 3.3.2.6.a) and Koutecký-Levich (K-L) plots (Figure 3.3.2.6.b) at this potential, with both showing deviations from linearity at higher rotation rates reflecting a lower than expected current. The peak is likely H_2, considering its low potential, its similarity to the established H_2 peak for BH_4^- at Pt (see below), and that it appears at the same potential that H_2 bubbles form at Au during BH_4^- oxidation (the bubbles are more evident with 50mM than with 5mM BH_4^-). While it is generally stated that Au has no activity for H_2 oxidation[21], an H_2 peak can be observed by sweeping a Au electrode to low potentials in acid, generating H_2 bubbles at the electrode surface, and then sweeping back to positive potentials (Figures 3.3.2.7 and 3.3.2.8). This approach is more suitable for comparison than simply using an H_2-saturated solution[21],

since BH_4^- hydrolysis does produce copious H_2 bubbles at the electrode surface. The H_2 peak we observe at Au in 0.1M H_2SO_4 can be enhanced by sweeping to lower potentials (Figure 3.3.2.7) or by holding the electrode at low potentials for longer periods of time (Figure 3.3.2.8). In addition to BH_4^- having an H_2 peak at Au, Zhang et al. proposed that a similar peak in the CV of DMAB at Au is also related to H_2 [41]. Although these peaks are likely H_2, we were unable to generate a strong H_2 peak at Au in 1M NaOH. Rather, we saw a significant increase in background current encompassing several small peaks while oxidizing H_2 generated at Au, similar to, but much more pronounced than, the data presented by Krishnan et al.[21] (Figures 3.3.2.9 and 3.3.2.10). It is likely that base inhibits the oxidation of H_2, but the presence of BH_4^- promotes it enough to overcome the inhibition. The peak position and increase in background current were consistent with stationary CV's of BH_4^- at Au and Pt, both of which exhibit a large anodic peak and background current on the first anodic sweep only (Figures 3.3.2.11.a and 3.3.2.11.b for Au and Pt, respectively).

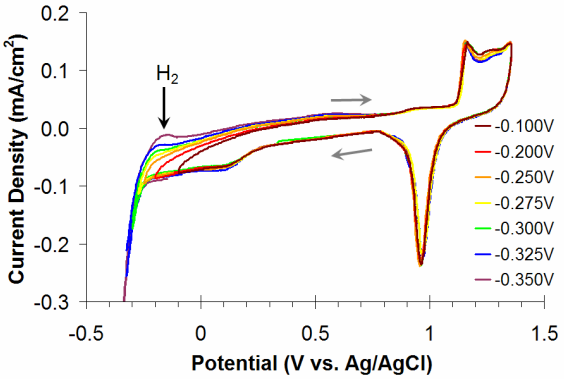

Figure 3.3.2.7: Window-Opening CV's of a 5mm Au disk electrode in 0.1 M H_2SO_4, 25mV/s, showing a putative H_2 peak.

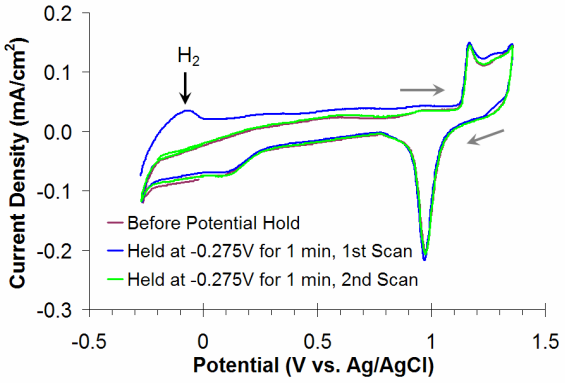

Figure 3.3.2.8: CV's of a 5mm Au disk electrode in 0.1 M H_2SO_4, 25mV/s, showing background current from H_2 oxidation. Two of the scans were paused at low potential to generate H_2 at the surface of the Au, causing an increase in oxidative current.

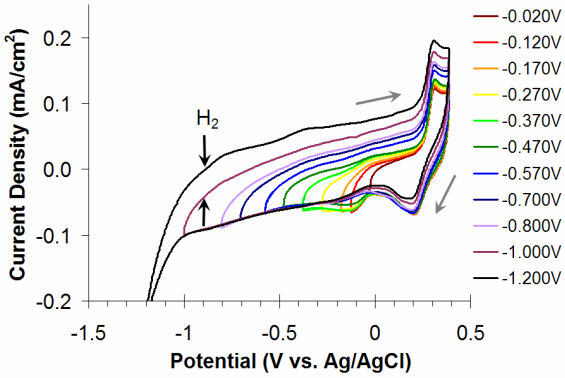

Figure 3.3.2.9: Window-Opening CV's of a 5mm Au disk electrode in 1M NaOH, 25mV/s, showing background current from H_2 oxidation. The legend indicates the negative limit of the scans; the positive limit of each scan was +0.4V.

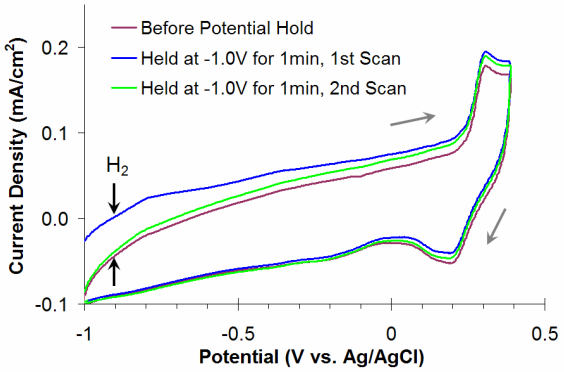

Figure 3.3.2.10: CV's of a 5mm Au disk electrode in 1M NaOH, 25mV/s, showing background current from H_2 oxidation. Two of the scans were paused at low potential to generate H_2 at the surface of the Au, causing an increase in oxidative current.

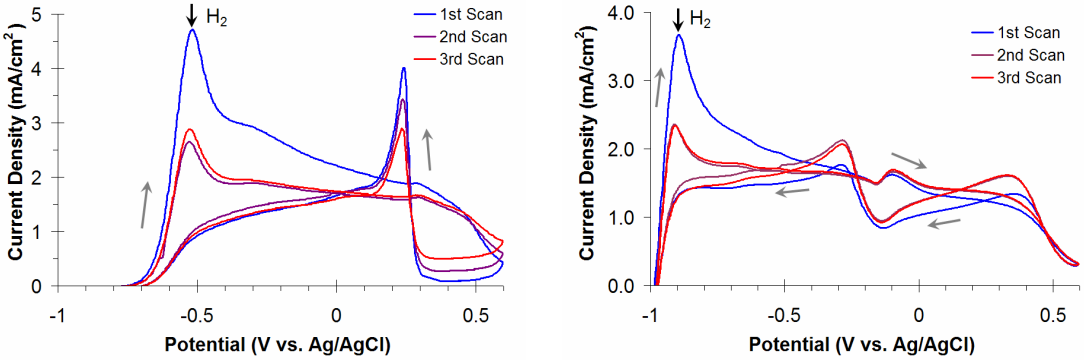

Figures 3.3.2.11.a & 3.3.2.11.b: CV's of 5mM $NaBH_4$ in 1M NaOH at 5mm Au (3.3.2.11.a) and 3mm Pt (3.3.2.11.b) disk electrodes, 25mV/s, showing a highly similar increase in suspected H_2 peaks and background currents for the first anodic sweep only.

Looking at the rotation rate-normalized current plot of the cathodic sweep (Figure 3.3.2.2.b), yet another CE process seems evident at +0.250V, but it manifests as an EC_{cat} process (increased current from linearly expected values at lower rotation rates) in the Levich and K-L plots (Figures 3.3.2.12.a and 3.3.2.12.b, respectively). An alternative explanation is plausible: It

has been previously determined that Au's surface oxide, even if only partially formed, is completely inactive towards BH_4^- [38] and BH_3OH^- oxidation[40,48] (at pH 14, Au oxide formation begins at +0.23V and oxide reduction at +0.30V). After the surface oxide is partially removed by reduction around +0.250V, the exposed Au surface can begin oxidizing the BH_4^- accumulated in the diffusion layer during the Au oxide's inactivity, resulting in a current profile akin to a potential step. This peak looks progressively smaller as the mass-transport limited current increases and outpaces the peak, creating a false EC_{cat} signature of higher-than-expected current at low rotation rates. Such a process was previously described for DMAB oxidation at Au[27].

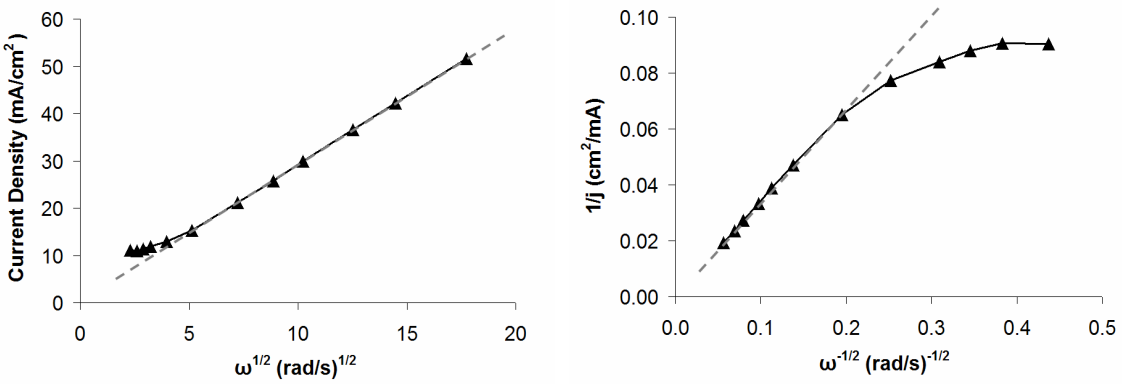

Figures 3.3.2.12.a & 3.3.2.12.b: Levich (3.3.2.12.a) and Koutecký-Levich (3.3.2.12.b) plots reflecting an EC_{cat} process for the cathodic sweep of 5mM $NaBH_4$ in 1M NaOH at a 5mm Au disk electrode sampled at +0.245V vs. Ag/AgCl.

Although several coupled-chemistry events were observed, the ECE mechanism proposed by Mirkin et al.[20] was not observed. In Molina-Concha et al.'s FTIR study of BH_4^- oxidation at Au, a slightly modified version of the ECE reaction is proposed based on observable species at the electrode surface, though it was proposed that either the chemical or second electrochemical step could not occur until the high-potential oxidation region[49].

3.3.3 Oxidation of DMAB (BH_3OH^-) at Au

While it certainly appears that BH_4^- follows two distinct oxidation pathways at Au, it is unclear if the lower-potential, lower-electron-count oxidation represents BH_3OH^- generated by chemical hydrolysis, or if it is an, as yet undetermined, oxidation of BH_4^- itself. The reported stationary CV's of BH_4^- [24] and BH_3OH^- [26,40,41] have nearly identical shapes, while the anodic sweep of our RDE voltammogram of BH_4^- (Figure 3.3.2.1.a) is also quite similar to that of BH_3OH^- in Sadik et al.'s RDE study[26] and in Nagle and Rohan's microelectrode studies[27,28]. It is therefore pertinent to study BH_3OH^- in an effort to separate out the contributions of BH_4^- and BH_3OH^- in the CV's.

The electrooxidation of DMAB at Au is thought to follow a CE process in which BH_3• first dissociates from dimethylamine, reacts with OH^- to form BH_3OH^-, and is then oxidized as BH_3OH^- [26]. Thus, studying DMAB is equivalent to studying BH_3OH^- and has been used as such[50].

In the CE process, DMAB is thought to undergo a 3 to 6e^- oxidation to $B(OH)_4^-$ depending on how many electrons are lost to H_2[26,27] in an oxidation-catalyzed process akin to that observed for BH_4^- :

$$(C)\ (CH_3)_2NBH_3 + OH^- \leftrightarrows (CH_3)_2N + BH_3OH^- \qquad \textbf{[3.3.3.a]}$$

Followed by

$$(E)\ BH_3OH^- + 6OH^- \rightarrow B(OH)_4^- + 3\ H_2O + 6e^- \qquad \textbf{[3.3.3.b]}$$

and

$$(E)\ BH_3OH^- + 3OH^- \rightarrow B(OH)_4^- + 3/2\ H_2 + 3e^- \qquad \textbf{[3.3.3.c]}$$

A stationary CV of DMAB at Au is presented in Figure 3.3.3.1, showing four peaks. Sadik identified the oxidations to be due to BH_3OH^- at –0.7V, BH_3OH^- and Au oxide formation in the broad region around –0.30V, $BH_2(OH)_2^-$ at +0.22V, and $BH(OH)_3^-$ at +0.37V. Sadik also saw peaks for these species in the cathodic sweep, arranged in the same order based on the oxidation peak potentials. This general, stepwise mechanism of BH_3OH^- oxidation to form $B(OH)_4^-$ instead of BO_2^- [19] at Pt was supported by Martins and Nunes[50]. Zhang et al.[41] also thought the broad region at –0.30V was from BH_3OH^- oxidation, but attributed the peak at –0.7V to H_2, based on the presence of H_2 bubbles at the electrode surface and its similarity in potential and shape to Gyenge's H_2 peak at Pt[24].

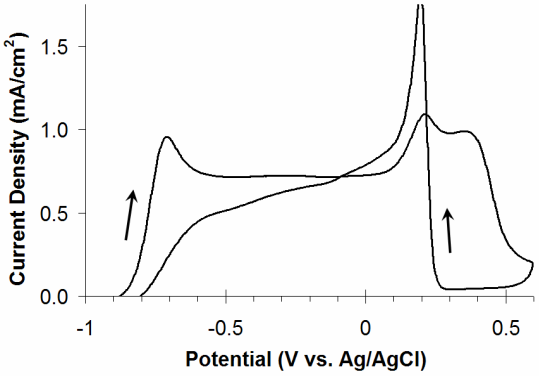

Figure 3.3.3.1: Stationary CV, 2nd scan, of 5mM DMAB in 1M NaOH at an Au disk electrode, 25mV/s.

3.3.4 RDE Analysis of DMAB (BH_3OH^-) at Au

The RDE voltammograms of DMAB at Au are shown in Figures 3.3.4.1.a and 3.3.4.1.b (anodic and cathodic sweeps, respectively). The onset potential for oxidation, –0.870V, was a full 230mV more negative than that observed for BH_4^-, in agreement with observations of

BH_3OH^- at Hg[25] and Au[19-21,27,28,33] electrodes. Again similar to BH_4^-, the RDE voltammograms have two regions of mass-transport-limited current, with a lower current, lower potential oxidation from –0.720 to –0.460V, and a higher current, high potential oxidation from –0.290 to +0.280V. Similar waves have been reported in microelectrode studies of DMAB and NH_3BH_3 at Au[27,28]. The low and high potential oxidations begin 300mV and 100mV more negative, respectively, for DMAB than for BH_4^-. Both the low and high potential oxidations seem to involve approximately one-half the number of electrons observed for BH_4^-, at 1.8 and 3.6e^- vs. 4.5 and 7.2e^- , respectively (Table 3.3.2.1). These n-values are both one e^- higher than those determined in Sadik's RDE analysis over the same potential regions[26] and reflect significant loss of electrons to H_2, as BH_3OH^- can theoretically generate up to 6e^- per molecule during oxidation to $B(OH)_4^-$ (see [3.3.3.a] and [3.3.3.b]). Using BH_3OH^-'s reported diffusion coefficient of ~8x10^{-6} cm^2/s [27,40], the values for n become 3 and 6 for the low-potential and high-potential regions, respectively, which agree with previous studies using the same values of the diffusion coefficient[27,28]. If the values for n are this high, it remains unclear how BH_3OH^- can exhibit a diffusion coefficient 50% smaller than BH_4^-'s.

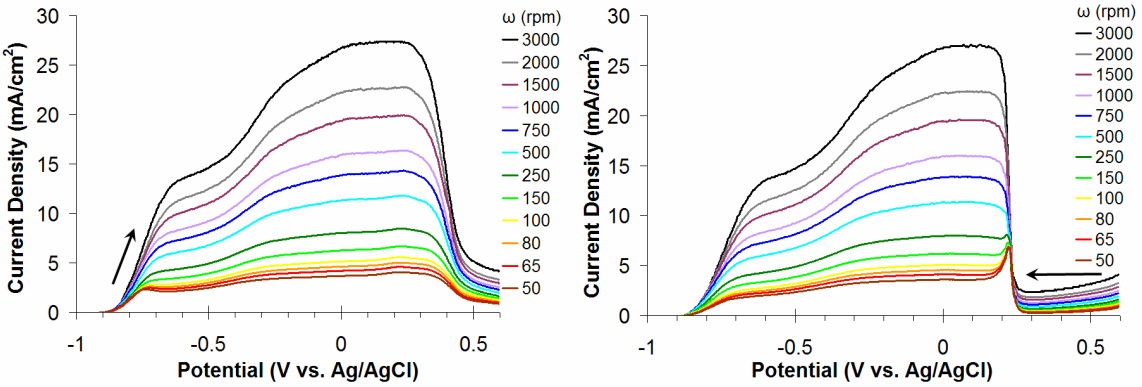

Figures 3.3.4.1.a and 3.3.4.1.b: RDE anodic (3.3.4.1.a) and cathodic (3.3.4.1.b) sweeps of 5mM DMAB in 1M NaOH at an Au disk electrode, 25mV/s, rotated between 50-3000 rpm.

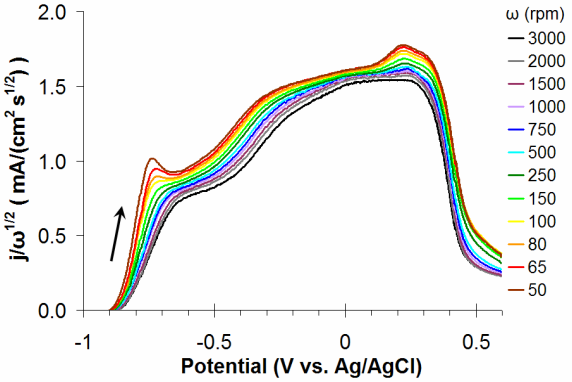

Figure 3.3.4.2: RDE anodic sweeps with current density normalized by the root of the rotation rate ($\omega^{1/2}$). Experimental conditions: 5mM DMAB in 1M NaOH at an Au disk electrode, 25mV/s, rotated between 50-3000 rpm.

Although the anodic sweeps of the RDE voltammograms are quite similar for BH_4^- and BH_3OH^-, it is perplexing that, should BH_3OH^- be an intermediate in the oxidation of BH_4^- at Au surfaces, that the two compounds should have different transition potentials between regions of low- and high-potential oxidations (–0.20V for BH_4^-,

–0.290V for BH_3OH^-). It is possible that at Au, BH_3OH^- proceeds along a different oxidation pathway than does BH_4^-, possibly involving easier-to-oxidize intermediates. Assuming this were the case, perhaps not enough BH_3OH^- is generated from BH_4^- to manifest BH_3OH^-'s mass-transport limited current, so current output during BH_4^- oxidation is dominated by BH_4^-'s separate, higher-onset-potential oxidation pathway. It is alternatively possible that BH_3OH^- inhibits BH_4^- oxidation, causing the same intermediates to be oxidized at more positive potentials. This inhibitory effect was also observed in Molina-Concha et al.'s FTIR study of BH_4^- oxidation at Au, and their results suggested that either specifically-adsorbed BH_3 or BH_3OH^- may cause the effect[49]. Although BH_4^-'s and BH_3OH^-'s oxidation pathways to $B(OH)_4^-$ may not be identical, they show significant similarities, as both produce separate low- and high-potential mass-transport limited currents, and both show peaks in the same positions for oxidation of intermediates (broad peak at –0.30V, two peaks between +0.2 and +0.4V; see Figures 3.3.1.1 and 3.3.3.1).

Neither DMAB nor BH_4^- show oxidation activity on Au's surface oxide, rapidly decreasing in current at +0.400V in the anodic sweep and exhibiting no oxidative current in the cathodic sweep until the oxide layer is partially removed via reduction by +0.250V. These results confirm previous findings of the inactivity of Au oxide towards BH_4^- oxidation[38,40,48].

The rotation rate-normalized current plot of DMAB at Au (Figure 3.3.4.2) reveals two CE processes in the anodic sweep, one at –0.720 V and a second at +0.240V. The CE reaction at –0.720 is somewhat evident in the Levich plot (Figure 3.3.4.3.a) and the K-L plot (Figure 3.3.4.3.b), while the CE reaction at +0.240V is too small to show up in either. The K-L plot is particularly difficult to assess since small nonlinearities in the Levich plot at low rotation rates

become magnified, generating a K-L signature more typical of an EC_{cat} process (enhanced normalized current at low rotation rates).

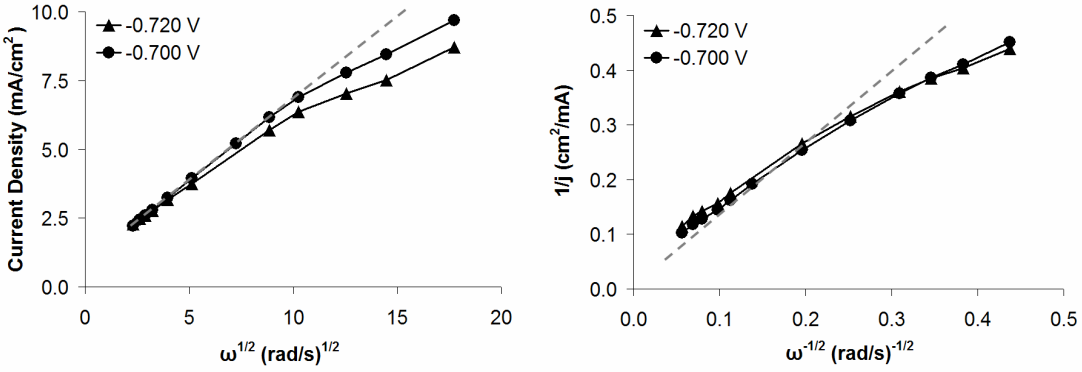

Figures 3.3.4.3.a & 3.3.4.3.b: Levich (3.3.4.3.a) and Koutecký-Levich (3.3.4.3.b) plots reflecting a CE process for the anodic sweep of 5mM DMAB in 1M NaOH at a Au disk electrode sampled at the potentials indicated (in V vs. Ag/AgCl).

The peak appearing at +0.240V is in agreement with Sadik's findings that DMAB oxidation intermediates are oxidized more completely (with higher electron count) at more positive potentials. The peak at –0.720V is very similar to BH_4^-'s peak at –0.460V at Au and the H_2 peak at Pt, so we conclude that all three peaks are likely due to H_2. The cathodic sweep has an apparent EC_{cat} peak at +0.215V, as readily discerned from the Levich and Koutecký-Levich plots (Figures 3.3.4.4.a and 3.3.4.4.b, respectively). It is not clear which process within the nest of DMAB intermediate transitions could act with an EC_{cat} mechanism. It is more likely that this process is similar to that observed for the cathodic sweep of BH_4^- oxidation, simply representing a current burst (essentially charging current) from an equivalent potential step applied to a fresh Au surface, devoid of oxide and in the presence of fuel[27].

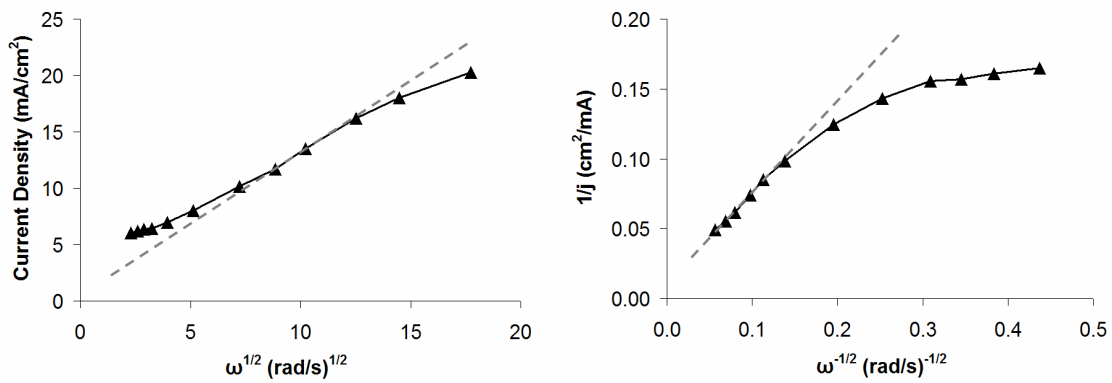

Figures 3.3.4.4.a & 3.3.4.4.b: Levich (3.3.4.4.a) and Koutecký-Levich (3.3.4.4.b) plots reflecting an EC_{cat} process for the cathodic sweep of 5mM DMAB in 1M NaOH at a 5mm Au disk electrode sampled at +0.215V vs. Ag/AgCl.

3.3.5 Oxidation of BH_4^- at Pt

The oxidation of BH_4^- at Pt has received little attention as compared to its oxidation at Au. In our view, this is largely due to the perception of Au as an ideal BH_4^- catalyst ($8e^-$/molecule at low potential, no hydrolysis), which we have discussed and disputed above. The few recent studies conducted that do use Pt do not agree on the electron count per molecule for BH_4^- oxidation[42], with estimates of $4e^-$ [24], $6e^-$ [29], 4-$6e^-$ [50,51], and even $8e^-$ [22,52,53] having been reported. Nor do the studies agree on the peak/wave assignments for the BH_4^- CV at Pt. Although Gardiner and Collat's study of BH_4^- at Hg[25] and Okinaka's study of BH_4^- at Au[33] have been used in the recent literature[24,50] to understand BH_4^- at Pt, such a comparison is difficult to make as Pt's surface catalysis is significantly different from such materials. Previously, BH_4^- at Pt was qualitatively[54] and quantitatively[55,56] investigated by RDE, but neither RDE voltammograms showing steady-state character nor Levich plots have been presented. To the best of our knowledge, this represents the first in-depth RDE study of BH_4^- at Pt, and no attempt

is made to rationalize the observations by comparison to BH_4^-'s behavior at other electrode surfaces.

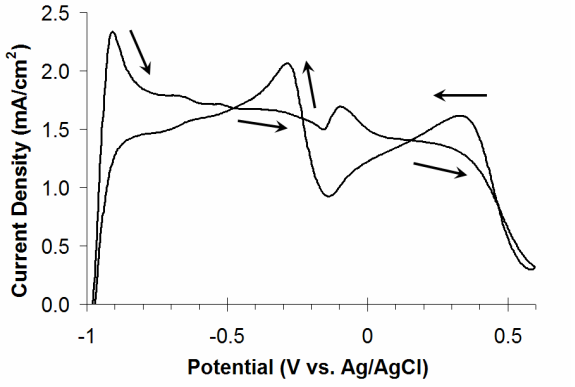

Figure 3.3.5.1: Stationary CV, 2nd scan, of 5mM $NaBH_4$ in 1M NaOH at a Pt disk electrode, 25mV/s.

A stationary CV of BH_4^- at Pt is shown in 3.3.5.1. Gyenge proposed that the first anodic peak at –0.93V is the oxidation of H_2 from BH_4^-'s CE reaction, including [3.1.b] and [3.1.c]; the anodic current from –0.45 to –0.20V is from oxidation of BH_3OH^- formed in [3.1.d]; the anodic peak at –0.10V is BH_4^- oxidation; and the cathodic peak at –0.30V is also BH_3OH^- oxidation[24]. The large cathodic peak at +0.3V was not described. The subtle anodic and cathodic peaks at –0.67 and –0.54V, which correspond to hydrogen adsorption/desorption (surface hydrides) on polycrystalline Pt in 1M NaOH (3.3.5.2), were not observed, as they were likely obscured by a larger H_2 peak. Martins and Nunes did observe these low-potential peaks, although at potentials about 100mV more negative than reported here, and also attributed them to hydrogen ionization on Pt[50]. Based on the results from Gyenge[24] and studies of BH_4^- at Au[33,41] and Hg[25], they concluded that these peaks were related to BH_3OH^- oxidation, even though the peaks were absent in their CV of DMAB (BH_3OH^-). They also ascribed the peak at –0.1V to BH_4^-. Dong et

al. disagreed with Gyenge's assessment, proposing that the low-potential current in the anodic sweep from about –0.8 to –0.2V represented BH_4^- oxidation dependent on the formation of surface hydrides, while the anodic peak at –0.1V was a hydride-independent BH_4^- oxidation on a partially-formed Pt surface oxide[29] (Pt oxide formation begins at –0.25V in 1M NaOH; see 3.3.5.2). By +0.60V, Pt forms a full surface oxide coating that is completely inactive towards BH_4^- oxidation.

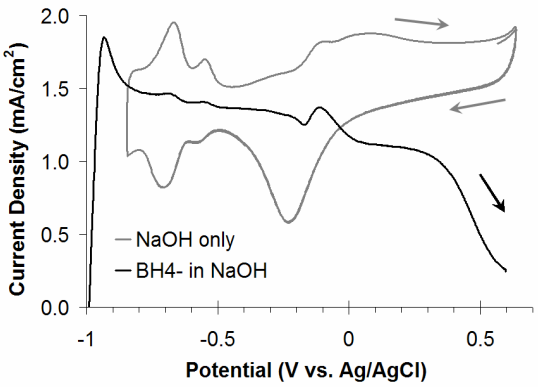

Figure 3.3.5.2: Comparison of a CV of Pt in 1M NaOH in juxtaposition with the 2nd scan of a CV of 5mM $NaBH_4$ in 1M NaOH at a Pt disk electrode, 25mV/s.

The concept of surface hydrides being essential to BH_4^- oxidation was first proposed in the 1960's by Elder and Hickling[17,18]. They noticed, as did Dong et al.[29], that the open-circuit potential of BH_4^- at Pt was lower than H_2 and changed with BH_4^- concentration, so it seemed clear that at least some of the low-potential current was from direct BH_4^- oxidation (likely through an adsorbed state) rather than solely H_2 or BH_3OH^-. Martins and Nunes found that both the low-potential peaks and the peak at –0.1V scaled with BH_4^- concentration[50,51], which we also confirmed (data not shown), providing further evidence that direct BH_4^- oxidation begins at much lower potentials than previously reported[24].

3.3.6 RDE Analysis of BH_4^- at Pt

RDE voltammograms of BH_4^- at Pt are presented in Figures 3.3.6.1.a and 3.3.6.1.b (anodic and cathodic sweeps, respectively). In the anodic sweep, oxidative current has an onset potential of –1.0V. At lower rotation rates, there are two regions which clearly exhibit mass-transport-limited current in the anodic sweep: from –0.8 to –0.25 V and from 0 to +0.2V. Thus, there are at least two oxidation processes for BH_4^- at Pt. That is, because there are two mass-transport limited processes, they must both reflect direct oxidation of BH_4^- from bulk solution, rather than an intermediate produced at the electrode surface. This finding is in agreement with Dong et al.'s proposal of separate BH_4^- oxidations in the regions of Pt hydrides and oxides[29], while the observation of mass-transport limited current contradicts the findings of Ivanov & Tsionskii that BH_4^- oxidative current is unrelated to BH_4^- diffusion[55].

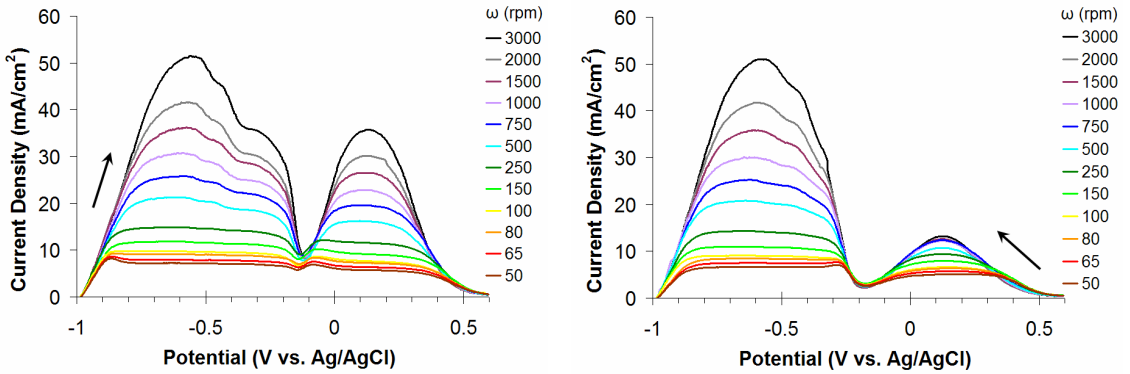

Figures 3.3.6.1.a & 3.3.6.1.b: RDE anodic (3.3.6.1.a) and cathodic (3.3.6.1.b) sweeps of 5mM $NaBH_4$ in 1M NaOH at a Pt disk electrode, 25mV/s, rotated between 50-3000 rpm.

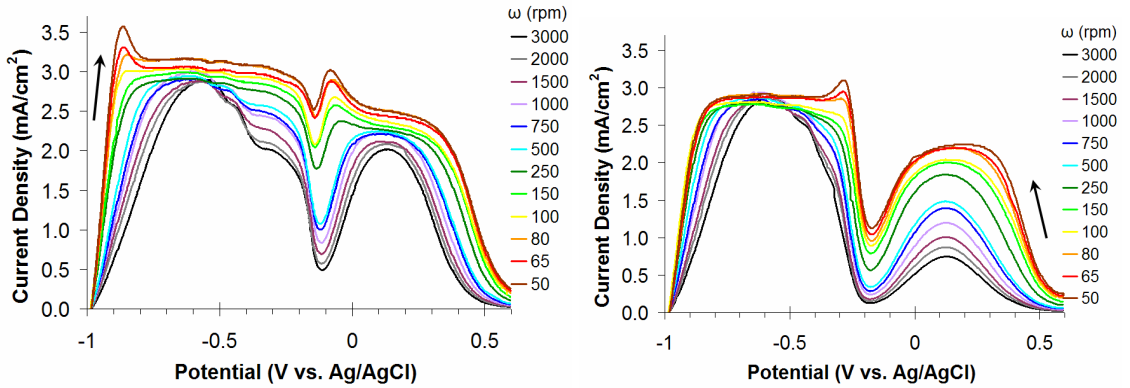

Figures 3.3.6.2.a & 3.3.6.2.b: RDE anodic (3.3.6.2.a) and cathodic (3.3.6.2.b) sweeps with current density normalized by the root of the rotation rate ($\omega^{1/2}$). Experimental conditions: 5mM $NaBH_4$ in 1M NaOH at a Pt disk electrode, 25mV/s, rotated between 50-3000 rpm.

The oxidative process in the anodic sweep between –0.8 and –0.25V also appears as mass-transport limited in the cathodic sweep, although between –0.85 and –0.3V. The oxidation in the anodic sweep between 0 and +0.2V is also evident in the cathodic sweep, but quickly reaches a maximum current and no longer responds to changes in rotation rate. Thus, while the

low-potential oxidation of BH_4^- at Pt is similar in the anodic and cathodic sweeps, the high-potential oxidation shows a pronounced hysteresis.

Levich analysis showed nearly $7e^-$ involved in the low-potential BH_4^- oxidation and at least $5e^-$ for the high-potential BH_4^- oxidation (Table 3.3.6.1). Koutecký-Levich analysis for the low-potential BH_4^- oxidation consistently showed $\geq 7e^-$ at multiple potentials. Regardless of the method, the electron count is just as high as that observed for Au and is obtained at lower overpotentials, indicating faster reaction kinetics (higher k_b) for BH_4^- oxidation at Pt than at Au (Tables 3.3.2.1 & 3.3.6.1). The high electron count also suggests that the low-potential current at Pt cannot be from BH_3OH^-, which can produce at most $6e^-$ and likely loses some redox equivalents to H_2 during hydrolysis. The high-potential $5e^-$ oxidation may reflect lower electron recovery from BH_4^- or a mix between BH_4^- and BH_3OH^- oxidations.

BH_4^- at Pt					
potential (V vs. Ag/AgCl)	n (Levich)	n (Koutecký-Levich)	k_b (cm/s)	k^0 (cm/s)	$(1 - \alpha)$
–0.800	-	7.7	2.9E-02	1.0	0.45
–0.540	6.8	7.1			
+0.090	5.4	5.9			

Table 3.3.6.1: RDE results for BH_4^- oxidation at Pt

Though Pt significantly outperforms Au in terms of kinetics, our value of k^0 at Pt, ~1.0 cm/s, is unrealistically high. We note that this value contains significant uncertainty for the same reasons as described for kinetic studies at Au: mainly, unknown E^0 and imperfect linearity of the $\ln [i / (i_{l,a} - i)]$ vs. E plots used to calculate α. We allow future work to resolve this kinetic behavior. Our value for k_b, 0.029 cm/s, is unaffected by the uncertainty in E^0 and α. This value

is lower than Gyenge's 0.14 cm/s [24], although the latter was again obtained by chronocoulometry.

RDE voltammograms at 50mM of BH_4^- at Pt exhibited vigorous bubble formation (via increased noise, supported by visual observation) beginning at around –0.1V, suggesting that the oxidation process between –0.8 and –0.25V represents a direct oxidation of BH_4^-, while the oxidation process between 0 to +0.2V represents a mixed oxidation of both BH_4^- and BH_3OH^- produced via hydrolysis. Elder also noticed that gas was freely evolved during anodic oxidation of dilute BH_4^- in base once a Pt surface oxide formed[18], and significant oxide has already formed by –0.1V on Pt in 1M NaOH (3.3.5.2). Additional support for –0.1V as the onset potential for surface hydrolysis of BH_4^- to BH_3OH^- and H_2 is shown in a plot of mass transport-normalized current ($j/\omega^{1/2}$) vs. $\omega^{1/2}$ at this potential (Figure 3.3.6.3), which clearly evidences a CE process: as the rotation rate increased, the current gradually dipped below its anticipated mass-transport limit (represented in Figure 3.3.6.3 by the plot for the mass-transport limited BH_4^- oxidation at +0.1V), reflecting that a chemical precursor was removed from the electrode surface before it could form an electroactive species. This CE process likely reflects the generation of an electroactive product from an H_2-producing hydrolysis reaction, as indicated by visual bubble formation, which occurs at this potential. Furthermore, if extensive hydrolysis occurred between –0.8 and –0.25V, it would not be possible to obtain $7e^-$ from BH_4^- over this potential region, as far more electrons per molecule would be lost to H_2. Thus, the hydrolysis of BH_4^- at Pt likely occurs at potentials much more positive than previously thought, and BH_4^- does appear to undergo a low potential, direct oxidation at Pt.

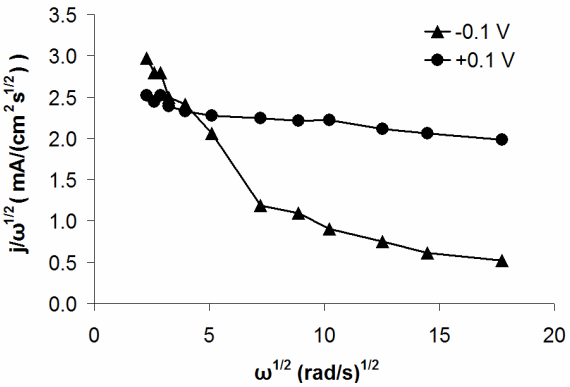

Figure 3.3.6.3: Plots of current density normalized by the root of the rotation rate ($\omega^{1/2}$) vs. the root of the rotation rate reflecting a CE process in the anodic sweep of 5mM $NaBH_4$ in 1M NaOH at a Pt disk electrode. The CE process at –0.1V is contrasted against the mass-transport limited process at +0.1V.

The Levich and Koutecký-Levich plots (Figures 3.3.6.4.a and 3.3.6.4.b) show two different CE processes in the anodic sweep, one at –0.9 and the other at –0.1V. The rotation rate-normalized current plot (Figure 3.3.6.2.a) confirms this finding, with peaks at these potentials decaying relative to the anticipated mass-transport-limited current. The peak at –0.9V is likely due to H_2, identified primarily by location and precedent[24,50], but it is unclear if this CE process reflects hydrolysis in bulk solution or low-rate hydrolysis at the Pt surface that does not exhibit visible H_2 bubble formation. The CE process at –0.1V is more difficult to discern because of the dip at –0.125 to –0.15V, which generates a shifting baseline. Based on the appearance of bubbles at this potential, the peak is probably the oxidation of a BH_4^- hydrolysis intermediate, as described above. The peak in the cathodic sweep at –0.3V (Figure 3.3.6.2.b) also appears to be a CE process, but is, once again, hard to analyze due to a shifting baseline. The cathodic sweep features a very strong CE process at +0.1V, a region which shows no evidence of coupled chemistry processes in the anodic sweep. This process may reflect the

oxidation of an adsorbed surface species that is dependent on the binding of a second molecule to neighboring metal sites (see the discussion of BH_3OH^-'s CV below).

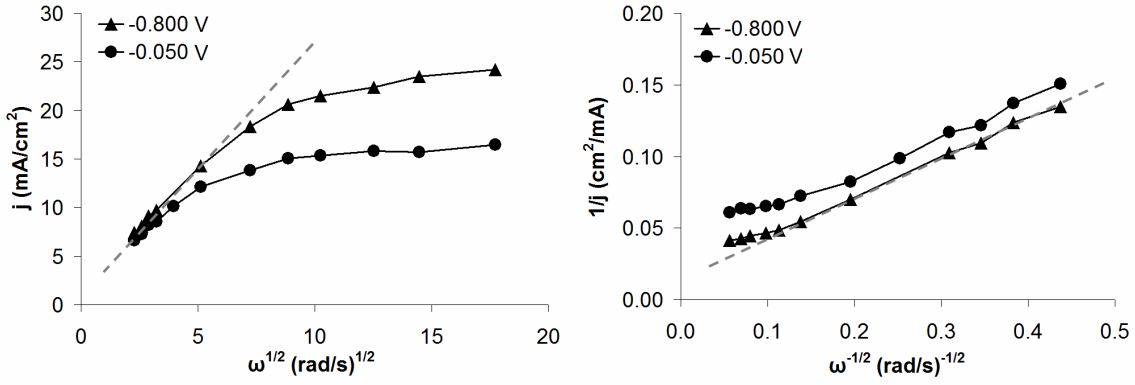

Figures 3.3.6.4.a & 3.3.6.4.b: Levich (3.3.6.4.a) and Koutecký-Levich (3.3.6.4.b) plots reflecting a CE process for the anodic sweep of 5mM $NaBH_4$ in 1M NaOH at a Pt disk electrode sampled at the potentials indicated (in V vs. Ag/AgCl).

Our work supports Gyenge's conclusion that BH_4^-'s oxidation at +0.1V represents an incomplete direct oxidation of BH_4^-, as our analysis found a very similar low electron count of 5-6e^- per BH_4^- molecule (Table 3.3.6.1) as compared to Gyenge's 4e^- [24]. It is unclear to us why Gyenge did not observe the low-potential oxidation of BH_4^-. It is possible that at stationary electrodes, the H_2 peak at –0.9V obscures the BH_4^- oxidation beginning at –0.8V. Additionally, Gyenge's use of thiourea to specifically adsorb to Pt and block surface BH_4^- hydrolysis, with the goal of examining direct BH_4^- oxidation, may have inadvertently poisoned Pt's ability to perform the low-potential, surface-hydride-dependent oxidation of BH_4^-, as thiourea concentrations as low as ~10 μM will block Pt surface hydride site occupation by 90% [57], and BH_4^- oxidation at Pt (as mentioned previously) is thought to require the formation of surface hydrides[17,18].

Additionally, Gyenge's use of a quarternary ammonium ion, which has an opposite effect on the activity of surface hydrides[58], did not interrupt BH_4^- oxidation at low potentials.

3.3.7 Oxidation of DMAB (BH_3OH^-) at Pt

As performed for Au, the oxidation of DMAB at Pt was investigated to determine which features and how much current from the BH_4^- voltammograms could be ascribed to BH_4^-'s first oxidation and hydrolysis product, BH_3OH^-. A stationary CV of DMAB at Pt is shown in Figure 3.3.7.1. This CV is similar to the one generated by Martins and Nunes at low sweep rates[50], although their scan went well past –1.0V, evolving much H_2 that likely produced its own anodic peak at –1.0V in the subsequent anodic sweep. We also observed such a peak on the first scan only. They also observed a broad anodic peak at –0.75V which we did not observe. They ascribed this peak, as well as the anodic peak at +0.14V in Figure 3.3.7.1, to BH_3OH^- oxidation. The cathodic peak at –0.3V (–0.5V in their study) was also attributed to BH_3OH^-, and the dip in the current at –0.2V was not described.

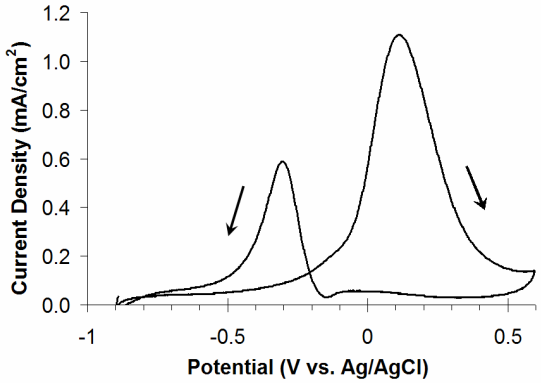

Figure 3.3.7.1: Stationary CV of 5mM DMAB in 1M NaOH at a Pt disk electrode, 25mV/s.

We attempted to perform RDE of BH_3OH^- at Pt, but the anodic peak at +0.14V did not increase with rotation rate (data not shown), so it likely represents a surface oxidative adsorption rather than a diffusional process. The current decreased to background levels at +0.6V, indicating that the full Pt oxide is inactive for BH_3OH^- oxidation, as was the case for BH_4^-. The cathodic sweep shows negligible activity in the region of the main peak from the anodic sweep, indicating that the oxidative adsorption of BH_3OH^- to Pt in the anodic sweep completely inactivates the surface of Pt for further oxidation. The anodic oxidation peak starts at about –0.2V, which is where the main adsorption peak for OH^- at Pt appears. Thus, the adsorption of BH_3OH^- to Pt may require Pt surface hydroxides. There appears to be a small reduction peak in the cathodic sweep at -0.160V, after which there is a restoration of oxidative current. This reduction may be the reduction and removal of OH^- or Pt surface oxide. Since this reduction causes restoration of oxidative current, it is likely that the OH^-, or surface oxide, was blocking metal sites neighboring the adsorbed BH_3OH^- species, which prevented further oxidation.

The cathodic sweep has a large oxidation peak around –0.4 to –0.3V, depending on scan rate, and also does not show a dependence on rotation rate, suggesting that it too is a surface process. This cathodic peak is much more negative than the main oxidative peak in the anodic sweep at +0.140V, and does not reappear in subsequent anodic sweeps, suggesting that the cathodic peak belongs to a new species formed during BH_3OH^- oxidation. The new species, perhaps $BH_2(OH)_2^{2-}$, remains adsorbed to the Pt surface until OH^-, or oxide, is stripped from the surface in the cathodic sweep, which then allows the species to be oxidized, generating an oxidative peak. The oxidation of this species may require a free neighboring metal site, which could explain why the oxidation cannot begin until the surface is free of oxide or specifically adsorbed OH^-.

The CV of BH_3OH^- at Pt (Figure 3.3.7.1) allows reinterpretation of the BH_4^- results. Unlike Gyenge[24] or Martins and Nunes[50] reports, we see no evidence for oxidative current from BH_3OH^- at low potentials (–1 to –0.2V) in the anodic sweep of BH_4^- at Pt (Figure 3.3.5.1). The decrease in BH_4^- current at –0.2V is likely due to the adsorption of OH^- or BH_3OH^- to the Pt surface (Figure 3.3.5.2). This adsorption blocks the surface for the lower-potential oxidation of BH_4^-, which probably requires the presence or formation of Pt surface hydrides[17,18,29]. At higher potentials, BH_4^- can undergo a second type of oxidation at Pt surface oxides or hydroxides. As evidenced from bubble formation and the CE peak at –0.1V in the rotation rate-normalized current plot of BH_4^- at Pt (Figure 3.3.6.2.a), BH_3OH^- is probably initially formed via hydrolysis around –0.15 to –0.1V and adsorbs to the Pt surface upon oxidation. The oxidized species of BH_3OH^- that remains bound to the surface strongly inhibits BH_4^- oxidation in the reverse sweep, causing the current for the high-potential BH_4^- oxidation to be limited by kinetics rather than mass transport from –0.2 to +0.5V (Figures 3.3.6.1.b & 3.3.6.2.b). Once the inhibitor, likely OH^-, is removed from the Pt surface at –0.15V, BH_3OH^-'s oxidation product can be oxidized and liberated from the surface at a potential more negative than the initial BH_3OH^- oxidation (Figure 3.3.7.1), and facile oxidation of BH_4^- resumes at –0.25V (Figures 3.3.6.1.b & 3.3.6.2.b).

To further demonstrate that the low-potential current in voltammograms of BH_4^- at Pt is from BH_4^- and not BH_3OH^-, a rotating ring-disk electrode experiment was performed (Figure 3.3.7.2). Our data (Figures 3.3.6.1.a and 3.3.6.1.b, Table 3.3.6.1) predict that BH_4^- oxidation will occur both in the low-potential region of –0.8 to –0.25 V and in the high-potential region of –0.1V to +0.4V. In contrast, previous literature has suggested that BH_4^- will only be oxidized in the high-potential region, while BH_3OH^- oxidation is solely responsible for the observed current at low potentials[24,50]. In our RRDE experiment of BH_4^- oxidation at Pt ring and Pt disk

electrodes, the ring was held at +0.1V, a potential sufficient to oxidize BH_4^- by either prediction. At 1000 rpm, essentially all of the current exhibited at the ring will be due to BH_4^- oxidation, since there is no BH_3OH^- present in bulk solution to provide high current via convection to the electrode surface, and BH_4^- has a lower residence time in the diffusion layer to generate BH_3OH^- via hydrolysis. Thus, any decreases in ring current indicate BH_4^- oxidation at the disk. The results are consistent with our prediction: as soon as the disk is swept anodically through low potentials, producing oxidative current, the ring current immediately dips, indicating that the disk is oxidizing BH_4^- at low potentials. If the low-potential current were from BH_3OH^-, as suggested in the literature, the ring current should remain constant, but this clearly is not observed. The ring current dips again as the disk is swept through the high-potential region, confirming that BH_4^- undergoes a second form of oxidation at high potentials at Pt. Thus, the RRDE results (Figure 3.3.7.2) support the concept that the direct oxidation of BH_4^- at Pt begins at –0.8V and has a second direct oxidation at –0.1V (Figures 3.3.6.1.a & 3.3.6.1.b), while BH_3OH^- is not responsible for the low-potential current in the oxidation of BH_4^- at Pt (Figure 3.3.7.1).

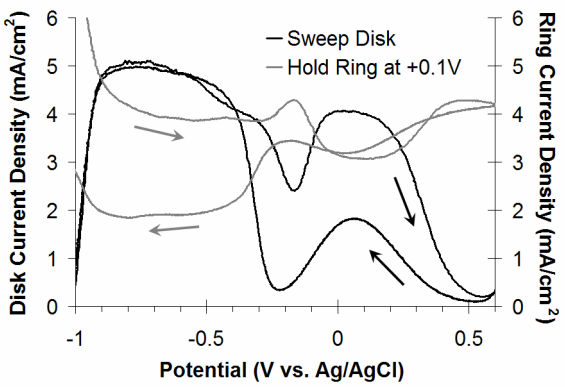

Figure 3.3.7.2: RRDE voltammograms of 1mM $NaBH_4$ in 2M NaOH at a Pt ring-disk electrode, 25mV/s and 1000 rpm. The disk was swept between –1.0 and +0.6V while the ring was held at +0.1V vs. Ag/AgCl.

3.4 Conclusions for BH_4^- Oxidation Mechanisms

3.4.1 Conclusions for BH_4^- and BH_3OH^- Oxidation at Au

The results presented here have many implications for the understanding of BH_4^- oxidation at Au, especially with regard to BH_4^-'s use in fuel cells. First, as several groups have already noticed[21,38,41], Au does, in fact, catalyze the hydrolysis of BH_4^- and BH_3OH^-, producing H_2 as a byproduct at the electrode surface. Second, and perhaps more importantly, our data show that the reported 7 to 8e^- oxidation process observed for BH_4^- at Au[20,24,29,35,36,39] only occurs 320mV more positive than the peak in a stationary CV of BH_4^- (at –0.2V vs. the peak at –0.52V), and smaller overpotentials yield only about 4.5e^- per molecule with the remainder of the electrons likely generating H_2. In similar fashion, the results suggest that the number of electrons exchanged during the oxidation of BH_3OH^- also depends on potential, with 1.8e^- available at low potential and 3.6e^- recovered at potentials above –0.3V, representing significant

losses of electrons to H_2. As described above, BH_3OH^-'s electron recovery is higher when using a smaller diffusion coefficient[27,40].

The RDE voltammograms for BH_4^- and BH_3OH^- at Au have nearly identical shapes (Figures 3.3.2.1.a and 3.3.2.1.b as compared to Figures 3.3.4.1.a and 3.3.4.1.b), suggesting that their oxidations are quite similar. Both exhibit separate low- and high-potential oxidations, with the latter generating more electrons per molecule of fuel. Since the potential separating the low- and high-potential oxidations is different for BH_4^- and BH_3OH^-, the two fuels may generate different oxidation intermediates, or BH_3OH^- may inhibit the oxidation of BH_4^- 's intermediates. Both BH_4^- and BH_3OH^- have additional intermediates that can only be oxidized at very high potentials, and these have been described previously[26]. The oxidations of BH_4^- and BH_3OH^- in the anodic sweeps show initial CE reactions, while the oxidations in the cathodic sweeps show small hysteresis and a lack of oxidative activity on Au's surface oxide.

Despite claims to the contrary[21], Au shows activity for H_2 oxidation (Figures 3.3.2.7 & 3.3.2.8), providing suggestive evidence that the first CE peak in both BH_4^- and BH_3OH^- oxidation (Figures 3.3.2.2.a and 3.3.4.2) belongs to H_2 rather than the original fuel molecules. Thus, the peaks in the stationary CV of BH_4^- (Figure 3.3.1.1) are ascribed to a combination of H_2 oxidation and the low-potential BH_4^- oxidation at –0.52V, the high-potential BH_4^- oxidation at –0.26V (broad peak), and possibly $BH_2(OH)_2^-$ and $BH(OH)_3^-$ at +0.30V and +0.46V, respectively[26]. In the cathodic sweep, the peak at +0.215V corresponds to the onset of oxidation of BH_4^- at a newly oxide-free Au surface and the broad peak at -0.25V corresponds to the high-potential oxidation of BH_4^-.

The stationary CV of BH_3OH^- on Au (Figure 3.3.3.1) has nearly the same features, with anodic peaks from H_2 and the low-potential BH_3OH^- oxidation at –0.7V, the high-potential

BH_3OH^- oxidation at –0.30V, $BH_2(OH)_2^-$ at +0.22V, and $BH(OH)_3^-$ at +0.37V, with oxidative current from BH_3OH^- throughout the anodic sweep. The cathodic peak at +0.19V is from BH_3OH^- oxidation at a newly oxide-free Au surface and the broad peak at –0.30V is from the high-potential BH_3OH^- oxidation.

Thus, many of Au's purported advantages over Pt, such as a low-potential $8e^-$ BH_4^- oxidation and absence of BH_4^- hydrolysis, are not upheld. Instead, a limitation in Au's catalytic activity is supported, in that 450mV are lost from the open-circuit potential simply to obtain the desired $7e^-$s from BH_4^- in its high-potential oxidation at Au, with lower overpotentials recovering only 4-$5e^-$ per BH_4^- molecule.

3.4.2 Conclusions for BH_4^- and BH_3OH^- Oxidation at Pt

There are two forms of direct BH_4^- oxidation at Pt. The first occurs at low potentials (–0.8 to –0.25V, Figure 3.3.6.1.a), produces $7e^-$, requires the presence of Pt surface hydrides, and is poisoned by the adsorption of BH_3OH^-. The second occurs at high potentials (–0.1 to +0.4V), involves 5-$6e^-$, and occurs on a partially-oxidized Pt surface with adsorbed OH^- and BH_3OH^-. The initial low-potential oxidation is faster than the oxidation of BH_4^- at Au. Surface hydrolysis of BH_4^- at Pt does not begin until either OH^- adsorbs to Pt or Pt surface oxides form at –0.2V, generating BH_3OH^- and copious H_2 gas. BH_3OH^- adsorbs to the surface and is oxidized, and its oxidation product can only be removed at lower potentials (–0.3V) after OH^- and Pt surface oxides are reduced (stripped) off the surface in a cathodic sweep. The oxidation and removal of the adsorbed BH_3OH^- oxidation product restores the low-potential oxidation of BH_4^-.

Peaks for the stationary CV of BH_4^- at Pt (3.3.5.1) can then be reassigned. In the anodic sweep, the peak at –0.9V is H_2 oxidation, but the peaks at –0.67 and –0.54V are Pt surface hydrides generated during BH_4^- oxidation rather than BH_3OH^-. Anodic current from –0.85 to –0.2V is from BH_4^-. The dip at –0.15 represents the diminution of the low-potential BH_4^- oxidation as OH^- binds to the surface, with its adsorption generating the peak at –0.1V. A second, high-potential BH_4^- oxidation occurs from –0.1 to +0.4V. In the cathodic sweep, the peak at +0.3V is the high-potential BH_4^- oxidation, the dip at –0.2V corresponds to the removal of OH^- or oxides from Pt's surface, and the peak at –0.3V is the oxidation of BH_3OH^-'s surface-adsorbed oxidation product. The peaks at –0.67 and –0.54V again correspond to Pt surface hydrides generated during the low-potential oxidation of BH_4^-, which produces current from –0.2 to –0.9V.

3.4.3 Implications for Direct BH_4^- Fuel Cells

While conventional thinking has favored Au as an ideal 7-8e^-, hydrolysis-free BH_4^- catalyst[20,24,29,35,39], our results indicate that Pt anodes offer a number of important advantages over Au anodes in the context of a direct BH_4^- fuel cell. First, Pt anodes are expected to increase the open-circuit voltage of a BH_4^- fuel cell by about 360mV, since direct BH_4^- oxidation begins at –1.0V rather than –0.64V for Au (Figures 3.3.6.1.a and 3.3.2.1.a, respectively). This advantage is significant considering that BH_4^- fuel cells often have an open-circuit voltage of around 1.1 to 1.4V[1,2,4,5], though higher values have been reported[6]. The gain in operating voltage should be even higher, up to 600mV, since Pt reaches its 7e^- mass-transport limited current at –0.8 to –0.7V (depending on RDE rotation rate or fuel cell flow rate) while Au does not offer this electron recovery until

–0.2V. Furthermore, since Pt was not observed to catalytically hydrolyze BH_4^- to H_2 until nearly +0.1V, hydrolysis can be minimized in a BH_4^- fuel cell with Pt anodes by operating at higher voltages, whereas Au anodes will have significant hydrolysis problems at all operating voltages.

The results also show, however, that as fuel cell voltage is decreased, Pt anodes will actually decrease, rather than increase, the current output as they progress through the dip in activity at +0.1V and from the high-current, low-potential oxidation to the low-current, high-potential oxidation (Figure 3.3.6.1.a and Table 3.3.6.1). Au anodes are expected to provide higher current at lower voltages up to the point of Au etching and dissolution (Figure 3.3.2.1.a and Table 3.3.2.1).

Some of the advantages of Pt catalysts have already been reported. It was observed that Au-Pt alloy anodes have over 3 times higher peak current densities than Au anodes, and generated approximately 25% more power when used in a BH_4^- fuel cell[37]. Yang et al. found that switching the anode material from Au to PtRu black in a BH_4^- fuel cell increased the open-circuit voltage by 150mV and achieved a maximum power increase of 36% [59].

While these increases in power may not be as high as predicted from the analytical results, they are significant nonetheless, and support the finding that Pt will outperform Au as an anode material in direct BH_4^- fuel cells. Comparisons of unalloyed, pure Pt and Au anodes are needed to fully verify this conclusion. Further understanding of the complex mechanisms of BH_4^- oxidation at noble metal catalysts will lead to enhancements in BH_4^- fuel cell performance. The techniques used in this paper offer a more reliable assessment of catalyst performance than those based on stationary or fuel cell electrodes, and will hopefully yield promising results when applied to new catalysts for BH_4^- oxidation.

3.5 BH_4^- Reversible Poisoning

3.5.1 BH_4^- Reversible Poisoning at Pt

Although Pt's low-potential BH_4^- oxidation offers a tremendous gain for BH_4^- fuel cells, it also undergoes an undesirable poisoning reaction. Figure 3.1.1 shows current generated vs. time while holding a Pt RDE electrode at various potentials and rotating (250 rpm). Current is observed to decrease from its initial value of 14 mA/cm^2 (Figure 3.3.6.1.a) by 50-90% within 10-20 min, depending on potential. Notably, current produced at –0.4 V stabilizes after a 50% loss, indicating that only a portion of the polycrystalline Pt surface can be poisoned at this potential. Current at –0.2 V first poisons, then recovers its initial value, suggesting that a self-cleaning mechanism occurs at this potential (Figure 3.5.1.2). Unfortunately, –0.2 V falls within the current dip at the upper boundary of BH_4^-'s low-potential current region I (Figure 3.3.6.1.a), providing only 5.5 of 8 e^- at 0.6 V higher (less favorable) potential.

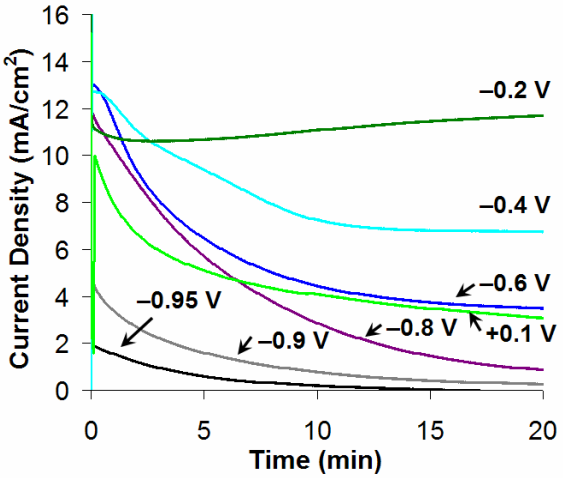

Figure 3.5.1.1: Current generated vs. time at various potentials for 5 mM BH_4^- in 1 M NaOH at Pt, 250 rpm.

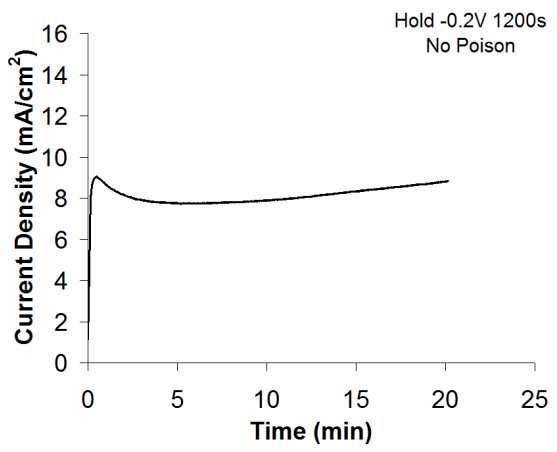

Figure 3.5.1.2: Current generated vs. time at –0.2 V for 5 mM BH_4^- in 1 M NaOH at Pt, 250 rpm.

Since very well-behaved RDE voltammograms were established for BH_4^- at Pt (Figures 3.3.6.1.a and 3.3.6.1.b), it was surprising that any poisoning occurred at all. In Section 3.3.7, the process of BH_3OH^- adsorption to Pt, which blocks BH_4^- activity in the cathodic sweep, was discussed, and it seemed that this process may actually occur at lower potentials than previously thought. The removal of BH_3OH^- required that Pt be brought to very high potentials, +0.6 V, so this appeared to be a logical potential to attempt to remove any adsorbed, poisoning species of boron on Pt. A long-term potential step was then performed to monitor BH_4^- activity at Pt over time, with occasional potential steps to +0.6 V to remove surface poisons (Figure 3.5.1.3). The results were quite encouraging: The $7e^-$ BH_4^- oxidation at Pt was well-maintained for over 20 min, while stepping positive for only 0.5 s every 300s. That is, the potential of the electrode remained at –0.7 V for 600 times the length of time it was held at +0.6 V. The preliminary demonstration of these cleaning techniques in an actual BH_4^- fuel cell is discussed in Section 8.2, and suggests that *in-situ* cleaning is instrumental to the operation of BH_4^- fuel cells at high voltage.

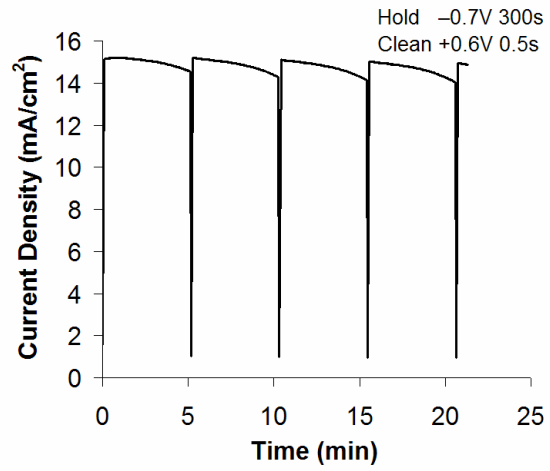

Figure 3.5.1.3: Long-term oxidative current under pulse-cleaning of 5mM BH_4^- in 1M NaOH at Pt, 250 rpm

3.5.2 BH_4^- Reversible Poisoning at Au

Au also exhibits a poisoning mechanism for its low-potential current region (see Section 3.3.2), showing a 40% loss in current over 15 min (Figure 3.5.2.1). Au's high-potential BH_4^- oxidation does not appear to poison significantly, but produces current at a potential 0.9 V higher (less favorable) than available at Pt.

We then attempted to use the same cleaning procedure at Au that we had developed at Pt. Though Pt and Au form their surface oxides at different potentials, both electrode materials have heavy oxide coverages at +0.6 V, which we speculated would likely clean both metals. Figure 3.5.2.2 shows the cleaning procedure successfully applied to an Au electrode held in Au's low potential region for BH_4^- oxidation (–0.4 V), though the electrode spent only 200 times as long at low potential as it did at +0.6 V, which is three times shorter than observed for Pt. These data were often difficult to obtain, as Au's surface quickly becomes covered by H_2 bubbles from Au-catalyzed BH_4^- hydrolysis, and the bubbles introduce fluctuations into the observed current. The

data in Figure 3.5.2.2 were obtained immediately after a fast rotation pulse used to remove the H_2 bubbles. Nonetheless, the higher-voltage, lower-current BH_4^- oxidation at Au can be maintained via *in-situ* cleaning.

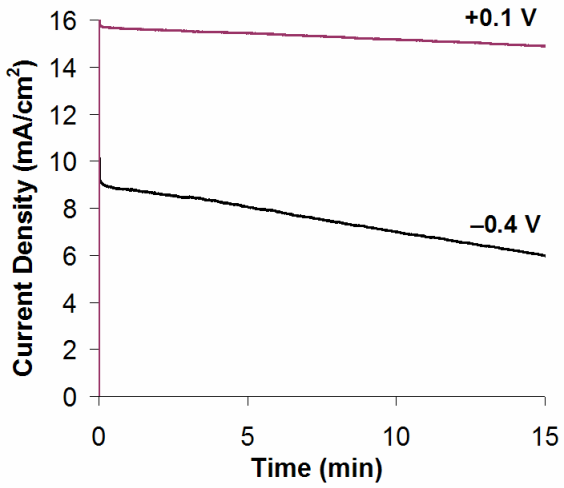

Figure 3.5.2.1: Current generated vs. time at various potentials for 5mM BH_4^- in 1M NaOH at Au, 250 rpm.

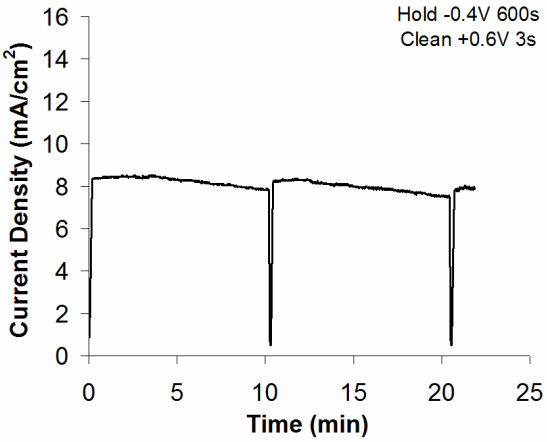

Figure 3.5.2.2: Long-term oxidative current under pulse-cleaning of 5mM BH_4^- in 1M NaOH at Au, 250 rpm

3.6 BH_4^- Oxidation at Alternative Metal Catalysts

BH_4^- exhibits significant current and fast oxidation kinetics at Pt, providing superior energy density and muliple orders of magnitude higher power density compared to H_2 or MeOH (Section 1.2). However, the cost of a Pt-based fuel cell system will always be of concern. Fortunately, BH_4^- is known to exhibit oxidation by a number of less precious metals, such as Pd, Ag, Ni, and even misch metals.[61] This feature gives BH_4^- fuel cells an important cost flexibility that is simply unachievable for H_2 or MeOH systems. A critical evaluation of BH_4^-'s oxidation process at these catalysts, however, is lacking.

Since BH_4^- does not seem to require a specific catalyst, we investigated its oxidation at a wide variety of pure metals. By conducting fundamental studies of BH_4^- oxidation at these materials, as were performed for Pt and Au, we have gained a deep, mechanistic understanding of the catalytic processes involved. This will allow not only utilization of the oxidation reactions in the most effective manner, but ideally direct the development of new, catalytic, binary or ternary alloys that maintain Pt's fast reaction rate for BH_4^- oxidation while using lower cost materials.

Though BH_4^- has oxidative activity at a wide variety of catalysts, our investigation of BH_4^- oxidation at Pt indicated that surface hydrides were critical for low-potential oxidation.[60] Thus, we have focused attention on other metals that either support surface hydrides or show low-potential oxidation of H_2. Table 3.6.1 shows the current spot values for the Pt-group metals, all of which have these characteristics, along with Ni and Ag, which have commonly been employed as BH_4^- catalysts. Au and Pt are shown at the top, as they reflect the best-performing and most frequently used BH_4^- catalysts. It quickly becomes apparent that while all of the Pt group metals are significantly more expensive than Ni and Ag, some of them are 50-90% less

costly than Pt or Au. We have therefore included Ni, Ag, and most of the Pt group metals in our research, excluding Rh, because it is actually more expensive than even Pt, and Os, for safety concerns.

Metal	**Price** ($/tr.oz.)
Au	1,353.00
Pt	1,667.00
Ni	0.70
Ag	27.30
Ru	155.00
Os	400.00
Pd	702.00
Ir	760.00
Rh	2,375.00

Table 3.6.1: Current spot values of all of the Pt-group metals, as well as several less precious metals, the latter of which have been previously used as BH_4^- catalysts.

3.6.1 BH_4^- Oxidation at Ni

A stationary cyclic voltammogram of BH_4^- at Ni is compared against a voltammogram of Ni in electrolyte alone in Figure 3.6.1.1. It is readily apparent that BH_4^- shows an oxidative reaction at Ni metal, but the current quickly dissipates upon formation of Ni oxide at –0.75 V. This find is nonetheless significant, for it shows that Ni can produce current from BH_4^- at potentials as low as those seen at Pt (Figures 3.3.6.1.a and 3.3.5.2).

The RDE voltammogram for BH_4^- oxidation at Ni is much less promising (Figure 3.6.1.2), as there is no increase in current upon rotation. This suggests that current from BH_4^- involves an irreversible, self-poisoning, surface adsorption process. Indeed, BH_4^-'s long-term oxidative current at Ni decreases by 50% within 20 min (Figure 3.6.1.3). The current produced by this process is miniscule, corresponding to < 2% of that seen at Pt. Ni's exceptionally low cost (Table 3.6.1) and low onset for BH_4^- oxidation (Figure 3.6.1.1) make it an attractive candidate as a BH_4^- catalyst, but it is unclear that its mechanism allows for the significant current densities required for high-power fuel cells.

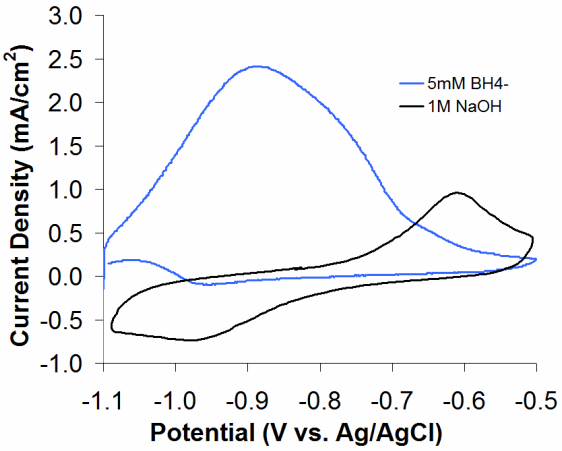

Figure 3.6.1.1: CV's of 5 mM BH_4^- in 1 M NaOH at Ni, and the Ni electrode in 1 M NaOH without any fuel present, revealing Ni surface features, 20 mV/s.

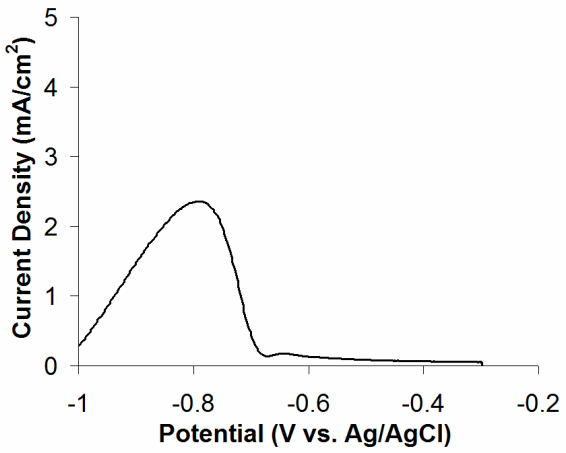

Figure 3.6.1.2: RDE voltammogram of 5 mM BH_4^- in 1 M NaOH at Ni, 3000 rpm, anodic sweep, 20 mV/s.

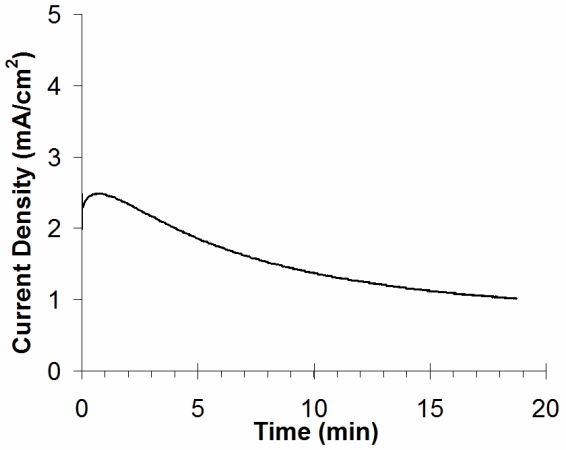

Figure 3.6.1.3: Long term oxidative current of 5 mM BH_4^- in 1 M NaOH at Ni, held at –0.9 V, rotated at 200 rpm.

3.6.2 BH_4^- Oxidation at Ag

Like Ni, Ag is a low-cost catalyst (Table 3.6.1), but it seems to have an opposite reactivity for BH_4^-, where the metal itself shows no activity for BH_4^- oxidation, but one of its surface oxides does (Figure 3.6.2.1). Although Ag forms some degree of oxide by –0.7 V, it is not until it forms a second oxide at around –0.3 V that BH_4^- oxidation begins. This reaction is

limited, because at potentials not much higher than the onset for BH_4^- oxidation (about +0.1 V), Ag oxide formation occurs vigorously, causing significant etching of the surface. This is rather unfortunate, because aside from this rather positive onset potential, Ag provides a full $8e^-$ recovery from BH_4^-, as seen in its RDE voltammograms (Figure 3.6.2.2), with a k_b of $1x10^{-2}$ cm/s at +0.04 V. Additionally, BH_4^- oxidation does not appear to poison significantly at Ag, maintaining its reaction for 30 min (Figure 3.6.2.3); most of the slight drop in current is likely attributable to bulk consumption of BH_4^- within the confines of the electrochemical cell.

Offering a poison-free, complete oxidation of BH_4^- at a fraction of the price of Pt, Ag may appear to be an attractive catalyst, but it does not show oxidation until almost 0.8 V more positive than Pt, severely compromising the voltage of a BH_4^- fuel cell. Alloys that contain Ag, and bear some of its catalytic traits, may be more attractive than Ag itself for future BH_4^- catalysts.

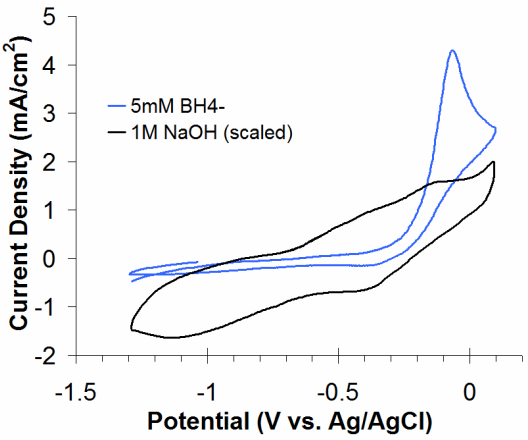

Figure 3.6.2.1: CV's of 5 mM BH_4^- in 1 M NaOH at Ag, and the Ag electrode in 1 M NaOH without any fuel present, scaled to show Ag surface features, 20 mV/s.

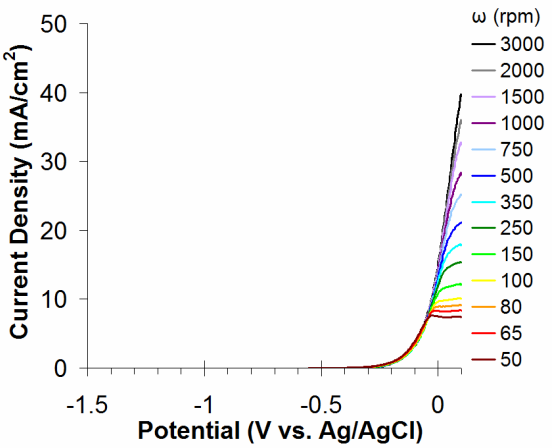

Figure 3.6.2.2: RDE voltammograms of 5 mM BH_4^- in 1 M NaOH at Ag, anodic sweeps, 20 mV/s.

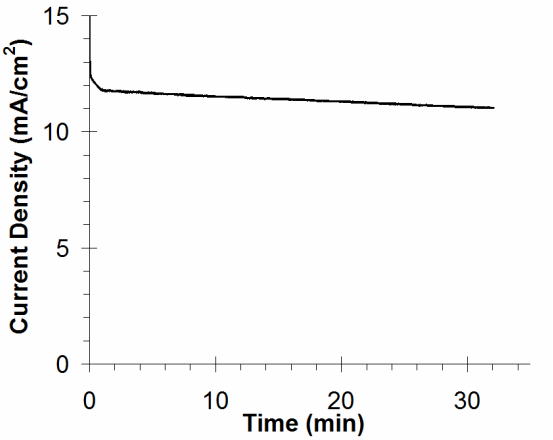

Figure 3.6.2.3: Long term oxidative current from 5 mM BH_4^- in 1 M NaOH at Ag, held at +0.17 V, rotated at 150 rpm.

3.6.3 BH_4^- Oxidation at Pd

Pd was perhaps the most promising alternative catalyst for BH_4^- oxidation that we investigated. Its reactivity with respect to surface features, however, was rather perplexing. In Pd's region of H_2 oxidation (between –0.85 and –0.75 V, Figure 3.6.3.1), BH_4^- oxidation was very slow, only just beginning its reaction. BH_4^- oxidation did not become fast enough to be

mass-transport limited at even low rotation rates until about –0.65 V, within Pd's capacitive double-layer region (Figure 3.6.3.2). The current in this region corresponds to a 3.2 e^- oxidation of BH_4^-, with a k_b of $1x10^{-2}$ cm/s at –0.63 V, which is attractive in terms of delivering significant current at lower potentials than Au, but falls far short of the available current at Pt.

Oxidative current from BH_4^- increased significantly upon formation of Pd surface oxide at –0.3 V, and the current density rose to levels that exceeded those expected from 8 e^- oxidation of BH_4^-, which corresponds to >55 mA/cm^2 at 3000 rpm (Figure 3.3.2.1.a). Some of this additional current may be due to stripping of adsorbed boron species that formed at low potential, which would be consistent with the sharp peak in the voltammogram at –0.05 V. This process cannot account for the entirety of the discrepancy; assuming full monolayer coverage of BH_4^- at the $1.31x10^{15}$ Pt atoms/cm^2, and 8e^- recovery from BH_4^-, oxidation of adsorbed species can account for only $1.7x10^{-3}$ C/cm^2 of charge, while the integrated charge from the voltammogram (with a sweep rate of 20 mV/s) corresponds to 0.13 C/cm^2. Either a fraction or entirety of the discrepancy is thus undoubtedly due to oxidation of absorbed H_2 that may have formed during BH_4^- surface or bulk hydrolysis, as Pd is well known to absorb H_2. Further study is required to understand how much of the current between –0.3 and +0.3 V is due to absorbed H_2 or increased e^- recovery from BH_4^-.

BH_4^- oxidative current at Pd declines in the low-potential, ~3 e^- recovery region with time (Figure 3.6.3.3), albeit slower than that seen at Pt (Figure 3.5.1.1). Since Pd does not appear to poison between RDE voltammetric sweeps (Figure 3.6.3.2), it is likely that Pd can be cleaned by the same sort of pulse-cleaning method that has been applied to Pt and Au (Section 3.5). Further study is needed to understand BH_4^-'s oxidation mechanism at Pd oxide, BH_4^- oxidation stability at a greater variety of potentials at Pd, and the practicality of pulse cleaning

for Pd anodes in a BH_4^- fuel cell. Pd remains very attractive as an alternative catalyst, as it is still capable of delivering significant current from BH_4^- at low potential, and costs about 50% lower than either Pt or Au (Table 3.6.1).

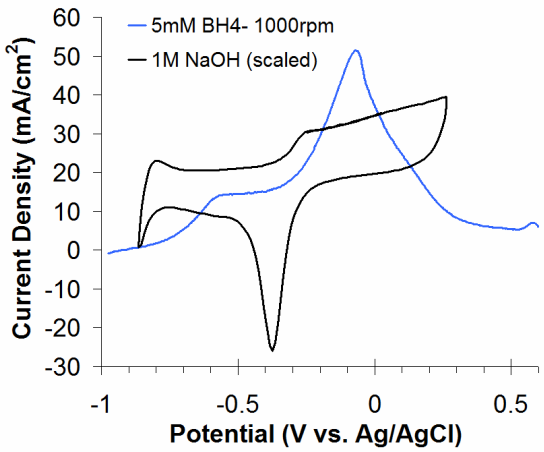

Figure 3.6.3.1: RDE voltammogram of 5 mM BH_4^- in 1 M NaOH at Pd, and the CV of the Pd electrode in 1 M NaOH without any fuel present, scaled and translated to show Pd surface features, 20 mV/s.

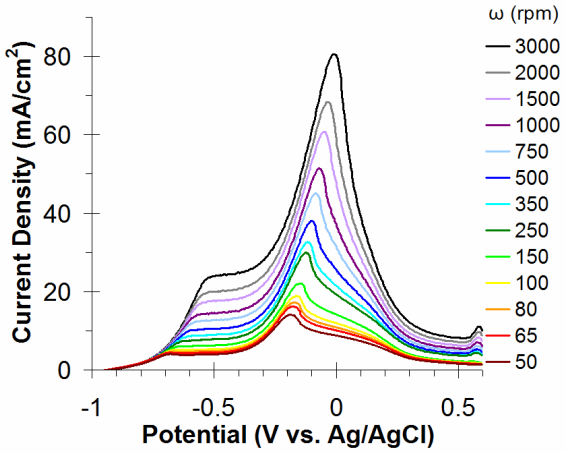

Figure 3.6.3.2: RDE voltammograms of 5 mM BH_4^- in 1 M NaOH at Pd, anodic sweeps, 20 mV/s.

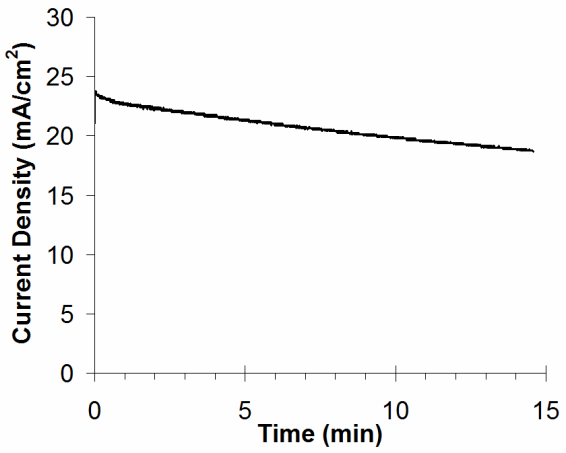

Figure 3.6.3.3: Long term oxidative current from 5 mM BH_4^- in 1 M NaOH at Pd, held at –0.5 V, rotated at 3000 rpm.

3.6.4 BH_4^- Oxidation at Ir

Ir supports surface hydrides, but its oxidation of BH_4^- was very unlike that of Pt. While the region of surface hydrides, about –1 to –0.6 V, did show oxidative activity for BH_4^-, Ir did not support the oxidation at any other potential in its limit of solvent stability (Figure 3.6.4.1). Current generated at these potentials did show some increase with rotation rate (Figure 3.6.4.2), indicating that at least some of the current was due to a diffusional process, but the increase was less than expected for a fully diffusional process. A great deal of the current, then, was probably from a surface adsorptive process. Current was not sustained across time (Figure 3.6.4.3), suggesting that the adsorptive process may be irreversible and therefore self-poisoning at low potential. As with Pt, Pd, and Au, the self-poisoning is likely reversible upon formation of surface oxide. Overall, the current observed was less than five times lower than that expected for the 8 e^- oxidation of BH_4^-, and about three times lower than that recorded at Pd at similar potentials (Figure 3.6.3.2).

The results for Ir were quite disappointing, at this is one of the most similar metals to Pt in terms of density, electronic states, and surface features. While Ir is unlikely to serve as a promising BH_4^- catalyst by itself, it may provide low-potential current as part of an alloy.

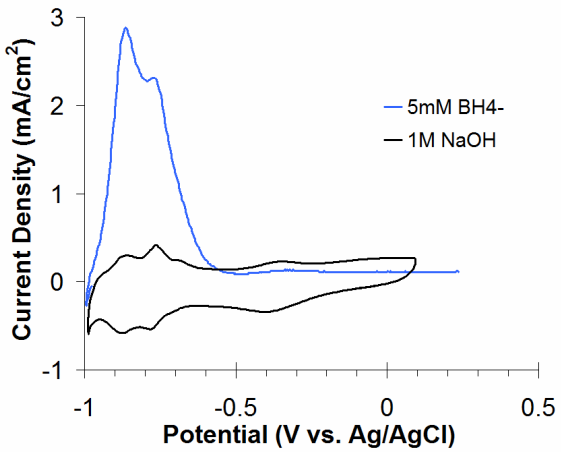

Figure 3.6.4.1: CV's of 5 mM BH_4^- in 1 M NaOH at Ir, and the Ir electrode in 1 M NaOH without any fuel present, revealing Ir surface features, 20 mV/s.

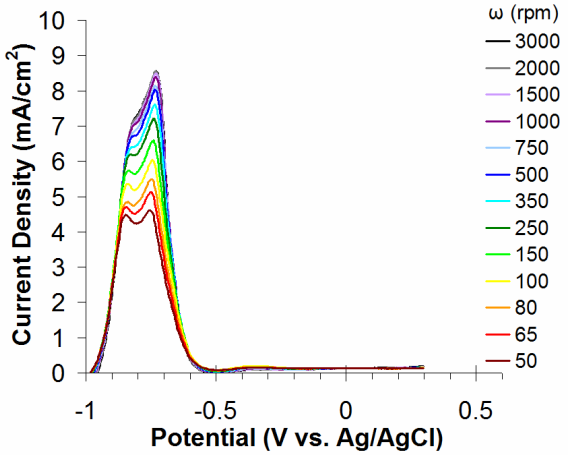

Figure 3.6.4.2: RDE voltammograms of 5 mM BH_4^- in 1 M NaOH at Ir, anodic sweeps, 20 mV/s.

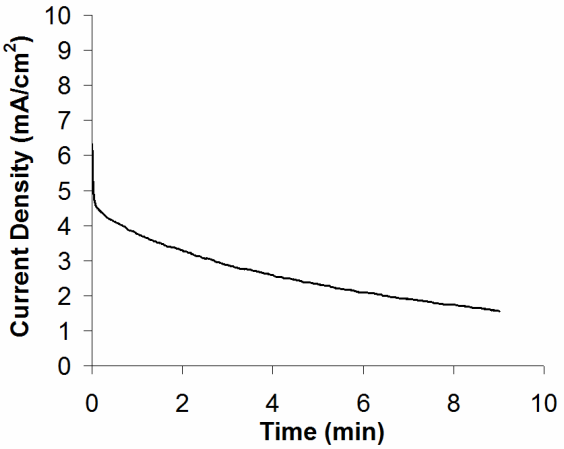

Figure 3.6.4.3: Long term oxidative current from 5 mM BH_4^- in 1 M NaOH at Ir, held at –0.85 V, rotated at 100 rpm.

3.6.5 BH_4^- Oxidation at Ru

Like Ir and Pd, Ru also shows low-potential oxidative activity for H_2, and as such was expected to show low-potential oxidation of BH_4^-. Unfortunately, like Ir, Ru's oxidation of BH_4^- exists only in this low-potential region, from about –1 to –0.7 V (Figure 3.6.5.1), and the overall current density observed was about as low as seen at Ir (Figure 3.6.4.2). An RDE voltammogram was performed at 3000 rpm only (Figure 3.6.5.2), as this current was found to quickly deteriorate with time, approximately ten times faster than poisoning seen at Ir (Figure 3.6.5.3 compared to Figure 3.6.4.3), and further analysis was not performed due to time constraints. Like Ir, Ru may add low-potential BH_4^- alloys, but is unlikely to serve as a BH_4^- catalyst on its own.

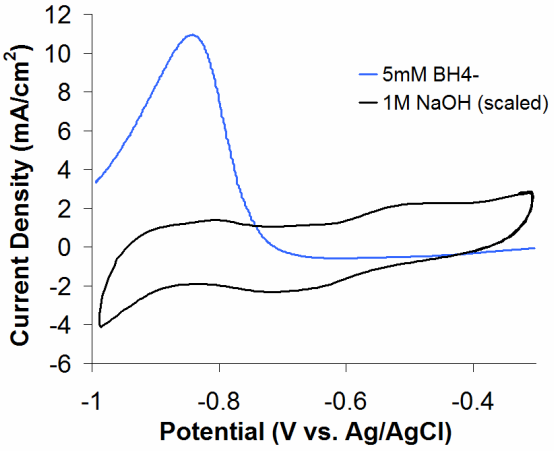

Figure 3.6.5.1: CV's of 5 mM BH_4^- in 1 M NaOH at Ru, and the Ru electrode in 1 M NaOH without any fuel present, scaled to show Ru surface features, 20 mV/s.

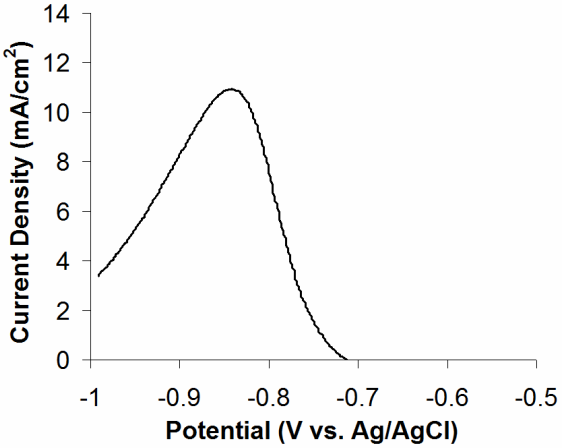

Figure 3.6.5.2: RDE voltammogram of 5 mM BH_4^- in 1 M NaOH at Ru, 3000 rpm, anodic sweep, 20 mV/s.

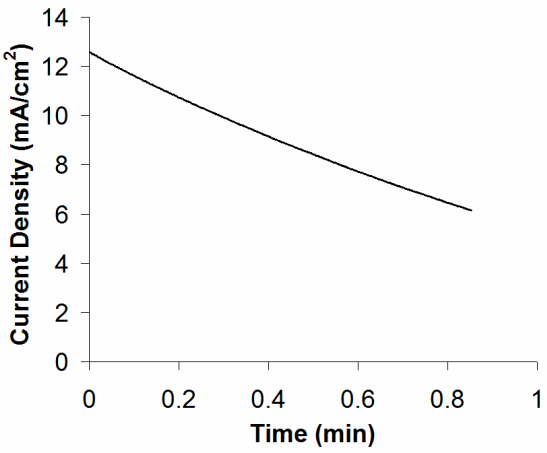

Figure 3.6.5.3: Long term oxidative current from 5 mM BH_4^- in 1 M NaOH at Ru, held at –0.85 V, rotated at 3000 rpm.

3.6.6 Conclusions for BH_4^- Oxidation at Alternative Metals

A summary of the performance of all BH_4^- oxidation catalysts studied herein is presented in Figure 3.6.6.1. It is clear that while this wide variety of metals does have the ability to oxidize BH_4^-, most metals do not have anywhere near the catalytic ability of Pt or Au, and finding a more affordable BH_4^- catalyst will not be trivial. Ag shows significant current, but only at high potentials, and does not reach transport-limited current before it begins to corrode. As predicted from our previous study, the Pt-group metals Pd, Ru, and Ir did show low-potential oxdation of BH_4^-. However, BH_4^- oxidation at Ru and Ir may be an inactivating surface adsorption, meaning that current does not scale correctly with mass transport, decreasing the viability of these materials as catalysts. Oddly, though Ni showed the poorest oxidative catalysis for BH_4^- of all of the metals studied, it is by far the most cost-effective, as it delivered about twenty times less current than Pt for a price reduction of over three orders of magnitude (Table 3.6.1). The real discovery here was Pd, which offered comparable, though reduced, performance as compared to

Pt or Au, but at half the price of either. Pd's RDE voltammogram is quite complex, and all of the materials will need significant further study to elucidate their oxidative mechanisms for BH_4^-.

Even this preliminary data already allows us to prepare to study binary alloys for BH_4^- oxidation activity. Metals that have either low or high potential oxidations, such as Ir and Ag, or Pd and Au, could be combined to deliver current at a wider variety of potentials. Materials that support surface oxides at lower potential, such as Ni, could be combined with Pt, so as to assist in removing Pt's surface poisons, perhaps without the need for the pulse-cleaning method described in Section 3.5. Further investigation in this area will be critical to establishing superior catalysts for BH_4^- oxidation.

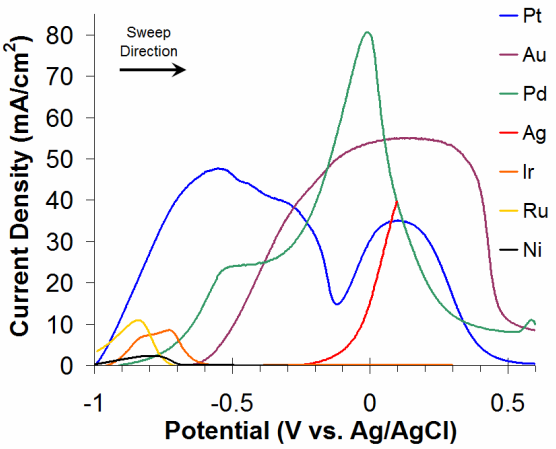

Figure 3.6.6.1: RDE performance comparison of alternative BH_4^- fuel cell catalysts. Activities are shown for 5 mM BH_4^- in 1 M NaOH, 3000 rpm, anodic sweeps, at 20 mV/s.

3.7 Acknowledgments

The authors gratefully acknowledge support from the Office of Basic Energy Sciences, Division of Materials Sciences, U.S. Department of Energy, under Grant DE-FG02-05ER46250.

3.8 References

(1) Raman, R. K.; Choudhury, N. A.; Shukla, A. K. *Electrochem. Solid. St.* **2004**, *7*, A488-A491.

(2) Li, Z. P.; Liu, B. H.; Arai, K.; Suda, S. *J. Electrochem. Soc.* **2003**, *150*, A868-A872.

(3) Lee, S. M.; Kim, J. H.; Lee, H. H.; Lee, P. S.; Lee, J. Y. *J. Electrochem. Soc.* **2002**, *149*, A603-A606.

(4) Ponce de León, C.; Walsh, F. C.; Rose, A.; Lakeman, J. B.; Browning, D. J.; Reeve, R. W. *J. Power Sources* **2007**, *164*, 441-448.

(5) Miley, G. H.; Luo, N.; Mather, J.; Burton, R.; Hawkins, G.; Gu, L.; Byrd, E.; Gimlin, R.; Shrestha, P. J.; Benavides, G.; Laystrom, J.; Carroll, D. *J. Power Sources* **2007**, *165*, 509-516.

(6) Raman, R. K.; Prashant, S. K.; Shukla, A. K. *J. Power Sources* **2006**, *162*, 1073-1076.

(7) Ponce de León, C.; Walsh, F. C.; Pletcher, D.; Browning, D. J.; Lakeman, J. B. *J. Power Sources* **2006**, *155*, 172-181.

(8) Liu, B. H.; Li, Z. P. *J. Power Sources* **2009**, *187*, 291-297.

(9) Latimer, W. M. *Oxidation Potentials*; 2nd ed.; Prentice-Hall, Inc.: Englewood Cliffs, NJ, 1938.

(10) Gardiner, J. A.; Collat, J. W. *J. Am. Chem. Soc.* **1965**, *87*, 1692-1700.

(11) Ye, W.; Zhang, H.; Xu, D.; Ma, L.; Yi, B. *J. Power Sources* **2007**, *164*, 544-548.

(12) Langmi, H. W.; McGrady, G. S. *Coord. Chem. Rev.* **2007**, *251*, 925-935.

(13) Peña-Alonso, R.; Sicurelli, A.; Callone, E.; Carturan, G.; Raj, R. *J. Power Sources* **2007**, *165*, 315-323.

(14) Zhang, J.; Zheng, Y.; Gore, J. P.; Fisher, T. S. *J. Power Sources* **2007**, *165*, 844-853.

(15) Liu, B. H.; Li, Z. P. *J. Power Sources* **2009**, *187*, 527-534.

(16) Stockmayer, W. H.; Rice, D. W.; Stephenson, C. C. *J. Am. Chem. Soc.* **1955**, *77*, 1980-1983.

(17) Elder, J. P.; Hickling, A. *Trans. Faraday Soc.* **1962**, *58*, 1852-1864.

(18) Elder, J. P. *Electrochim. Acta* **1962**, *7*, 417-426.

(19) Morris, J. H.; Gysling, H. J.; Reed, D. *Chem. Rev.* **1985**, *85*, 51-76.

(20) Mirkin, M. V.; Yang, H.; Bard, A. J. *J. Electrochem. Soc.* **1992**, *139*, 2212-2217.

(21) Krishnan, P.; Yang, T. H.; Advani, S. G.; Prasad, A. K. *J. Power Sources* **2008**, *182*, 106-111.

(22) Liu, B. H.; Li, Z. P.; Suda, S. *Electrochim. Acta* **2004**, *49*, 3097-3105.

(23) Bard, A. J.; Faulkner, L. R. *Electrochemical Methods*; 2nd ed.; John Wiley & Sons, Inc.: New York, NY, 2001.

(24) Gyenge, E. *Electrochim. Acta* **2004**, *49*, 965-978.

(25) Gardiner, J. A.; Collat, J. W. *Inorg. Chem.* **1965**, *4*, 1208-1212.

(26) Sadik, O. A.; Xu, H.; Sargent, A. *J. Electroanal. Chem.* **2005**, *583*, 167-175.

(27) Nagle, L. C.; Rohan, J. F. *Electrochem. Solid. St.* **2005**, *8*, C77-C80.

(28) Nagle, L. C.; Rohan, J. F. *J. Electrochem. Soc.* **2006**, *153*, C773-C776.

(29) Dong, H.; Feng, R.; Ai, X.; Cao, Y.; Yang, H.; Cha, C. *J. Phys. Chem. B* **2005**, *109*, 10896-10901.

(30) Mirkin, M. V.; Bard, A. J. *Anal. Chem.* **1991**, *63*, 532-533.

(31) Denuault, G.; Mirkin, M. V.; Bard, A. J. *J. Electroanal. Chem.* **1991**, *308*, 27-38.

(32) Kiekens, P.; Steen, L.; Donche, H.; Temmerman, E. *Electrochim. Acta* **1981**, *26*, 841-845.

(33) Okinaka, Y. *J. Electrochem. Soc.* **1973**, *120*, 739-744.

(34) Ponce de León, C.; Bavykin, D. V.; Walsh, F. C. *Electrochem. Commun.* **2006**, *8*, 1655-1660.

(35) Chatenet, M.; Micoud, F.; Roche, I.; Chainet, E. *Electrochim. Acta* **2006**, *51*, 5459-5467.

(36) Cheng, H.; Scott, K. *Electrochim. Acta* **2006**, *51*, 3429-3433.

(37) Atwan, M. H.; Macdonald, C. L. B.; Northwood, D. O.; Gyenge, E. L. *J. Power Sources* **2006**, *158*, 36-44.

(38) Chatenet, M.; Molina-Concha, M. B.; Diard, J. P. *Electrochim. Acta* **2009**, *54*, 1687-1693.

(39) Amendola, S. C.; Onnerud, P.; Kelly, M. T.; Petillo, P. J.; Sharp-Goldman, S. L.; Binder, M. *J. Power Sources* **1999**, *84*, 130-133.

(40) Sargent, A.; Sadik, O. A.; Matienzo, L. J. *J. Electrochem. Soc.* **2001**, *148*, C257-C265.

(41) Zhang, X. B.; Han, S.; Yan, J. M.; Chandra, M.; Shioyama, H.; Yasuda, K.; Kuriyama, N.; Kobayashi, T.; Xu, Q. *J. Power Sources* **2007**, *168*, 167-171.

(42) Demirci, U. B. *J. Power Sources* **2007**, *172*, 676-687.

(43) Colominas, S.; McLafferty, J.; Macdonald, D. D. *Electrochim. Acta* **2009**, *54*, 3575-3579.

(44) Pecsok, R. L. *J. Am. Chem. Soc.* **1953**, *75*, 2862-2864.

(45) Chatenet, M.; Molina-Concha, M. B.; El-Kissi, N.; Parrour, G.; Diard, J. P. *Electrochim. Acta* **2009**, *doi:10.1016/jelectacta.2009.03.019*.

(46) Bruckenstein, S.; Feldman, G. A. *J. Electroanal. Chem.* **1965**, *9*, 395-399.

(47) Prater, K. B.; Bard, A. J. *J. Electrochem. Soc.* **1970**, *117*, 207-213.

(48) Burke, L. D.; Lee, B. H. *J. Appl. Electrochem.* **1992**, *22*, 48-56.

(49) Molina-Concha, B.; Chatenet, M.; Coutanceau, C.; Hahn, F. *Electrochem. Commun.* **2009**, *11*, 223-226.

(50) Martins, J. I.; Nunes, M. C. *J. Power Sources* **2008**, *175*, 244-249.

(51) Martins, J. I.; Nunes, M. C.; Koch, R.; Martins, L.; Bazzaoui, M. *Electrochim. Acta* **2007**, *52*, 6443-6449.

(52) Wang, K.; Jiang, K.; Lu, J.; Zhuang, L.; Cha, C.; Hu, X.; Chen, G. Z. *J. Power Sources* **2008**, *185*, 892-894.

(53) Li, Z. P.; Liu, B. H.; Zhu, J. K.; Suda, S. *J. Power Sources* **2006**, *163*, 555-559.

(54) Gyenge, E.; Atwan, M.; Northwood, D. *J. Electrochem. Soc.* **2006**, *153*, A150-A158.

(55) Ivanov, M. V.; Tsionskii, M. V. *Elektrokhimiya (Soviet Electrochemistry)* **1989**, *25*, 514-516.

(56) Celikkan, H.; Sahin, M.; Aksu, M. L.; Veziroglu, T. N. *Int. J. Hydrogen Energy* **2007**, *32*, 588-593.

(57) Gao, L.; Conway, B. E. *Electrochim. Acta* **1994**, *39*, 1681-1693.

(58) Maoka, T.; Enyo, M. *Surf. Technol.* **1979**, *9*, 147-157.

(59) Yang, C. C.; Li, Y. J.; Chiu, S. J.; Lee, K. T.; Chien, W. C.; Huang, C. A. *J. Power Sources* **2008**, *184*, 95-98.

(60) Finkelstein, D. A.; Mota, N. D.; Cohen, J. L.; Abruña, H. D. *J. Phys. Chem. C.* **2009**, *113*, 19700-19712.

(61) Ma, J.; Choudhury, N. A.; Sahai, Y. *Renewable and Sustainable Energy Reviews* **2010**, *14*, 183-199.

Chapter 4: Electro-oxidation of BH_4^- in Dimethylsulfoxide and Dimethylformamide Studied by Rotating Disk Electrode (RDE) Voltammetry

Publication: **2011** *J. Power Sources*, doi:10.1016/j.jpowsour.2011.03.034

Personnel: David A. Finkelstein,[I] David J. Jones,[I] Kenneth Hernandez-Burgos, Héctor D. Abruña.

Department of Chemistry and Chemical Biology, Baker Laboratory, Cornell University, Ithaca, New York 14853-1301

Borohydride (BH_4^-) is a promising new fuel for fuel cells, yet its practical implementation has been hindered by a deleterious hydrolysis reaction to form H_2 in aqueous solvents, especially at the high BH_4^- concentrations necessary for high-power fuel cells. We investigated a wide array of nonaqueous solvents for their ability to hold BH_4^- at higher concentrations and allow effective electro-oxidation at Pt and Au, two well-studied BH_4^- anode materials. Only dimethylsulfoxide and dimethylformamide were found to be suitable, and precluded BH_4^- decomposition to H_2 in bulk solution (hydrolytic or otherwise). BH_4^- decomposition at electrode surfaces was still observed, however. Current densities in these solvents were about an order of magnitude below those observed in aqueous solution, and onset potentials were 0.7 V less favorable. MeOH addition, to stabilize oxidized states of boron, did not increase current.

[I] Both authors contributed equally to this work.

4.1 BH_4^- Oxidation in Nonaqueous Solvents Introduction:

Borohydride (BH_4^-) has attracted intense attention as a high-power fuel, either used directly or indirectly (via hydrolysis to H_2) to generate power in fuel cells.[1,2] The power and energy density available come from its low onset potential (–1 V vs. Ag/AgCl at Pt), fast kinetics for oxidation,[3] high aqueous solubility (14.5 M[4]) and diffusion coefficient (1.67×10^{-5} cm^2 s^{-1} [5]), and the ability to provide up to $8e^-$:[6]

$$BH_4^- + 8OH^- \rightarrow BO_2^- + 6H_2O + 8e^- \qquad \textbf{[4.1.a]}$$

Unfortunately, utilization of direct BH_4^- oxidation is plagued by its hydrolysis to H_2, which occurs in aqueous solution, especially at low pH, and is also catalyzed at Pt surfaces.[7] Hydrolysis can consume up to all $8e^-$, although partial hydrolysis to practically any electron count is possible:[8]

$$BH_4^- + 2H_2O \rightarrow BO_2^- + 4H_2 \qquad \textbf{[4.1.b]}$$

Though the hydrolysis can be slowed at high pH, it proceeds even at pH 14[7], and hydrolysis is first order with respect to $[BH_4^-]$[6,8]. This becomes rather deleterious, as hydrolysis is enhanced at the greater $[BH_4^-]$ practical and necessary for to high-power fuel cell development.

The most logical solution to hydrolysis, then, would be to remove water from the system altogether, and operate in a nonaqueous solvent instead. Since facile syntheses for BH_4^- compounds were first discovered,[9] BH_4^- has been employed a reducing agent for many organic syntheses, and, as such, has been used in a variety of nonaqueous solvents.[10] However, BH_4^-

solutions were not always stable in these studies; even if BH_4^- made only a suspension, or decomposed in the solvent, it could still perform the reaction, and the total utilization efficiency of BH_4^- was not always the highest priority. $NaBH_4$ was found to be soluble in both MeOH and EtOH, but unfortunately decomposed to H_2 in both. The methanolysis reaction was rapid, whereas the ethanolysis was much slower.[11,12] As with the hydrolysis, the methanolysis was first order with respect to $[BH_4^-]$.[11] $NaBH_4$ has been shown to form a suspension in tetrahydrofuran (THF),[13] i-PrOH, and t-BuOH.[14] Brown et al. observed that solutions/suspensions of $NaBH_4$ in i-PrOH, diethylene glycol dimethyl ether (diglyme) and triglyme did not undergo BH_4^- decomposition to H_2,[15] though Lalancette et al. observed H_2 formation when making sulfurated borohydrides in THF, diglyme, and other solvents.[16,17] Other BH_4^- reactions have been carried out in ether[18], dioxane,[12,19] ethyl ether, isopropyl ether, hexamethyl phosphoric triamide, diethylamine, triethylamine, carbon disulfide, dimethylsulfoxide (DMSO), benzene, and various other alcohols and ketones.[16] Sigma-Aldrich© currently sells solutions of $NaBH_4$ in diglyme (0.5 M), triglyme (2.0 M), and tetraglyme (3 M).

As will be discussed below, we found great difficulty in obtaining expected current densities from BH_4^- in several of these solvents, and we speculated that BH_4^-'s fully oxidized form, BO_2^- or $B(OH)_4^-$,[3] may not easily form in solvents without a ready supply of oxy-ions, preventing the full $8e^-$ from being obtained. If this is the case, the stability and ease of formation of boron's solvation shell may be critical to determining current efficiency in a nonaqueous BH_4^- fuel cell. Previously, it was observed that BH_4^- is oxidized to $B(OCH_3)_4^-$ in MeOH,[11,13,20] and that BH_4^-'s reducing activity was influenced by the type of alcohol present to act as a ligand to its oxidized form.[20] Thus, we also attempted adding small amounts of MeOH to the system, with the goal of facilitating formation of the fully oxidized $B(OCH_3)_4^-$ complexes.

4.2 Experimental Methods

4.2.1 Reagents and solutions

All chemicals used were reagent grade, and included sodium borohydride ($NaBH_4$), 98%, potassium borohydride (KBH_4), 97%, high-purity sulfuric acid, 99.999%, tetrabutylammonium hexafluorophosphate (TBAH), 98%, dimethylformamide (DMF), 99.8%, acetonitrile, 99.8% (Sigma Aldrich), sodium nitrate ($NaNO_3$), dimethylsulfoxide (DMSO), 99.9%, methanol, 99.9%, isopropanol, 99.5%, tetrahydrofuran, 99% (Mallinckrodt), ether, 99.9%, 1-propanol (Fisher), diglyme, 99.0% (Fluka), ethanol (Pharmco-Aaper).

Electrode cleaning solutions were prepared with deionized water purified with a Barnstead Nanopure Analytical UV system (18 MΩ·cm). Organic solutions were used in open-air, without concern for solvent hydration. Electrolyte choice was based on simplicity and previous experience. $NaNO_3$ is a simple inorganic compound and worked well with DMSO, while DMF would not dissolve various perchlorate salts to 0.1 M, and instead required TBAH. Li^+ and Na^+ salts are inherently more soluble in most solvents than K^+ salts, and $LiBH_4$ is currently about ten times the price of $NaBH_4$ without offering a comparable gain in solubility, so $NaBH_4$ was selected for BH_4^- solubility assessment. $NaBH_4$ is hygroscopic and reacts with water, tending to decompose in air slowly over time. KBH_4 is non-hygroscopic,[21] and so was chosen for the analytical electrochemistry. Both sodium and potassium borohydride were stored in a desiccator to minimize any possible decomposition prior to experimentation.

4.2.2 Electrochemical setup and electrode cleaning

Experiments were carried out in a three-chambered electrochemical cell, with compartments separated by medium porosity glass frits, using a Pt-mesh counter electrode and a

Pt/PtO pseudoreference. The potential of the Pt/PtO pseudoreference was measured against an Ag/AgCl reference electrode in the corresponding solvent immediately prior to experimentation, and all potentials are referenced vs. Ag/AgCl. Rotating disk electrode voltammetry was performed using a Pine bipotentiostat (Model AFCBP1) and analytical rotor (Model AFMSRX). Electrodes were rotated between 50 and 3000 rpm. CV's were swept at 20 mV s^{-1} to obtain pseudo steady-state sweeps. All experiments were run at room temperature and pressure (25°C, 1 atm). The 3 mm Pt rotating disk electrode was polished using 1μm diamond paste (Buehler Metadi) on a polishing cloth (Buehler Microcloth). The Pt electrode was then electrochemically cleaned from –0.2 to +1.2 V vs. Ag/AgCl in 0.1 M H_2SO_4 until the characteristic voltammetric profile of polycrystalline Pt was obtained. The 5 mm Au rotating disk electrode was polished using a series of 1 and 0.3 μm α-alumina and 0.05 μm γ-alumina polishes (Buehler Micropolish). The Au electrode was then electrochemically cleaned from 0.0 to +1.35 V vs. Ag/AgCl in 0.1 M H_2SO_4 until the characteristic voltammetric profile of polycrystalline Au was obtained.

4.2.3 Electrochemical analysis

For our RDE analyses of BH_4^- (see Chapter 2), we have used the diffusion coefficient for BH_4^- determined by Denuault et al., 1.67×10^{-5} cm^2 s^{-1} [5]. The kinematic viscosities of DMSO solutions were based on standard values for DMSO's viscosity and density: 1.99 mPa and 1.10 g cm^{-3}, respectively.[4] Small deviances due to addition of electrolyte or analyte were neglected, as they are practically eliminated by the –1/6 power for ν. The Levich equation (Equation [2.3.1]) is valid when the system is mass-transport limited at all rotation rates used in the calculation, and this is evidenced by linearity in the Levich plot ($i_{l,a}$ vs. $\omega^{1/2}$).

In this study, both n and D_R appeared conspicuously low, and are speculated upon in the Discussion. Since D_R is significantly below a common literature value,[5] the exact value of n could not be readily obtained, and evaluation of kinetic parameters was not performed. Though techniques do exist to simultaneously determine n and D,[5,23] the results obtained herein were not promising enough to justify a more extensive analysis.

4.3 Results and Discussion

4.3.1 Solvent selection for BH_4^-

The criteria for selection of a nonaqueous solvent for BH_4^- were based on improving past fuel cell results. Our previous work showed exceptional oxidation performance for BH_4^- in basic aqueous solutions, with nearly all 8 e^- recovered at the expected D_R of 1.67×10^{-5} cm^2 s^{-1}, and, for Pt, with fast kinetics as well.[3] However, since BH_4^- decomposes to H_2 at higher concentrations, excessive base was needed to stabilize solutions of BH_4^-.[6,8] The [NaOH] was limited to about 3 M, with higher concentrations resulting in degradation of various fuel cell components. This in turn limited our [BH_4^-] to approximately 0.15 M.[24] To represent a significant improvement from our current system, we decided that BH_4^- must be soluble to > 0.4 M in a nonaqueous solvent, and that the new BH_4^- solution must not have any new problematic side effects that would diminish and/or compromise system performance.

$NaBH_4$'s solubility was tested in many solvents with a wide range of polarity (Table 4.3.1.1; see Section 4.2.1 for use of $NaBH_4$ vs. $LiBH_4$ and KBH_4). We limited the scope of this study by choosing mostly polar, common solvents, and we expect that our results can help predict $NaBH_4$'s relative solubility in many solvents not included in our analysis. This assessment of solubility was intentionally coarse and the solubilities should be treated as semi-

quantitative only. The results are obtained from simple room-temperature experiments, without heating. Complications were closely monitored and are likewise noted with the solubilities.

Solvent	BH_4^- Solubility at 25℃ (M)	Complications
DMSO	0.42	
DMF	0.43	
Acetonitrile	-	not soluble
Diglyme	0.46	suspension
Ether	-	not soluble
Methanol	0.33	bubbles
Ethanol	0.49	bubbles
Isopropanol	-	not soluble
1-propanol	-	not soluble
THF	-	not soluble

Table 4.3.1.1: Solubility of $NaBH_4$ in a variety of nonaqueous, mostly polar solvents, and complications regarding the stability of each solution.

Many of the solvents tested did not show any significant solubility for $NaBH_4$ at all, and of those that did, most had significant drawbacks for use (Table 4.3.1.1). As expected, BH_4^- decomposed to H_2 bubbles in both MeOH and EtOH, but the reactions occurred at surprisingly fast rates, precluding both solvents from practical utility. Considering the various high-concentration glyme solutions available from Sigma-Aldrich©, diglyme was rather disappointing, as the saturated solution was very cloudy, indicating that a suspension formed to some degree. Out of a fairly wide pool of solvents, we quickly narrowed our focus down to DMF and DMSO, and chose appropriate electrolytes for each (see Methods).

4.3.2 BH_4^- oxidation in DMF and DMSO

Both of our selected solvents proved very challenging to work with. The RDE voltammograms for BH_4^- oxidation often did not show standard shape or have well-defined mass-transport limited regions[22] in these solvents. Early trials were poorly reproducible (Figure 4.3.2.1). Studies at Pt in DMF often showed decreased current on later scans, indicating slow poisoning reactions (Figure 4.3.2.2). In fact, we were never able to get a clean voltammogram with DMF (Figure 4.3.2.3), preventing a more thorough quantitative analysis.

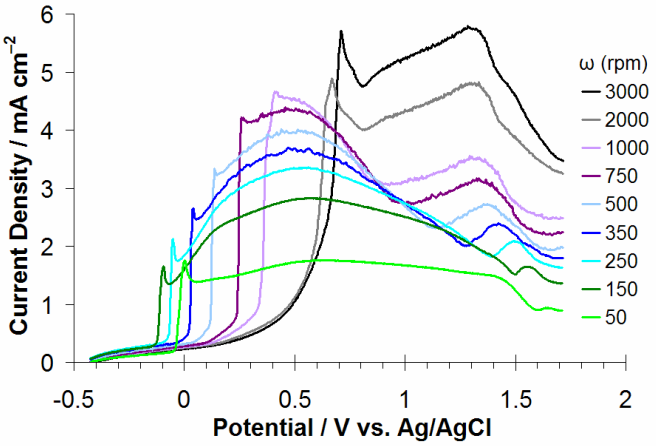

Figure 4.3.2.1: RDE voltammogram anodic sweeps of 5mM KBH_4 in DMF, 0.1 M TBAH, at a Pt disk electrode, 20 mV s^{-1}, rotated between 50-3000 rpm, swept from –0.5 to +1.7 V vs. Ag/AgCl. Additional, unknown oxidative processes occurred positive of +1.25 V.

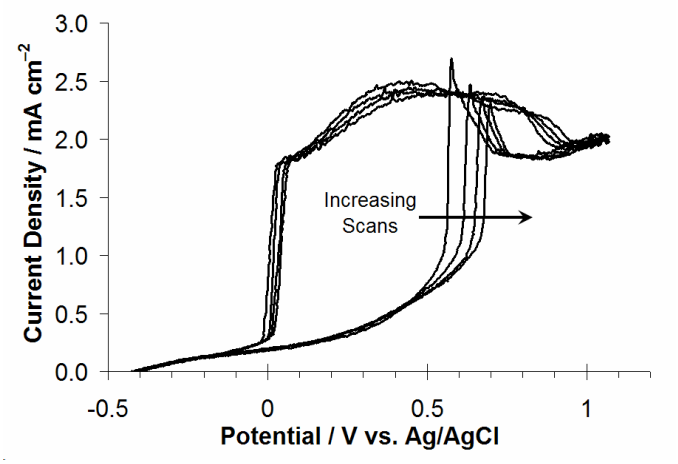

Figure 4.3.2.2: RDE voltammogram anodic sweeps of 5mM KBH_4 in DMF, 0.1 M TBAH, at a Pt disk electrode, 20 mV s^{-1}, rotated at 500 rpm, swept from –0.5 to +1.2 V vs. Ag/AgCl. Even complicating, unknown oxidative processes positive of +1.25 V were avoided, voltammograms changed slowly over time, with decreased current and increased overpotential for oxidation, likely indicating electrode poisoning.

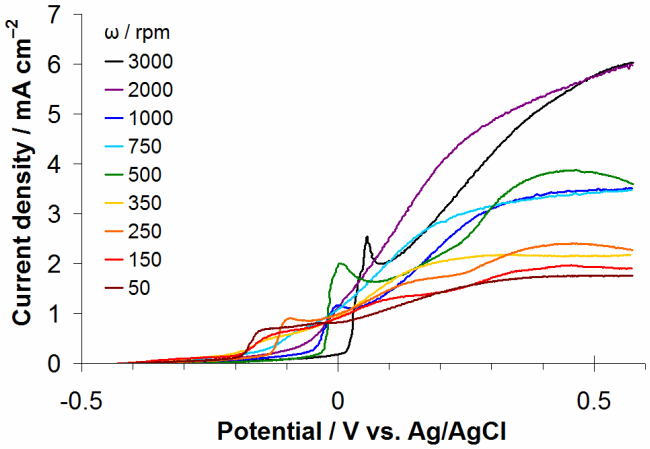

Figure 4.3.2.3: RDE voltammogram anodic sweeps of 5mM KBH_4 in DMF, 0.1 M TBAH, at a Pt disk electrode, 20 mV s^{-1}, rotated between 50-3000 rpm.

Though early trials of BH_4^- in DMSO resembled those in DMF (Figure 4.3.2.4), we were eventually able to obtain much cleaner voltammograms at Pt (Figure 4.3.2.5) by finding a more appropriate solvent window (–0.5 to +0.9 V vs. Ag/AgCl), which prevented reactions with the solvent from interfering with the current from BH_4^- oxidation. Some degree of a linear, probably resistive trend was still evident in the mass-transport-limited region of the voltammograms, but a highly linear Levich plot was nonetheless obtained (Figure 4.3.2.5, inset). The same experiment performed at Au produced i_l's about 20% higher, though the additional current was available only at higher potentials, kinetics were slower, and onset potentials were more positive (Figure 4.3.2.6). The Au voltammograms were somewhat more prone to solvent poisoning in the wider potential window used (–0.5 to +1.5 V vs. Ag/AgCl), as evidenced by increases in onset potential with time (seen here as later rotation rates, e.g. 2000 and 3000 rpm).

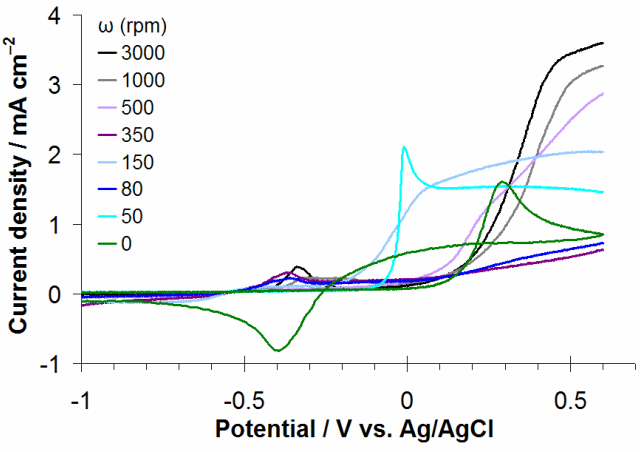

Figure 4.3.2.4: RDE voltammogram anodic sweeps of 5mM KBH_4 in DMSO, 0.1 M $NaNO_3$, at a Pt disk electrode, 20 mV s^{-1}, rotated between 0-3000 rpm, swept from –1.0 to +0.6 V vs. Ag/AgCl. Adjusting the sweeping range to higher potentials seemed to avoid unknown solvent reactions at low potential and allow more stable oxidation of BH_4^- at high potentials.

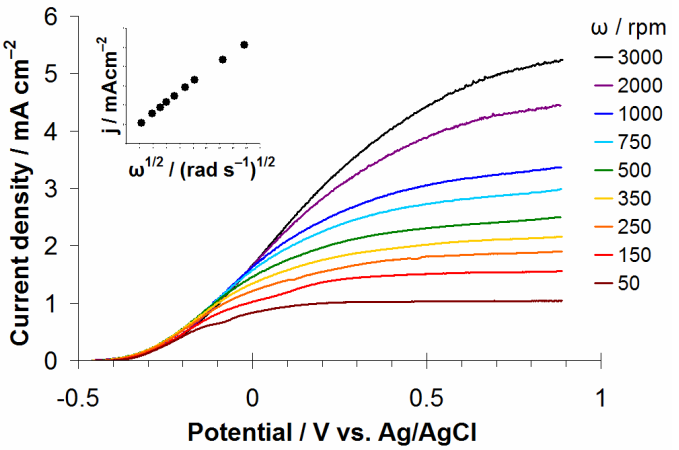

Figure 4.3.2.5: RDE voltammogram anodic sweeps of 5mM KBH_4 in DMSO, 0.1 M $NaNO_3$, at a Pt disk electrode, 20 mV s^{-1}, rotated between 50-3000 rpm. Inset: Levich plot sampled at E = +0.8 V.

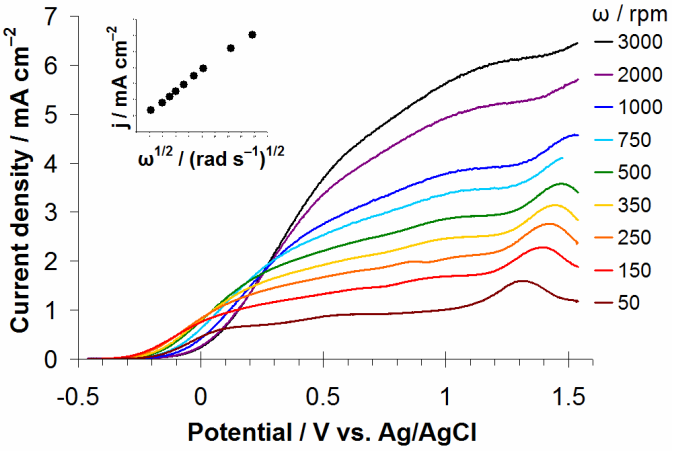

Figure 4.3.2.6: RDE voltammogram anodic sweeps of 5mM KBH_4 in DMSO, 0.1 M $NaNO_3$, at an Au disk electrode, 20 mV s^{-1}, rotated between 50-3000 rpm. Inset: Levich plot sampled at E = +1.2 V.

These observed currents, however, were well below expectation. Our previous study of BH_4^- oxidation in 1 M NaOH (base) at Pt and Au produced current densities above 50 mA cm^{-2},[3]

while those observed in this investigation are approximately 10 times lower (Figure 4.3.2.7), and occur at potentials 0.2 – 0.5 V more positive (less favorable). These initial results suggest that DMSO and DMF significantly diminish fuel cell power obtainable from BH_4^- oxidation.

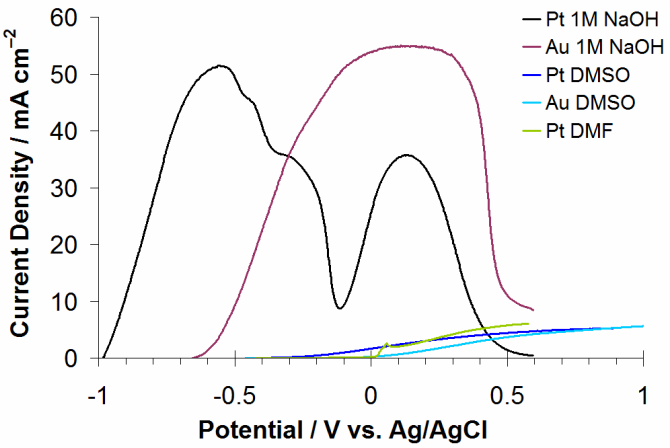

Figure 4.3.2.7: Comparison of BH_4^- oxidation at Pt and Au in 1 M $NaOH_{(aq)}$ (5 mM $NaBH_4$, 25 mV s^{-1}), in DMSO with 0.1 M $NaNO_3$, and in DMF with 0.1 M TBAH (5 mM KBH_4, 20 mV s^{-1}). RDE voltammogram anodic sweeps are shown at 3000 rpm, anodic sweeps only.

As many terms in the Levich equation were standard between base and DMSO, the decrease in current must be due to changes in either n, D_R, or ν. The change in ν is fairly insignificant; though $\nu_{1\text{ M NaOH}} = 1.2\text{x}10^{-2}$ cm^2 s^{-1} and $\nu_{DMSO} = 1.8\text{x}10^{-2}$ cm^2 s^{-1} (inferred from various tables in Lide[4]), these values are raised to the –1/6 power in the Levich equation (see Methods), making the terms in the final expression nearly identical. The current decrease must then be due to either D_R or n, implying either a change in solvent interaction or reaction mechanism, respectively. Typically, D has minimal variance from 10^{-5} cm^2 s^{-1}, even across wide ranges of polarity of solute,[4] and by extension, polarity of solvent. If n dropped from 8[3] to only 1 e$^-$, D_R would have had to decrease by 40% from $1.7\text{x}10^{-5}$ to $1.0\text{x}10^{-5}$ cm^2 s^{-1}. Since $n < 1$

is rather unlikely,[II] and $n > 1$ implies an even larger decrease in D_R, it can be concluded that BH_4^- had weaker solvent interaction in DMSO than in base. Since $D_R < 5x10^{-7}$ cm^2 s^{-1} would be required for $n = 8$, which represents an essentially unphysically small value for D_R, it is clear that n for BH_4^- oxidation is lower in DMSO than in base, suggesting that DMSO mechanistically hinders the BH_4^- oxidation pathway. There do exist procedures to determine n and D_R simultaneously when given C_R^*, such as comparison of transient and steady-state responses from an ultramicroelectrode,[5] or comparison of the slope and intercept from hydrodynamic chronocoulometry.[23] Given that the results obtained suggest that DMSO is not an ideal solvent for BH_4^- fuel cells, we did not feel that further analysis would yield actionable information, and these techniques were not attempted.

Our cursory analysis of n and D does suggest, however, that BH_4^-'s n in DMSO is probably very small, and improvement of BH_4^-'s oxidation mechanism in DMSO could yield significantly higher current densities. As described in the Introduction, previous studies found that BH_4^- coordinated methoxy groups during its oxidation, and the nature of such alcohol-derived ligands influenced BH_4^-'s reactivity. We hypothesized that, because BH_4^- had a comparatively weak solvent interaction with DMSO, it may not coordinate DMSO effectively in its oxidized state. Thus, availability of MeOH to promote formation of the fully oxidized form $B(OCH_3)_4^-$ could result in a higher n and therefore increased current from BH_4^-'s oxidation.

[II] The most probable case for $n < 1$ would be dimer formation ($n = 0.5$), but this would require $D = 3x10^{-5}$ cm^2 s^{-1}, which is physically very unlikely.

4.3.3 Effect of MeOH on BH_4^- oxidation in DMSO

To examine the effect of adding MeOH to the system, we first assessed whether MeOH would produce its own current, serving as a second fuel in solution. No significant current was obtained from MeOH oxidation in the absence of BH_4^- within the potential range studied (Figure 4.3.3.1). Any current increase from MeOH addition was therefore due to enhanced BH_4^- oxidation only.

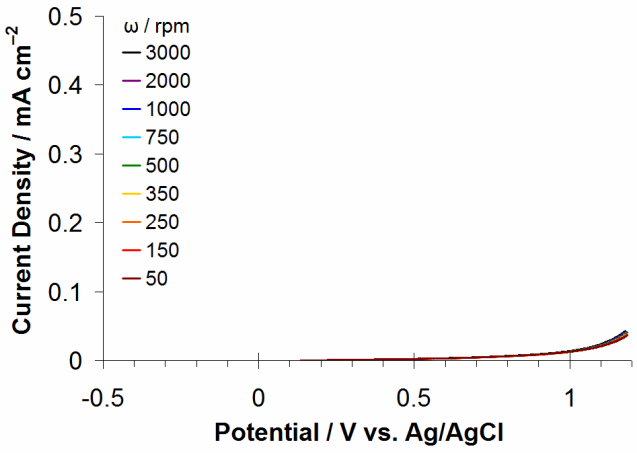

Figure 4.3.3.1: RDE voltammogram anodic sweeps of 5mM MeOH in DMSO, 0.1 M $NaNO_3$, at a Pt disk electrode, 20 mV s^{-1}, rotated between 50-3000 rpm. MeOH did not produce any significant current in the potential range studied, and any current increase in BH_4^- voltammograms is due to MeOH's action as a ligand, rather than its oxidation as a second fuel.

Addition of equimolar (5 mM) MeOH at first appeared to increase BH_4^-'s limiting current density by about 10% (from 5.2 to 5.7 mA cm^{-2} in Figures 4.3.2.5 and 4.3.3.2, respectively). Since MeOH appeared to boost current, perhaps by serving as a single coordinating ligand, we then tried adding MeOH in a 4:1 molar ratio with BH_4^- to allow formation of the four-coordinate

species, $B(OCH_3)_4^-$. In case MeOH had low activity in DMSO, we added 50% extra MeOH (30 instead of 20 mM), to ensure saturation of any current-boosting effect from coordination. Instead of further increasing current, 30 mM MeOH actually decreased currents to their original levels (Figure 4.3.3.3). Considering that we had a small degree of variance in currents across multiple trials, it is likely that the current increase observed with 5 mM MeOH falls within experimental error, and that MeOH addition has no significant effect on BH_4^- oxidation in DMSO. The trials with and without MeOH that are most similar are shown in Figure 4.3.3.4.

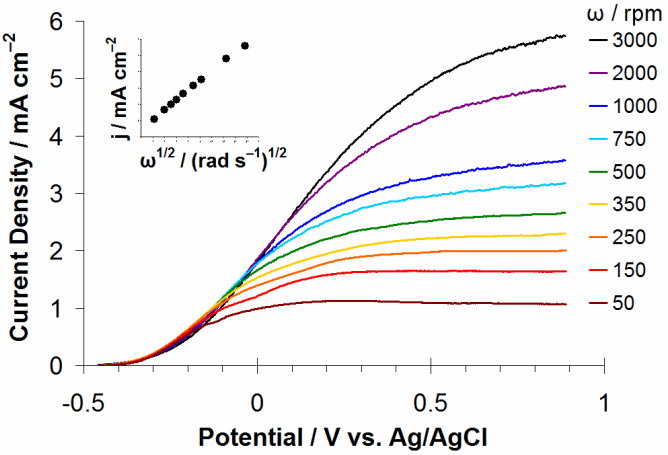

Figure 4.3.3.2: RDE voltammogram anodic sweeps of 5mM KBH_4 with 5mM MeOH in DMSO, 0.1 M $NaNO_3$, at a Pt disk electrode, 20 mV s^{-1}, rotated between 50-3000 rpm. Inset: Levich plot sampled at E = +0.8 V.

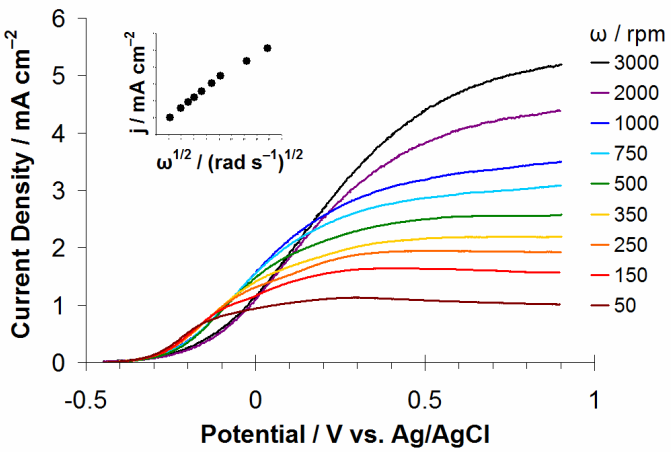

Figure 4.3.3.3: RDE voltammogram anodic sweeps of 5mM KBH_4 with 30mM MeOH in DMSO, 0.1 M $NaNO_3$, at a Pt disk electrode, 20 mV s^{-1}, rotated between 50-3000 rpm. Inset: Levich plot sampled at E = +0.85 V.

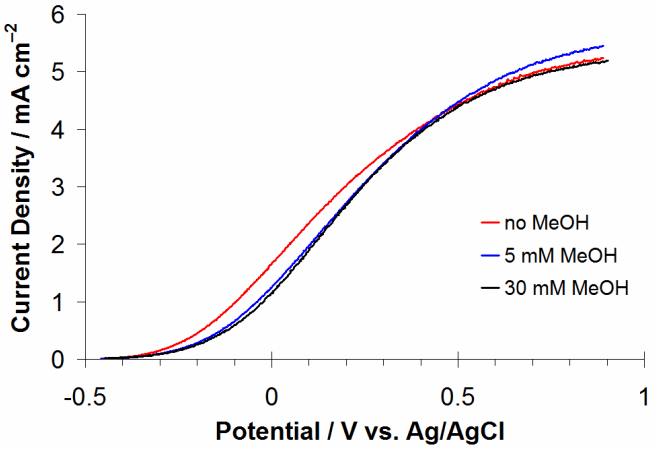

Figure 4.3.3.4: Comparison of RDE voltammogram anodic sweeps of 5mM KBH_4 in DMSO, 0.1M $NaNO_3$, at a Pt disk electrode, 20 mV s^{-1}, rotated at 3000rpm, with 0, 5, and 30mM MeOH added.

4.3.4 Solvent effects on BH_4^- hydrolysis, electron recovery, and diffusivity

Although we were unable to increase BH_4^-'s oxidative current in DMSO to levels seen in base, both DMSO and DMF were able to successfully dissolve large quantities of $NaBH_4$ without permitting homogeneous or passive heterogeneous BH_4^- hydrolysis. No bubbles were evident during solubility tests, with $[BH_4^-] > 0.4$ M, nor at electrode surfaces in 5 mM BH_4^- solutions at open circuit. In contrast, basic solutions of just 5mM BH_4^- will quickly and visibly (via bubbles) be hydrolyzed at Pt oxide at open circuit. Unfortunately, we noticed that heterogeneous hydrolysis at both Pt and Au still occurred vigorously upon oxidative current discharge, with bubbles quickly covering the electrode surfaces. Thus, even in an environment with minimal $[H_2O]$, BH_4^- either reacts with trace amounts of H_2O or uses its own H atoms to produce to H_2.

It is unclear why Au was able to produce a larger i_l for BH_4^- oxidation in DMSO than Pt (Figures 4.3.2.5 and 4.3.2.6). This would imply that n was 20% larger in BH_4^-'s oxidation mechanism at Au vs. Pt. This sort of proportionality would best be explained by an increase in n from 5 to 6, but the corresponding D_R would be $1x10^{-6}$ cm^2 s^{-1}, which is exceptionally small. Given that Au can significantly improve n, perhaps other catalysts will increase the available current from BH_4^- in nonaqueous solvents. It would be nontrivial, however, to find a catalyst that could improve current densities by 10 times to reach existing current densities in base. Furthermore, a low value for D_R would strictly limit i_l regardless of the catalyst employed, and suggest that the first step to improving current would be finding a more suitable solvent.

4.4 Conclusions

The nonaqueous solvents DMSO and DMF were found to provide a fuel cell environment that helped mitigate, but did not eliminate, complications arising from BH_4^-'s catalytic decomposition to H_2. Though homogeneous and passive heterogeneous decomposition were prevented, Pt and Au both produced H_2 from BH_4^- upon passage of current, as they do in basic, aqueous solutions.

Using nonaqueous solvents for electrochemical reactions at noble metals is inherently challenging. Both DMSO and DMF interacted with Pt and Au surfaces, resulting in unexpected poisoning and side reactions, which limited the electrical potential window in which they could operate. DMF was unable to support a reproducible oxidation of BH_4^- under any of the conditions studied. Additionally, there may exist complications in achieving high conductivity in DMSO[25] and DMF,[26] although further discussion lies outside the scope of this investigation. While highly concentrated mixtures of $NaBH_4$ can be prepared in various glymes, $NaBH_4$ – saturated diglyme appeared to be a suspension, rather than a solution, and would not be expected to be a good medium for heterogeneous catalysis. Thus, solutions that work well for synthetic organic chemistry will not necessarily yield facile solvent systems for heterogeneous, electrochemical reactions.

The oxidations of BH_4^- in DMSO and DMF were found to produce ten times less current and 0.7 V less voltage than in 1 M NaOH, indicating that DMSO and DMF are not ideal solvents for BH_4^- fuel cells. The exceptionally low current observed is due to decreases in both n and D_R for BH_4^- oxidation. Current densities in DMSO were about 20% higher at Au than at Pt, suggesting that BH_4^- undergoes a more complete oxidation at Au in this solvent. Though literature suggested that MeOH could provide methoxy ligands to stabilize BH_4^-'s oxidized state

and affect its reactivity, addition of MeOH was not observed to increase the current obtained from BH_4^-.

The results herein demonstrate that neither DMSO nor DMF will completely solve complications in BH_4^- fuel cells arising from BH_4^-'s decomposition to H_2. Future solutions may involve finding better solvents that decrease hydrolysis but do not impact n or D_R, developing aqueous additives that stabilize BH_4^-, or implementing engineering solutions that allow unmitigated fuel cell operation irrespective of copious bubble formation.

4.5 Acknowledgments

The authors gratefully acknowledge support from the Office of Basic Energy Sciences, Division of Materials Sciences, U.S. Department of Energy, under Grant DE-FG02-05ER46250.

4.6 References

(1) Ma, J.; Choudhury, N. A.; Sahai, Y. *Renewable and Sustainable Energy Reviews* **2010**, *14*, 183-199.

(2) Liu, B. H.; Li, Z. P. *J. Power Sources* **2009**, *187*, 527-534.

(3) Finkelstein, D. A.; Mota, N. D.; Cohen, J. L.; Abruña, H. D. *J. Phys. Chem. C.* **2009**, *113*, 19700-19712.

(4) *CRC Handbook of Chemistry and Physics*; 90th ed.; Lide, D. R., Ed.; CRC Press: Boca Raton, FL, 2010.

(5) Denuault, G.; Mirkin, M. V.; Bard, A. J. *J. Electroanal. Chem.* **1991**, *308*, 27-38.

(6) Pecsok, R. L. *J. Am. Chem. Soc.* **1953**, *75*, 2862-2864.

(7) Elder, J. P.; Hickling, A. *Transactions of the Faraday Society* **1962**, *58*, 1852-1864.

(8) Morris, J. H.; Gysling, H. J.; Reed, D. *Chemical Reviews* **1985**, *85*, 51-76.

(9) Schlesinger, H. I.; Brown, H. C.; Hoekstra, H. R.; Rapp, L. R. *J. Am. Chem. Soc.* **1953**, *75*, 199-204.

(10) Souza, M. V. N. d.; Vasconcelos, T. R. A. *Appl. Organomet. Chem.* **2006**, *20*, 798-810.

(11) Davis, R. E.; Gottbrath, J. A. *J. Am. Chem. Soc.* **1962**, *84*, 895-898.

(12) Klayman, D. L.; Griffin, T. S. *J. Am. Chem. Soc.* **1973**, *95*, 197-199.

(13) Golden, J. H.; Schreier, C.; Singaram, B.; Williamson, S. M. *Inorg. Chem.* **1992**, *31*, 1533-1535.

(14) Ward, D. E.; Rhee, C. K. *Can. J. Chem.* **1989**, *67*, 1206-1211.

(15) Brown, H. C.; Mead, E. J.; Rao, B. C. S. *J. Am. Chem. Soc.* **1955**, *77*, 6209-6213.

(16) Lalancette, J. M.; Freche, A.; Monteux, R. *Can. J. Chem.* **1968**, *46*, 2754-2757.

(17) Lalancette, J. M.; Arnac, M. *Can. J. Chem.* **1969**, *47*, 3695-3697.

(18) Noth, H.; Mikulaschek, G. *Z. Anorg. Allg. Chem.* **1961**, *311*, 241-248.

(19) Shah, A. R.; Padma, D. K.; Murthy, A. R. V. *Indian J. Chem.* **1971**, *9*, 885.

(20) Hathaway, B. A. *J. Chem. Educ.* **1998**, *75*, 1623-1624.

(21) Banus, M. D.; Bradgon, R. W.; Hinckley, A. A. *J. Am. Chem. Soc.* **1954**, *76*, 3848-3849.

(22) Bard, A. J.; Faulkner, L. R. *Electrochemical Methods*; 2nd ed.; John Wiley & Sons, Inc.: New York, NY, 2001.

(23) Tsushima, M.; Tokuda, K.; Ohsaka, T. *Anal. Chem.* **1994**, *66*, 4551-4556.

(24) Mota, N. D.; Kirtland, J. D.; Finkelstein, D. A.; Rodriguez, C. A.; Stroock, A. D.; Abruña, H. D. *Submitted.* **2010**.

(25) Kumar, T. P.; Prabhu, P. V. S. S.; Srivastava, A. K.; Kumar, U. B.; Ranganathan, R.; Gangadharan, R. *J. Power Sources* **1994**, *50*, 283-294.

(26) Safonova, L. P.; Sakharov, D. V.; Shmukler, L. E.; Kolker, A. M. *Phys. Chem. Chem. Phys.* **2001**, *3*, 819-823.

Chapter 5: Alternative Oxidants for High-Power Fuel Cells Studied by Rotating Disk Electrode (RDE) Voltammetry at Pt, Au, and Glassy Carbon Electrodes

Publication: **2011** *J. Phys. Chem. C.*, *115*, 6073-6084

Personnel: David A. Finkelstein[1], Joseph D. Kirtland[2], Nicolas Da Mota[1], Abraham D. Stroock[2] and Héctor D. Abruña[1].

[1]Department of Chemistry and Chemical Biology, Baker Laboratory,
[2]Department of Chemical and Biomolecular Engineering, Olin Hall
Cornell University, Ithaca, New York 14853

Oxygen (O_2) reduction has long been the factor limiting the power density of most fuel cells. Membraneless, microfluidic fuel cells are a promising new fuel cell technology, yet they are affected even more strongly by O_2, as they usually require a dissolved oxidant, and O_2 has minimal solubility in most solvents. Here we offer a detailed, analytical comparison of the performance of previously employed alternative oxidants, H_2O_2, MnO_4^-, VO_2^+, and ClO^-, at Pt, Au, and glassy carbon (GC) rotating disk electrodes (RDE's). We also investigated cerium ammonium nitrate (CAN), which has an exceptionally high potential for reduction. Of the oxidants studied, CAN offers the best immediate advantage, but MnO_4^-, though requiring development effort, shows the most long-term promise for high-power fuel cells.

5.1 Alternative Oxidants Introduction

Though a great deal of fuel cell research is focused on oxidation of the fuel, the reduction of the oxidant is just as essential for fuel cell operation. While many fuels have been extensively studied and implemented (i.e., H_2, MeOH, EtOH, BH_4^-), O_2 is nearly ubiquitous as the oxidant. The reduction of O_2 at virtually all electrode materials has a high overpotential and relatively slow kinetic reaction rate, causing it (rather than the fuel) to limit power density in nearly every fuel cell today.[1]

The use of O_2 is further complicated in microfluidic fuel cells. These unique systems use laminar flow of fluids, rather than a proton exchange membrane (PEM), to separate the fuel and oxidant streams.[2] This is a highly valuable trait, considering that membranes are often less selectively permeable than designed, can dry out during operation, and represent the major cost of typical fuel cells.[1] However, as laminar fluid flow is required, the oxidant must be dissolved in the catholyte, and O_2 has poor solubility in water (<1.3mM[3]) and other solvents. Gas diffusion electrodes have been employed to combat this problem, resulting in five times greater power density for a laminar-flow, formic acid fuel cell,[4] although generally, such electrodes for O_2 operate poorly, generating water that floods electrode pores.[1] To realize higher power densities in microfluidic fuel cells, oxidants superior to O_2 must be found.

In our study, we examined the previously-employed oxidants O_2, hydrogen peroxide (H_2O_2), permanganate (MnO_4^-), dioxovanadium (VO_2^+), and hypochlorite / bleach (ClO^-), as well as the new fuel cell oxidant CAN ($Ce(NH_4)_2(NO_3)_6$)[5], at Pt, Au, and GC RDE's. Oxidants were studied at low concentration (5mM) to discern analytical parameters, and high concentration (100mM) to examine under conditions more relevant to fuel cell operation. The reductions of most of these compounds have been well-studied, but we aim to provide a useful

comparison by analyzing these compounds in a rigorous and uniform manner under similar experimental conditions. Table 5.1.1 summarizes their expected reduction reactions.

Oxidant	Possible Reactions:	E^0 (V vs. Ag/AgCl)
O_2	$O_2 + 2H^+ + 2e^- \leftrightarrows H_2O_2$	0.498
	$O_2 + 4H^+ + 4e^- \leftrightarrows H_2O$	1.032
H_2O_2	$H_2O_2 + 2H^+ + 2e^- \leftrightarrows 2H_2O$	1.579
MnO_4^-	$MnO_4^- + e^- \leftrightarrows MnO_4^{2-}$	0.361
	$MnO_4^- + 4H^+ + 3e^- \leftrightarrows MnO_2 + 2H_2O$	1.482
	$MnO_4^- + 8H^+ + 5e^- \leftrightarrows Mn^{2+} + 4H_2O$	1.310
$Ce(NH_4)_2(NO_3)_6$	$Ce^{4+} + e^- \leftrightarrows Ce^{3+}$	1.523
VO_2^+	$VO_2^+ + 2H^+ + e^- \leftrightarrows VO^{2+} + H_2O$	0.794
	$VO^{2+} + 2H^+ + e^- \leftrightarrows V^{3+} + H_2O$	0.140
	$V^{3+} + e^- \leftrightarrows V^{2+}$	–0.452
ClO^-	$HClO + H^+ + 2e^- \leftrightarrows Cl^- + H_2O$	1.285
	$HClO + H^+ + e^- \leftrightarrows ½Cl_2 + H_2O$	1.414

Table 5.1.1: Reactions of Oxidants Studied

We have studied $O_{2(aq)}$ to use as a baseline for comparison with the other oxidants. Since its reduction has been extensively studied,[6] we do not seek to contribute any new information in our investigation. The reduction of O_2 may involve 2 or 4 e^- (Table 5.1.1), with the former reaction producing H_2O_2 and the latter H_2O. H_2O_2 can then be further reduced by $2e^-$ to form H_2O. Since O_2 reduction involves H_2O_2 as an intermediate, both O_2 and H_2O_2 reduction should be expected to have similar properties. Both oxidants are typically used with Pt electrodes,[7-10] though Ni electrodes may be used in strong base,[11] and H_2O_2 reduction has been demonstrated at Pd.[12] O_2 and H_2O_2 can also be reduced at Au, as demonstrated in prototype fuel cells,[8,13] but the

reductions occur only at low potentials (large overpotentials) that are not typically useful for fuel cell purposes.[14,15] The reduction of H_2O_2 at Pt is complicated by a catalytic decomposition Reaction involving Reactions 5.1.a and 5.1.b, in which two different H_2O_2 molecules are simultaneously oxidized and reduced, generating O_2 gas and no net current.[16-18] The sum Reaction 5.1.c represents decomposition to H_2O and O_2:

$$H_2O_2 \leftrightarrows O_2 + 2H^+ + 2e^- \quad \textbf{[5.1.a]}$$

$$H_2O_2 + 2H^+ + 2e^- \leftrightarrows 2H_2O \quad \textbf{[5.1.b]}$$

$$2H_2O_2 \leftrightarrows 2H_2O + O_2 \quad \textbf{[5.1.c]}$$

In addition to the deleterious effect on current, this decomposition occurs vigorously, generating O_2 bubbles that not only cover the electrode surface, decreasing its active surface area, but that can also disrupt laminar flow in a microfluidic fuel cell.[12] The decomposition produces an oscillatory current output and has been studied as an interesting electrochemical phenomenon in its own right.[17,18]

MnO_4^- may undergo a multitude of different reduction processes (Table 5.1.1), with $3e^-$ and $5e^-$ reductions occurring at high potential. This superoxidizer has been tested in fuel cells,[19-22] though it typically produces an MnO_2 precipitate on its electrode,[21-26] continually decreasing the effective electrode surface area and therefore the rate of its reaction. The reduction does not appear to require a specific electrode catalyst, and has been observed at Pt,[21-24,27] Ni,[21] and carbon[26,28] electrodes.

VO_2^+ is not currently used as a stand-alone oxidant, but rather is always found as part of a reversible vanadium fuel cell used for charge storage, or "vanadium redox battery." [29,30] These

systems oxidize VO^{2+} (vanadyl ion) to VO_2^+ in one chamber and reduce V^{3+} to V^{2+} in the other (Table 5.1.1). The reactions are then run in reverse to generate power. Though the reactions involve only $1e^-$, reversible vanadium fuel cells have high current recapture efficiency (90%,[30] 99%[31]) and can use carbon anodes and cathodes.[2,30-33]

ClO^- reduction involves either a 1 or $2e^-$ reaction (Table 5.1.1) and has recently been tested in fuel cells.[34-36] We were skeptical about the practical use of this oxidant, as its expected reduction products are Cl_2, a poisonous gas, or Cl^-, one of the strongest noble metal electrode poisons known. However, since it is a highly soluble, high oxidation potential oxidant, we felt it deserved to be considered as well.

The reduction of CAN involves just $1e^-$, but tetravalent cerium compounds are ferocious oxidizers, widely used in organic synthesis,[37] with standard potentials estimated at +1.22 to +1.44 V in H_2SO_4 and up to +1.7 V in $HClO_4$.[38-41] Additionally, previous studies have indicated that Ce's reduction occurs rapidly at Pt,[28,39,41-43] Au,[39,44,45] and GC[28,39,40,44-46] electrodes, suggesting that CAN should serve as a high-voltage, high-performance fuel cell oxidant.

Though several studies used other various important electrode materials, such as Pd, Ni, and various forms of carbon (e.g., graphite, carbon paper, and B-doped diamond), we have limited our investigation to Pt, Au, and GC for scoping purposes. Generally, oxidants that perform well at Pt and GC will also be expected to show activity at Pd and carbon materials, respectively.

Many criteria govern the performance of a given oxidant in a fuel cell. The maximum, or mass-transport-limited, current at the cathode of a microfluidic fuel cell is given by Equation 5.1.1 (see Appendix for a derivation of this expression from the recent literature):[47]

$$i_{l,c} = nFC_O^* D_O WPe\left(1 - \exp\left[-\frac{3}{2}\left(\frac{L}{PeH}\right)^{2/3}\right]\right) \qquad \textbf{[5.1.1]}$$

After mathematical approximation ($e^x \sim 1 + x$ in the Taylor series expansion) and variable substitution for *Pe*, the expression simplifies to Equation 5.1.2:

$$i_{l,c} \sim \frac{3}{2} nFC_O^*\left(\frac{D_O WL}{H}\right)^{2/3} Q^{1/3} \qquad \textbf{[5.1.2]}$$

where $i_{l,c}$ is the mass-transport-limited cathodic current (A), n is the number of e^- transferred, F is Faraday's constant (96,485 C/mol), C_O^* is bulk concentration of the oxidant (mol/cm^3), D_O is the diffusion coefficient (cm^2/s), W, L, and H are channel width, length, and height, respectively (all cm), and Q is the volumetric flow rate (cm^3/s). *Pe* is the Péclet number, a dimensionless ratio of convective to diffusive mass transport, and here is used in the form $Pe = Q/(WD_O)$. Equation 5.1.2 has been derived[48] and discussed[49] previously, but to the authors' knowledge, this expression has not been derived in English within the context of microfluidic, laminar-flow fuel cells.

It is immediately clear that, aside from the fuel cell channel dimensions (W, L, and H) and flow rate (Q), the maximum current obtainable from the oxidant depends heavily on n, C_O^*, and D_O, which are determined by the number of electrons involved in the oxidant's chemical reaction, the maximum solubility of the oxidant, and the nature of the oxidant's interaction with the solvent, respectively. The reason that D_O plays such a large role is that despite the convection of a flowing catholyte, the solution layer contacting the electrode is stagnant, and thus the oxidant's transport still requires diffusion across a short distance (i.e., the Nernst

diffusion layer). It should be noted that i_l's proportionalities with n, C_O^*, and D_O are the same as found in the Levich equation (Equation [2.3.1]), making analytical RDE results highly comparable to an oxidant's performance in an actual microfluidic fuel cell.

Two other parameters are critical in determining the oxidant's voltage performance: the onset potential (E_{onset}) and the kinetic rate of reaction (k_f), which govern the open-circuit voltage of the fuel cell and the rate of current gain from voltage sacrifice, respectively, via the Butler-Volmer expression.[50] All of the above parameters (n, C_O^*, D_O, E_{onset}, and k_f) have been heavily scrutinized in our investigation to provide a very detailed comparison of the various oxidants, and individual parameters often yielded striking differences between them. None of the oxidants were found to be ideal, as each showed either an important weakness in at least one of the given parameters, or exhibited a critically detrimental property (bubbles, precipitation, poisoning, etc.). MnO_4^- and H_2O_2 showed exceptional hypothetical performance, while CAN exhibited a trouble-free, moderately impressive reduction reaction.

5.2 Experimental Methods

All chemicals used were reagent grade, and included oxygen (Airgas), 30% hydrogen peroxide solution (Sigma-Aldrich), cerium ammonium nitrate (Fluka), potassium permanganate (Mallinckrodt), vanadyl sulfate (Sigma-Aldrich), 13.6% sodium hypochlorite solution (Alfa Aesar), 70% nitric acid (EMD), and high-purity (99.999%) sulfuric acid (Sigma-Aldrich). All solutions were prepared with deionized water purified with a Hydro purification system connected in series to a Millipore Milli-Q system (18 MΩ·cm).

The potassium salt of MnO_4^- was used, as it is less hygroscopic than the sodium salt, allowing a precise analytical concentration to be determined. However, practical fuel cells

demand high fuel and oxidant concentrations, so it should be noted that the more soluble sodium salt of this oxidant should be used for fuel cell applications.

A solution saturated with O_2 was prepared by bubbling 0.5 M H_2SO_4 with O_2 gas before each RDE voltammogram at a given rotation rate was taken. O_2 gas was blown over the top of the O_2 solution using a custom glass-capped electrochemical cell during rotation of the RDE. None of the oxidants solutions were deaerated prior or subsequent to addition of the oxidant, as every oxidant studied appeared capable of slowly oxidizing H_2O to O_2, and deaeration would likely have accelerated decomposition of the given oxidant by LeChatlier's principle. Oxidants solutions were freshly prepared (from acid stock solution) immediately prior to investigation and were mixed by gentle inversion to minimize oxidant decomposition. Solutions of $VOSO_4$ and $KMnO_4$ had slow dissolution rates and were mixed by sonication following inversion.

Solutions of VO_2^+ were prepared by bulk electrolysis of VO^{2+}. A large, three-chambered electrochemical cell was used (see description of electrochemical setup below) with high area Pt working and counter electrodes, as well as a Pt pseudoreference. A sufficiently positive potential was applied to the Pt working electrode, and the main cell chamber was stirred with a magnetic Teflon® stir bar and allowed to electrolyze overnight. When the main chamber switched from blue VO^{2+} to yellow VO_2^+, the counter electrode chamber became a darker blue-purple color, and a minimal current was observed at the working electrode, the electrolysis was deemed complete, and the new VO_2^+ solution was immediately used for analysis.

5.3 Results & Discussion

				E_{onset} (V vs. Ag/AgCl)			i_l at 3000rpm (mA/cm^2)	
Compound	n	D_O (x10^{-5} cm^2/s)	max C_O^* (M)	Pt	Au	GC	5mM	100mM
O_2	2.6	2.4[3]	0.001[3]	0.60	-	-	6.2[§]	-
H_2O_2	2	1.5[16]	42.4[‡]	0.64	0.10	-	12.5	220
MnO_4^-	5	1.2[24]	7.3[3]	1.27	1.12	1.11	30.0	590
CAN	1	0.36[44]	2.6[52]	1.47	1.31	1.31	3.0	57
VO_2^+	1	0.25[†]	< 3[59]	0.80	0.88	0.35	2.3	43
ClO^-	-	1.1[73]	10.7[3]	1.20	1.01	1.01	-	>50

Table 5.3.1: Oxidants Performance Parameters Determined or Confirmed by RDE Analysis. †Determined from RDE of VO^{2+} at Pt and Au assuming n = 1. See Results and Discussion for details. ‡Calculated from the density of pure H_2O_2 liquid. §O_2 was studied at its maximum aqueous solubility of ~1.27 mM[3] rather than 5mM.

	α			k_f (cm/s)			k_{eff}^0 (cm/s)		
Compound	Pt	Au	GC	Pt	Au	GC	Pt	Au	GC
O_2	0.56	-	-	0.01	-	-	0.1	-	-
H_2O_2	0.45	-	-	0.02	-	-	0.8	-	-
MnO_4^-	0.58	0.70	0.42	0.03	0.03	0.003	0.6	0.8	0.03
CAN	0.20	0.31	0.26	0.004	0.004	0.003	0.02	0.02	0.07
VO_2^+	0.36	0.80	-	0.002	0.007	-	0.01	0.3	-

Table 5.3.2: Oxidants Kinetic Parameters Determined by RDE Analysis

5.3.1 Oxygen (O_2)

A summary of the analytical results from the various oxidants, including relevant constants from the literature, is shown in Tables 5.3.1 and 5.3.2. All potentials in the text and table are referenced vs. Ag/AgCl.

The RDE results for reduction of O_2 at Pt in an O_2-saturated solution of 0.5 M H_2SO_4 are depicted in Figure 5.3.1.1. Though the E_{onset} and kinetic performance are good, Levich analysis determined that only 2.5e^- were involved in the reduction, indicating a mix between the 2e^- reduction to H_2O_2 and 4e^- reduction to H_2O (Table 5.1.1), with the former reaction dominating the latter. This runs contrary to literature reports of a 4e^- reduction, and the difference is likely due to choice of O_2's diffusion coefficient used in analysis (see below).

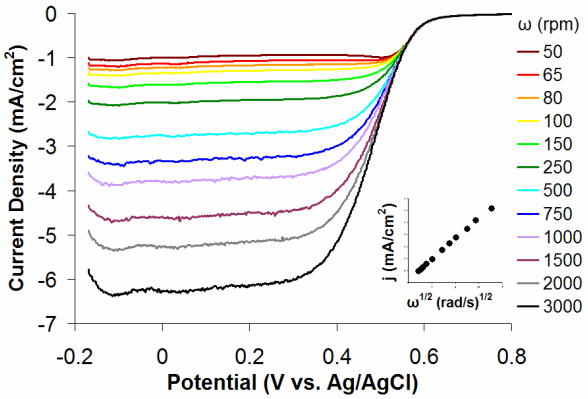

Figure 5.3.1.1: RDE cathodic sweeps of O_2-saturated 0.5 M H_2SO_4 at a Pt disk electrode, 20 mV/s, rotated between 50-3000 rpm. Inset: Levich plot sampled at E = +0.2 V.

It is immediately clear that the low i_l of 6 mA/cm^2 at 3000rpm precludes O_2's use in high-power microfluidic fuel cells. Despite having high values for n, D_O, E_{onset}, and k_f, O_2's low solubility keeps C_O^* to a minimum, in turn limiting i_l and expected cathodic power density.

These results are mostly consistent with those of Marković et al., although they found

slightly higher E_{onset} and i_l values.[6] They determined n to be $4e^-$, and did not observe H_2O_2 production using rotating ring-disk electrode voltammetric techniques. In our own Levich analysis of their data using $D_O = 2.4x10^{-5}$ cm^2/s (Table 5.3.1), their n value appears to be $3e^-$, much like our $2.5e^-$. The discrepancy of their n value as 3 or $4e^-$ is likely attributable to use of a different value of D_O, and their slightly higher i_l is likely due to more effective techniques for keeping O_2 dissolved in acid during convection from rotating their electrode. We defer to their results on favoring the $4e^-$ mechanism. As mentioned in the introduction, we do not attempt to add insight in understanding O_2 reduction. Rather, both our data and that of Marković et al. demonstrate that O_2 provides a low i_l in aqueous fuel cell systems.

5.3.2 Hydrogen Peroxide (H_2O_2)

H_2O_2 represents an intermediate oxidation state of oxygen (–1), and so can be both oxidized to O_2 at high potential and reduced to H_2O at low potential using a Pt electrode, with reactions fairly symmetric about a potential of +0.64 V (Figure 5.3.2.1).[16] Oxidation of H_2O_2 resulted in vigorous O_2 bubble formation at the electrode surface, though reduction of H_2O_2 also produced O_2 bubbles through catalytic decomposition, as described in the Introduction. Bubble formation during H_2O_2 reduction was less rapid, but still significant, and bubbles covered much of the electrode surface before the end of the cathodic sweep in the voltammogram.

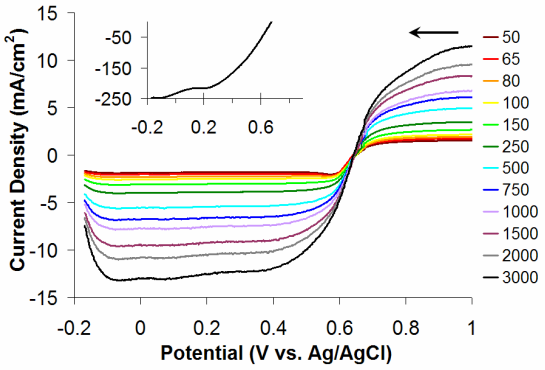

Figure 5.3.2.1: RDE cathodic sweeps of 5mM H_2O_2 in 0.5 M H_2SO_4 at a Pt disk electrode, 20 mV/s, rotated between 50-3000 rpm. Inset: >0.2 A/cm^2 $i_{l,c}$ observed for 100mM H_2O_2 in 0.5 M H_2SO_4 at 3000 rpm.

H_2O_2 showed excellent kinetics and an impressive $i_{l,c}$, allowing it to achieve a current density of 0.2 A/cm^2 for 100mM at 3000rpm (Figure 5.3.2.1, inset). We observed that current densities of this magnitude were so high that normally negligible resistances actually manifested significant voltage drops in the RDE voltammograms for H_2O_2 and MnO_4^-. The resistances appeared as linear current-potential relationships in the normally exponential, kinetically controlled regions of the voltammograms (Figures 5.3.2.1, inset, and 5.3.3.1). Data for H_2O_2 and MnO_4^- are therefore shown at low and high concentrations.

The E_{onset} (+0.64 V, Figure 5.3.2.1) for H_2O_2 reduction began soon after Pt surface oxide reduction began (+0.75 V), indicating that H_2O_2 has no reduction activity on a complete Pt oxide layer, in line with results from other workers,[14,16] but also that it does have some activity on a partially oxidized Pt surface. Regions of higher Pt oxide coverage support H_2O_2 oxidation. Our results support Prabhu et al.'s observation that reduction of H_2O_2 at Pt begins slightly before the reduction of O_2 (+0.60 V).[16] Our estimated α and k^0_{eff} of 0.45 and 0.8 cm/s (Table 5.3.2), respectively, were close to the 0.3 and 0.3 cm/s obtained by Prabhu et al., although our value of

k^0_{eff} is unphysically high. It is clear, however, that the reaction proceeds very quickly at minimal overpotentials following E_{onset}.

Though the reduction has an n of just $2e^-$ (Table 5.1.1), high current is nonetheless effected, largely owing to a superior D_O of $1.5x10^{-5}$ cm^2/s (Table 5.3.1), as observed previously.[14,16] Prabhu et al. concluded that the current observed from H_2O_2 reduction at Pt is from reduction of O_2 generated by catalytic decomposition,[16] but in our view, this is physically unlikely, as the currents observed in Figure 5.3.2.1 are more than 40x higher than can be generated by an O_2-saturated solution (Figure 5.3.1.1). Thus, H_2O_2 undergoes direct reduction at Pt. Prabhu et al. speculated that the boost in current at potentials below 0.2 V (Figure 5.3.2.1, inset) was due to reduction of O_2 generated by catalytic decomposition of H_2O_2,[16] although this also seems very unlikely, as our data show an increase in current of 32 mA/cm^2 between +0.1 and –0.1 V at 3000rpm, while the i_l of an O_2-saturated solution at 3000rpm is less than 6.5 mA/cm^2 (Figure 5.3.1.1). Perhaps O_2 generated at the surface blocks sites for H_2O_2 reduction, and this O_2 is reduced off the surface at lower potentials. Though other explanations are certainly possible, it is important to understand this phenomenon, as it seems to limit i_l at small overpotentials (higher potentials), decreasing the expected power from H_2O_2.

H_2O_2 also shows activity at Au (Figure 5.3.2.2), but only at potentials of +0.1V or below, which are impractical for high-power fuel cell development. Using surface-enhanced Raman spectroscopy, Li et al. found that, unlike Pt, Au does not stretch adsorbed H_2O_2's O-O bond enough to break it.[14] These results were consistent with a density functional theory approach, which showed poor interaction between Au and the O-O bond of superoxide.[15] Thus, H_2O_2's low activity at Au represents a fundamental catalytic constraint, so the reaction was not studied further.

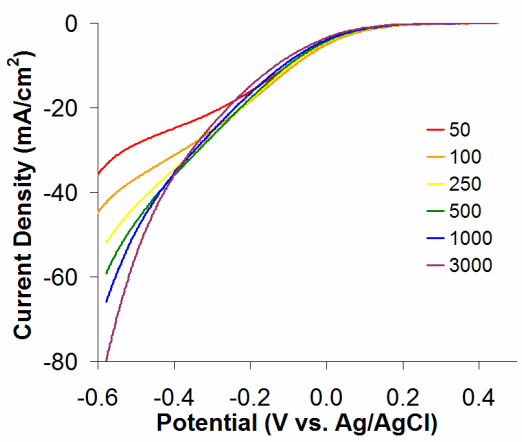

Figure 5.3.2.2: RDE cathodic sweeps of 5mM H_2O_2 in 0.5 M H_2SO_4 at an Au disk electrode, 20 mV/s, rotated between 50-3000 rpm. Inset: >0.2 A/cm^2 $i_{l,c}$ observed for 100mM H_2O_2 in 0.5 M H_2SO_4 at 3000 rpm.

With an impressive i_l (owing to high D_O and $n > 1$), E_{onset}, and kinetic performance, H_2O_2 serves as a potent oxidant. It is also a liquid with very high solubility in H_2O, and is 42 M in its pure form (Table 5.3.1). However, its tendency to generate gas bubbles at Pt at high concentration limits its practical use. Either alternative catalysts, which only catalyze H_2O_2 reduction, rather than its decomposition, must be found, or engineering advances, such as grooved, bubble-collecting cathodes developed by Kjeang et al.,[12] must be developed for effective utilization of H_2O_2.

5.3.3 Permanganate (MnO_4^-)

MnO_4^- was easily the highest-performing oxidizer analyzed in this study, able to deliver >0.5 A/cm^2 at high potential at a concentration of just 0.1 M (Figure 5.3.3.1). This powerful redox reaction does not require a precious metal catalyst, showing significant performance at GC, although the E_{onset} and kinetic rate of reaction were higher and faster at Au and especially Pt

(Figures 5.3.3.1 and 5.3.3.2). The superiority of Pt over Au was mostly evident at 100mM (Figure 5.3.3.1), while at 5mM, Pt has a higher E_{onset} but slightly less steep RDE voltammogram (Figure 5.3.3.2). Since *k* values were determined at 5mM, there is little differentiation among the average *k* values for Pt and Au presented in Table 5.3.2.

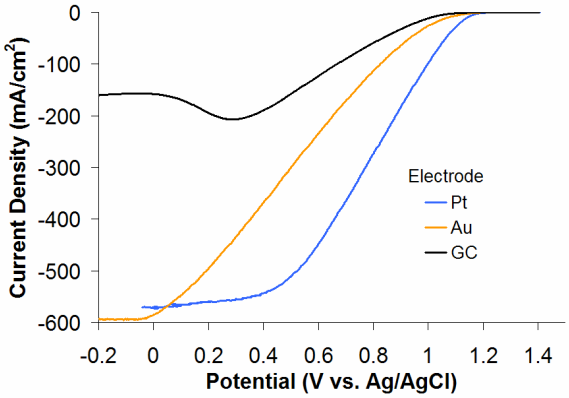

Figure 5.3.3.1: RDE cathodic sweeps of 100mM MnO_4^- in 0.5 M H_2SO_4 at Pt, Au, and GC disk electrodes, 20 mV/s, rotated at 3000 rpm. The high $i_{l,c}$'s cause small resistances to manifest linear, resistive regions in the current-potential relationship.

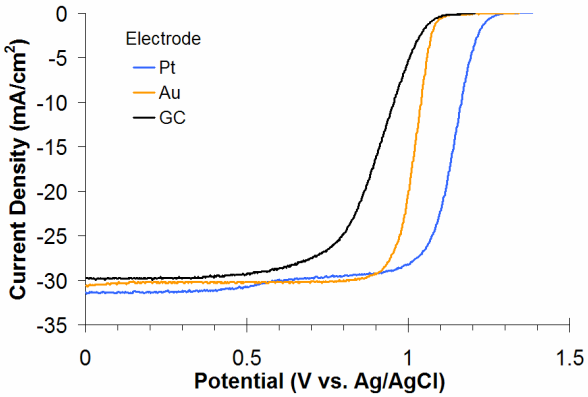

Figure 5.3.3.2: RDE cathodic sweeps of 5mM MnO_4^- in 0.5 M H_2SO_4 at Pt, Au, and GC disk electrodes, 20 mV/s, rotated at 3000 rpm.

Unfortunately, a film of brown, MnO_2 precipitate[23] appeared at the Teflon® edges of the RDE's at even 5mM, and at 100mM, the electrode surfaces were partially blocked by precipitate after just one potential sweep. The RDE voltammograms for 100mM MnO_4^- in Figure 5.3.3.1 represent the first cathodic sweeps only, and i_l dropped sharply on consecutive sweeps. Visual inspection showed a thick layer of MnO_2 covering the electrode surface. The precipitate formed at all three electrode materials studied, in contrast with a previous report indicating that the precipitate did not appear at GC.[26] In fact, precipitation occurred so quickly at GC that the electrode surface became significantly blocked on the time scale of its RDE voltammogram, and the expected i_l of ~600 mA/cm^2 could not be manifested (Figure 5.3.3.1).

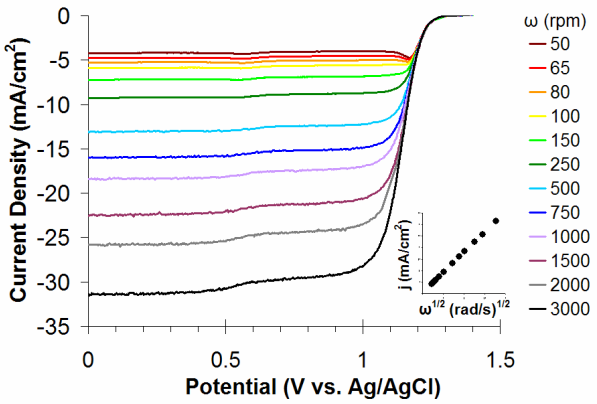

Figure 5.3.3.3: RDE cathodic sweeps of 5mM MnO_4^- in 0.5 M H_2SO_4 at a Pt disk electrode, 20 mV/s, rotated between 50-3000 rpm. Inset: Levich plot sampled at E = +0.1 V.

Although the precipitate did form at the electrode surface, MnO_2 does not represent an electrochemical byproduct of MnO_4^- reduction. At 5mM MnO_4^-, MnO_2 precipitate formation is so much slower that it does not readily cover the electrode surface nor inhibit MnO_4^- reduction, allowing repeated RDE voltammograms with a perfectly linear Levich plot at +0.1 V (Figure

5.3.3.3). The precipitation reaction 5.3.a is most likely oxidation of MnO_4^-'s $5e^-$ reduction product, Mn^{2+} (Table 5.1.1), with excess MnO_4^-:[22,51]

$$2MnO_4^- + 3Mn^{2+} + 2H_2O \rightarrow 5MnO_2 + 4H^+ \qquad \textbf{[5.3.3.a]}$$

The precipitation problem scales directly with the concentration of MnO_4^- used, as this will accelerate the homogenous precipitation reaction, explaining why trials at 100mM decreased active electrode surface area much faster than those at 5mM. Thus, precipitation is not integral to MnO_4^- reduction, but it is very likely to occur at the elevated oxidant concentrations necessary for high-power fuel cells.

The extraordinary i_l >0.5 A/cm^2 (Figure 5.3.3.1) achieved with MnO_4^- owes to the high n of $5e^-$ and D_O of $1.2x10^{-5}$ cm^2/s (Table 5.3.1). Much lower values for D_O have been reported ($7x10^{-6}$ [26] and $8.4x10^{-6}$ cm^2/s[27]), but with the data presented, they would require MnO_4^- to accept about $7e^-$, which would have plated Mn^0 on the electrode, and this was not visually evident at either Au or GC. Also, it is doubtful that Mn would have the same catalytic properties as Pt or Au, and the proportionately congruent RDE voltammograms at 5mM (Figure 5.3.3.3) would not have been obtained. Using the tabled value of $1.63x10^{-5}$ cm^2/s, based on the conductivity of MnO_4^- salt solutions,[3] our analysis would indicate about $4e^-$ involved, which would be an even mix between the $3e^-$ and $5e^-$ reductions (Table 5.1.1), the former of which produces MnO_2 precipitate. We view this as unlikely, since repeated potential sweeps at 5mM did not coat the electrode surface with MnO_2, as described earlier. Schurig and Heusler's D_O of $1.2x10^{-5}$ cm^2/s[24] made an excellent fit to our data to describe $n = 5e^-$ for MnO_4^- reduction, and this value of n has been observed previously in sulfuric acid solutions of MnO_4^-.[22]

We note that in base, MnO_4^- has been observed to undergo two sequential, $1e^-$ reductions to MnO_4^{2-} and MnO_4^{3-}, both of which may further react to form MnO_2.[21,23,24] The species MnO_4^-, MnO_4^{2-}, and MnO_4^{3-} are purple, green, and blue, respectively.[27] As we did not observe a color change in dilute 5mM solution, and our RDE voltammograms showed a single, mass-transport limited wave, we conclude that MnO_4^-'s reduction involves $5e^-$ in acid solution.

The kinetics of MnO_4^-'s reduction are as exceptional as its i_l. Past studies have determined k^0 to be $1.5x10^{-2}$ [28] and 2 to 5 $x10^{-2}$ cm/s at carbon electrodes, $8x10^{-3}$ cm/s at Au, and $2x10^{-2}$ to 0.8 cm/s at Pt, with α ranging from 0.5 to 0.8, depending on the method of analysis.[26] While our values of k^0_{eff} are unphysically high at Pt and Au, our k_f values are reliable and still indicate a rapid reaction (Table 5.3.2). The various k values and RDE voltammograms (Figures 5.3.3.1 and 5.3.3.2) also indicate that while MnO_4^- at GC is clearly slower than at Pt or Au, the reaction is still comparatively fast relative to other redox chemistries, and GC may be used as a cathode when fuel cell material cost is of utmost priority.

MnO_4^- manifests high kinetics, E_{onset}, and i_l, but its practical use is precluded by precipitate formation, as mentioned previously. Since precipitation is not an unavoidable aspect of MnO_4^- reduction, new, secondary chemical reactions, which interfere with precipitate formation or accumulation, must be introduced for MnO_4^- to be used at concentrations practical to high power fuel cell development.

5.3.4 Cerium Ammonium Nitrate ($Ce(NH_4)_2(NO_3)_6$)

CAN's reputation as a strong oxidant was upheld in our study, manifesting the highest E_{onset} of any of the oxidants studied herein (Table 5.3.1, Figure 5.3.4.1), exceeding the roughly +1.23 V at Pt for $Ce(SO_4)_2$ observed previously[41] by nearly 0.25 V. Fast kinetics were also

evident, as CAN also achieved its i_l at Au at 100mM and 3000rpm by 1 V, which is 0.4 V higher than any oxidant, save ClO^-. Perhaps most importantly, CAN did not exhibit any adverse side reactions, such as the bubbles, precipitation, or poisoning observed with H_2O_2, MnO_4^-, or ClO^-.

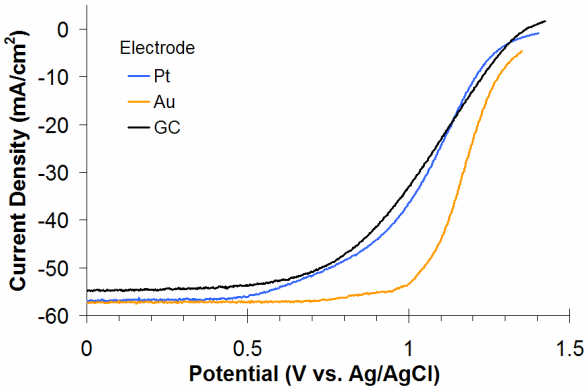

Figure 5.3.4.1: RDE cathodic sweeps of 100mM CAN in 1 M HNO_3 at Pt, Au, and GC disk electrodes, 20 mV/s, rotated at 3000 rpm.

CAN's main drawback is clearly its low i_l. The $1e^-$ reduction process does not utilize the multiplier effect of n in Equation 5.1.2. CAN's D_O (Table 5.3.1) is about 3x smaller than most of the other oxidants studied, and is diminutive compared to most other soluble molecules in general.[3] Furthermore, CAN's limited solubility of 2.6 M[52] combined with n = 1 equates to a maximum of 2.6 M electron equivalents (e^-'s), whereas MnO_4^-'s solubility of 7.3 M and n = 5 could provide 37 M electron equivalents. CAN's low solubility and high molecular weight create significant drawbacks in terms of volumetric and gravimetric energy densities, respectively, both of which are critical for portable fuel cell applications.

CAN performed well at all of the electrodes studied, although it has slightly better kinetics at Au (Figure 5.3.4.1). These findings support the conclusions of Kiekens et al. that

tetravalent Ce has limited, if any, adsorption at Au, Ir, and GC, and that CAN kinetics are independent of electrode material.[44] Previous results indicating inhibition of CAN reduction at Pt oxide[43] are not supported, since CAN showed high activity in the Pt oxide region (positive of +0.7 V).

The D_O calculated from our results was in line with the lower values of D_O found previously of 3.4[53] and 3.6x10^{-6} cm^2/s,[44] and half the value of other reports at 6.2[40] and 5x10^{-6} cm^2/s.[41] Tetravalent Ce is a well-studied oxidant, with determined k^0's of 1x10^{-4},[41] 3.7x10^{-4},[28] and 4.8x10^{-4}cm/s[54] at Pt; 2x10^{-4},[44] 3x10^{-4},[39] and 3-8x10^{-5} cm/s at Au[45]; 5.3x10^{-5},[46] 3x10^{-4},[44] and 3x10^{-2} cm/s[40] at GC; 3.8x10^{-4} cm/s at carbon paste;[28] and 5x10^{-6} to 1.5x10^{-5} cm/s at boron-doped diamond.[45] A k_f at Pt of 3x10^{-4} cm/s was also recorded. [43] Our k^0_{eff}'s were much higher than these literature values, most likely because very few of these studies used RDE to determine kinetic information,[41,44,53] and of those that did, our use of E_{onset} instead of thermodynamic E^0 in the K-L equation (Equations [2.3.2] and [2.3.3]) may have comparatively inflated k^0_{eff}. Our low values of α (about 0.2 to 0.3, Table 5.3.2) do not require knowledge of E^0, and were more in line with literature reports of 0.12,[41] 0.15,[43] 0.21,[28] 0.22,[42] 0.31,[55] and ~0.4[56] at Pt; 0.33[44] and 0.35[39] at Au; 0.16[46] and 0.25[44] at GC; and 0.28[28] at carbon paste. Though Paulenova et al. found $Ce(SO_4)_2$ to have 0.6 M solubility in 1N H_2SO_4,[57] Kaye and Laby report that CAN's solubility is much higher, at 2.6 M,[52] and this latter value was much more in agreement with what we observed experimentally (~2.5 M in 1M HNO_3).

CAN's usage is strictly limited to acidic environments, as it quickly precipitates to $Ce(OH)_4$, and possibly other hydroxide compounds, in base via hydrolysis reactions.[40,41,58] While CAN is shelf-stable as a solid, solutions of CAN slowly degrade, since CAN's E^0 is so high that it will oxidize H_2O to O_2.[43]

Showing no poisoning, high E_{onset}, and excellent kinetics, CAN is a reliable and powerful oxidant. Its low solubility, n, and D_O, however, represent fundamental physical restraints on its practicality for high-power and portable fuel cells.

5.3.5 Dioxovanadium (VO_2^+)

VO_2^+ was the lowest-performing alternative oxidant examined in our study, with the smallest observed i_l and an E_{onset} about 0.4-0.6 V lower than CAN, MnO_4^-, or ClO^- (Table 5.3.1, Figure 5.3.5.1). Though VO_2^+'s E_{onset} was about 0.2 V higher than H_2O_2, its i_l was less than five times lower. The problem with VO_2^+'s low i_l is compounded by its low solubility of <3M, and that its reduction product, VO^{2+} (Table 5.1.1), is less soluble at higher $[H_2SO_4]$,[59] which would otherwise raise VO_2^+'s E_{onset} via the Nernst equation.[50] Solubility is such a serious problem that commercial and high-performance vanadium redox batteries require stabilizing chelators, such as hexametaphosphate, EDTA, phosphoric acid, acetyl acetone, and other compounds.[33,60-62] Furthermore, VO_2^+ precipitates at high temperatures,[32] which would otherwise enhance its kinetic rate of reduction.[50] The principal advantage of using VO_2^+ is limited to its employment in vanadium redox batteries. In this case, both the fuel and oxidant are based on highly reversible V electrochemistry, so the spent fuel and oxidant do not require separation, and fresh solutions can be regenerated from equal portions of the same exhaust solution.[31]

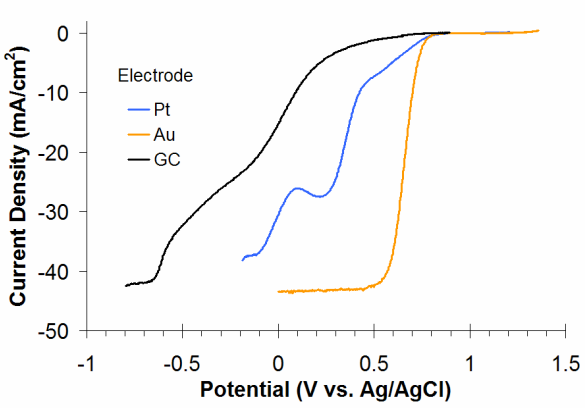

Figure 5.3.5.1: RDE cathodic sweeps of 100mM VO_2^+ in 0.5 M H_2SO_4 at Pt, Au, and GC disk electrodes, 20 mV/s, rotated at 3000 rpm.

The low i_l for VO_2^+ stems not only from a $1e^-$ reduction (Table 5.1.1), but also from VO_2^+'s conspicuously low D_O of $2.5x10^{-6}$ cm^2/s, which is even lower than CAN's (Table 5.3.1), despite V being a first-row transition metal and Ce being a Lanthanide series metal with six nitrate ligands. We were concerned that since we had prepared the VO_2^+ solution by bulk electrolysis of VO^{2+} (see Methods), perhaps the concentration of VO_2^+ was unexpectedly smaller than the VO^{2+} starting compound, and we may have mistaken the decrease in C_O^* for a decrease in D_O when using the Levich equation (Equation [2.3.1]). Starting with 5mM VO^{2+} solution prepared from dissolution of $VOSO_4$, and therefore a known bulk concentration, we performed RDE of VO^{2+} reduction at Pt (Figure 5.3.5.2) and VO^{2+} oxidation at Au (Figure 5.3.5.3), both of which are well-behaved redox reactions. The perfectly linear Levich plots obtained also correspond to a D_O of $2.5x10^{-6}$ cm^2/s when assuming $n = 1$, in reasonable agreement with previous findings.[63] Thus, the low D_O is not an artifact from bulk electrolysis, and represents an important limit to VO_2^+'s performance in fuel cells. Notably, our value for D_O is actually in

reasonable agreement with previous studies,* which found D_O to be 3-3.5x10^{-6} cm^2/s,[64-66] with older studies at a dropping Hg electrode finding a somewhat higher D_O of about 6x10^{-6} cm^2/s.[67,68]

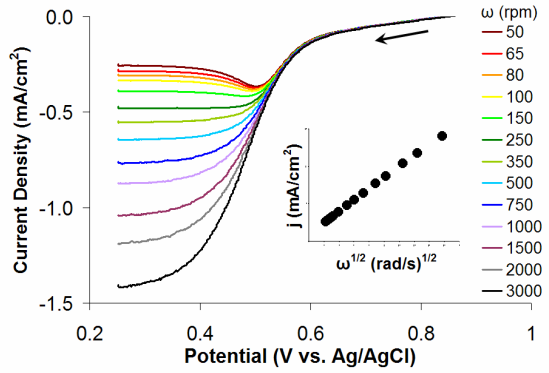

Figure 5.3.5.2: RDE cathodic sweeps of 5mM VO^{2+} in 0.5 M H_2SO_4 at a Pt disk electrode, 20 mV/s, rotated between 50-3000 rpm. Inset: Levich plot sampled at E = +0.25 V.

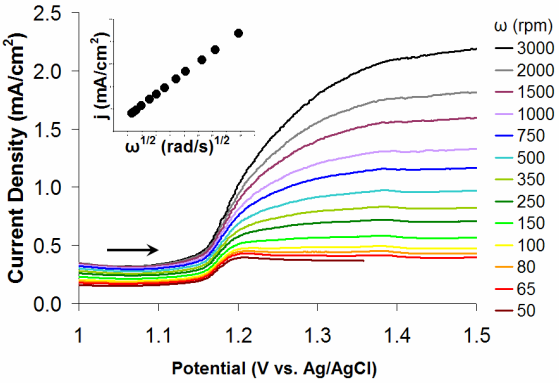

Figure 5.3.5.3: RDE anodic sweeps of 5mM VO^{2+} in 0.5 M H_2SO_4 at an Au disk electrode, 20 mV/s, rotated between 50-3000 rpm. Inset: Levich plot sampled at E = +1.45 V.

* These values for D_O come from our own analysis of the data presented in the cited papers and twice disagrees with the values for D_O presented by the original authors.

The reason for VO_2^+'s unusually low D_O most likely stems from its strong, attractive interaction with solvent and electrolyte species, which exert a drag on the molecule as it diffuses through solution. It has been observed that when VO^{2+} has been complexed to various anions, its diffusion coefficient decreases.[68] VO^{2+} appears to have a tendency to form complexes in solution with SO_4^{2-}, since its solubility decreases markedly at higher $[H_2SO_4]$,[59,68] and the effect of $[HSO_4^-]$ and $[SO_4^-]$ on Tafel plots of VO^{2+} is beyond that expected for the pH change.[65] In fact, VO^{2+} will form the solvated complexes $VOSO_4$, $VO(SO_4)_2^{2-}$, and $VOHSO_4^+$ in H_2SO_4,[69] and various V oxyions can even complex with one another.[70] Though VO_2^+'s D_O is almost unphysically low, it is consistent with VO_2^+'s behavior in H_2SO_4 and other solutions.

Vanadium redox batteries described to date universally use carbon-based cathodes,[2,29-33,60] which we found surprising considering VO_2^+'s tremendously superior performance (higher E_{onset} and k_f, Tables 5.3.1 and 5.3.2) at Au and Pt than at GC (Figure 5.3.5.1). Since VO_2^+'s reduction at GC was so slow and complicated (that is, exhibiting an intricate waveform), we did not feel confident in calculating a value for either k_f or k_{eff}^0, and we were also unable to establish a reasonably linear Levich plot until potentials of –0.5 V for 5mM VO_2^+ and –0.6V for 100mM VO_2^+. Multiple groups have noted that vanadium redox batteries have very limited power density and voltage,[33,65] limiting commercial applications to stationary power supplies that can accommodate the high volume of V solutions required to hold any significant energy.[32]

Our results suggest that employing an alternative cathode material may considerably improve the performance of such devices. VO_2^+'s reduction has been tested at Pt[42,71] and Au[64] previously, although using either of these catalysts is not straightforward. Although Pt has improved voltage and kinetics compared to GC, its waveform is just as complicated as GC's, possibly showing multiple reductions of VO_2^+ to VO^{2+} and V^{3+} (Figure 5.3.5.4), or perhaps even

an adsorptive process (i.e., a peak in the wave) that changes the activity of Pt midway through its reduction wave (Figure 5.3.5.1). It is notable that while Pt can perform two separate reductions of VO_2^+ (Figure 5.3.5.4), Au was observed to perform only a single reduction to VO^{2+}.

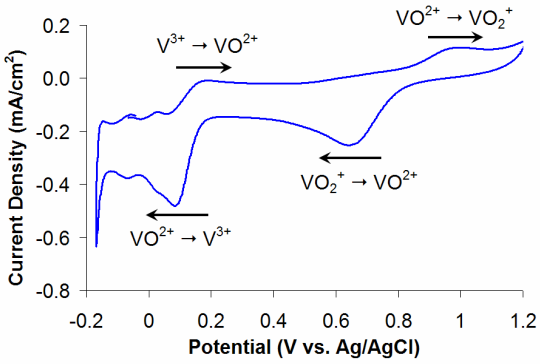

Figure 5.3.5.4: Stationary cyclic voltammogram of 5mM VO_2^+ in 0.1 M H_2SO_4 at a Pt disk electrode, 20 mV/s.

The reduction of VO_2^+ at Au shows some degree of an EC reaction (electrochemical reduction followed by a chemical transformation), in line with speculation by Huang et al. on transfer of O atoms after VO_2^+'s reduction (Figure 5.3.5.5).[33] The EC reaction is evident in the rotation-rate normalized RDE voltammograms of 5mM VO_2^+ at Au, in which scaling of the voltammograms is eliminated, and changes in the size or shape of the waves often indicate coupled-chemistry reactions. If an EC mechanism exists, then at lower rotation rates, VO_2^+'s reduction product has more time to undergo its chemical transformation near the electrode surface, removing the reduced species from solution, and shifting E^0 more positive according to the Nernst equation.[50] This trend is somewhat apparent in Figure 5.3.5.5.

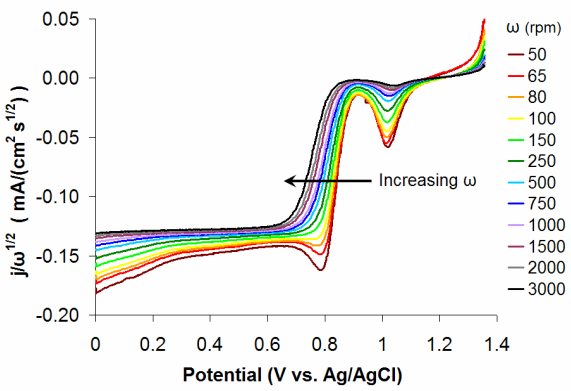

Figure 5.3.5.5: RDE cathodic sweeps with current density (j) normalized by the square root of the rotation rate ($\omega^{1/2}$). Experimental conditions: 5mM VO_2^+ in 0.5 M H_2SO_4 at an Au disk electrode, 20 mV/s, rotated between 50-3000 rpm.

Previously, Sum et al. also observed much higher performance of VO_2^+ at Au via RDE investigation, but concluded that Au was a poor catalyst, since its performance degraded over time.[64] Our RDE voltammograms did not show any poisoning whatsoever (Figure 5.3.5.1), but upon holding the potential in the mass-transport limited region of 100mM VO_2^+ at 3000rpm (+0.3 V, Figure 5.3.5.6), we found that Au's activity for VO_2^+ reduction decreased by 40% in under 15 min, and gradually approached a more stable 50% reduction at longer times. This seemed contradictory with our RDE results, but upon sweeping a 40% poisoned electrode to higher potentials, an oxidative peak appeared (Figure 5.3.5.7), and subsequent sweeps or potential holds at low potential showed the originally observed activity for VO_2^+ reduction. Thus, VO_2^+ reduction at Au appears to result in adsorption of a V species which significantly decreases Au's activity, but the adsorbed species can be oxidatively removed at higher potentials to restore activity. These findings could be of critical significance to vanadium redox battery systems, indicating that Au cathodes could (1) decrease energetic losses due to slow kinetics for rapid charging and discharging with carbon cathodes and (2) provide a much higher system

power density, but (3) would require a cyclical voltage during discharge to push the potential of the cathode high enough (toward open-circuit voltage) to remove activity-decreasing V species adsorbed on the electrode.

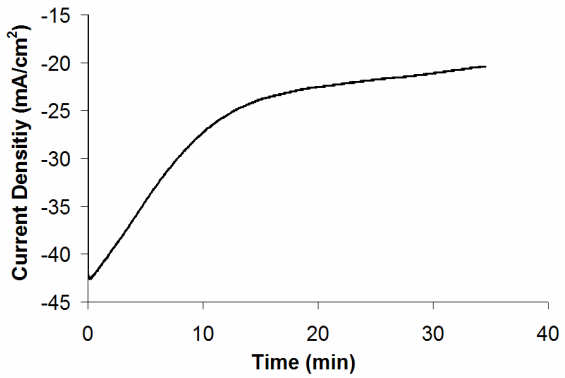

Figure 5.3.5.6: Continuous current generated by a potential step applied from +1.01 V to +0.3 V for 100mM VO_2^+ in 0.5 M H_2SO_4 at an Au disk electrode, rotated at 3000rpm. Fast poisoning is evidenced by the sharp drop in cathodic current.

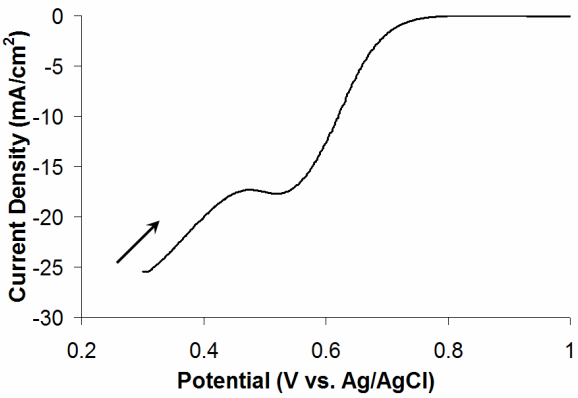

Figure 5.3.5.7: RDE anodic sweep of 100mM VO_2^+ in 0.5 M H_2SO_4 at a heavily poisoned Au disk electrode, 20 mV/s, rotated at 3000 rpm. The peak in the anodic sweep likely represents oxidative removal of an adsorbed species.

VO_2^+ is a comparatively weak oxidant, but has high utility in situations where facile, reversible oxidant recharge is mandatory. As was the case with CAN, its low solubility, *n*, and especially minuscule D_O strongly limit its current output, but unlike CAN, its E_{onset} is moderate, on par with H_2O_2 rather than MnO_4^-. These characteristics give VO_2^+ the smallest expected power density of any of the oxidants studied. Though VO_2^+ is most frequently used with carbon cathodes, it has poor activity at this material, indicating that vanadium redox batteries using carbon cathodes will suffer tremendous loss of power upon charging and discharging. Employing Au cathodes will dramatically improve the expected power recovery from vanadium redox batteries, but VO_2^+'s reversible poisoning at Au requires a complex voltage waveform to ensure minimal efficiency loss.

5.3.6 Hypochlorite (ClO^-)

ClO^- was very disappointing, as it poisoned Pt, Au, and even GC during reduction. The RDE voltammograms depicted in Figure 5.3.6.1 represent the first scan only under the given experimental conditions (100mM ClO^- at 3000rpm), and on just the first scan, it is clear that a mass-transport limited plateau does not establish; rather, the poisoning is so rapid that the current decreases linearly with time. RDE analytical information was impossible to obtain, as poisoning was evident even on the first sweep for the lowest i_l case scenario of 5mM ClO^- at 50rpm. The poisoning was extremely strong, with later scans at 3000rpm producing an i_l roughly equal to that obtained on the first sweep at 50rpm. Since ClO^- poisons the electrodes Pt, Au, and GC so quickly, and decreases expected current so significantly, it is not a candidate for future microfluidic fuel cell devices.

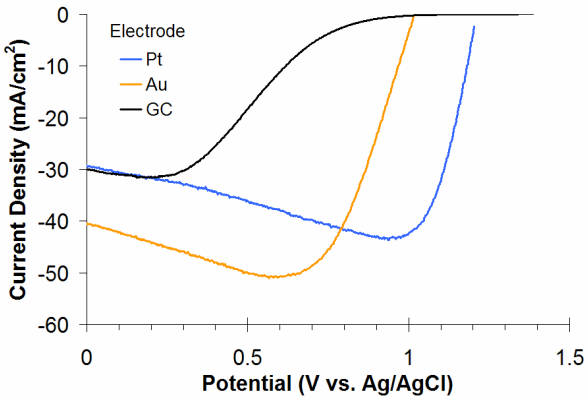

Figure 5.3.6.1: RDE cathodic sweeps of 100mM ClO^- in 0.5 M H_2SO_4 at Pt, Au, and GC disk electrodes, 20 mV/s, rotated at 3000 rpm.

It is neither clear nor certain how studies that used ClO^- as an oxidant in electrochemical devices could have demonstrated steady power production using such a poison-prone oxidant, though there are several possible reasons why poisoning may have gone unnoticed. Kjeang et al. electrodeposited a Pd catalyst on porous carbon (with an Au adhesion layer) using a large catalyst loading, creating a very high surface area cathode.[36] It is possible that complete poisoning of the catalyst may not have occurred during the time course of the experiments. Medeiros and Dow used seawater salts as their electrolytes,[34] and may have pre-poisoned their cathode with Cl^- before operation. If this were the case, current would have started out low, but would not have decreased further, because a stable layer of PdCl may have already formed. Although we did not examine Pd in our study, we assume that it would poison from Cl^- as readily as Pt did. Cardenas-Valencia et al.'s ClO^- battery system had a limited lifespan, but it is difficult to tell whether this was governed by the consumption of anode and cathode materials as opposed to poisoning at the cathode.[35] Analytical studies of ClO^- reduction and oxidation at Pt

used NaCl as an electrolyte,[72,73] and, similar to Medeiros and Dow, may have pre-poisoned their electrodes with Cl^- (to make a stable layer of PtCl) before any ClO^- redox processes began.

Aside from the intense deactivation processes, ClO^- is a fair fuel cell oxidant. Its reduction at Pt begins at the very high potential of +1.2 V, slightly lower than CAN and on par with MnO_4^-. Its D_O is impossible to determine, but is roughly the same as CAN, as the values of i_l for the two oxidants are similar. Once its cathode catalyst is poisoned with Cl^-, though, the i_l drops precipitously, diminishing ClO^-'s role as a potential high-power oxidant.

5.4 Conclusions

A meta-analyses of the various oxidants studied provides important trends for understanding the performance of a given oxidant in a high-power, microfluidic fuel cell. A comparison of all of the oxidants at their best catalysts, at 100 mM and rotated at 3000rpm, is presented in Figure 5.3.4.1. Because of the linear, resistive current-potential distortions at high current densities, the same results for 5mM solutions are presented in Figure 5.3.4.2. Some of these trends may not hold outside the concentration range investigated, but they did apply quite well for the 20 times increase in concentration used herein. It is immediately clear that any oxidant which undergoes only a $1e^-$ reduction (i.e., CAN, ClO^-, and VO_2^+) will have a comparatively small i_l, and as such will have limited use for portable fuel cell applications. An oxidant's reduction must have a minimum n of $2e^-$ to generate significant current with either a small volume or weight of oxidant.

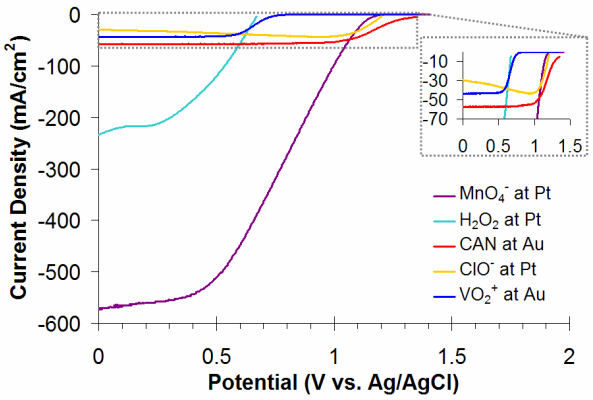

Figure 5.3.4.1: RDE cathodic sweeps of 100mM of various oxidants in 1 N acid (HNO_3 for CAN, H_2SO_4 for all others), 20 mV/s, rotated at 3000 rpm. Each oxidant is shown at its highest-performing catalyst, indicated in the legend. H_2O_2 and MnO_4^- show linear regions in their current-potential relationships due to resistance at high current density. Inset: Same data magnified to show a comparison of the lower-current oxidants.

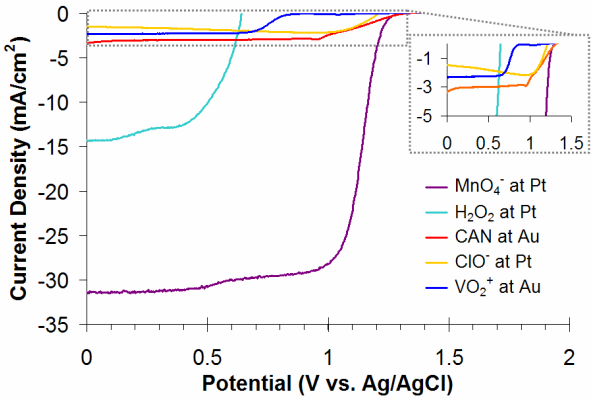

Figure 5.3.4.2: RDE cathodic sweeps of 5mM of various oxidants in 1 N acid (HNO_3 for CAN, H_2SO_4 for all others), 20 mV/s, rotated at 3000 rpm. Each oxidant is shown at its highest-performing catalyst, indicated in the inset legend. Inset: Same data magnified to show a comparison of the lower-current oxidants.

It is also apparent that, as predicted by Equations [5.1.2] and the Levich equation (Equation [2.3.1]), the D_O and max solubility (max C_O^*) for an oxidant are just as important as n. Though H_2O_2 has double the n of CAN, ClO^-, and VO_2^+, its i_l is about four times greater because its D_O is over four times CAN's and six times VO_2^+'s. The max C_O^* is critical for scaling the performance of the oxidants under ideal circumstances. At 2.6 M, CAN's best theoretical i_l would be around 1.5 A/cm^2, whereas MnO_4^-'s would be over 40 A/cm^2 at 7.3 M (Table 5.3.1). At such high concentrations, undesirable effects, such as substantial viscosity, precipitation, or side reactions, may prevent these currents from being fully realized. However, if just 10% of MnO_4^-'s possible current were realized, it would provide about 2.5 times the maximum current obtainable from CAN.

The oxidants also showed important disparities in E_{onset}. CAN, MnO_4^-, and ClO^- begin their reductions positive of +1.2 V, while H_2O_2 and VO_2^+ do not begin their reactions until potentials 0.5 V lower (Table 5.3.1). Since a fuel cell's open-circuit voltage is the difference between E_{onset} values for a low-potential anode and a high-potential cathode, fuel cells using CAN, MnO_4^-, and ClO^- will have an open-circuit voltage 0.5 V higher than the other oxidants.

Most of the oxidants showed similar values for k_f (Table 5.3.2), but the real difference in kinetic performance appeared when using different cathode catalysts for the same oxidant. Though every alternative oxidant save H_2O_2 could be reduced at GC, which is very attractive in terms of minimizing materials costs, the oxidants universally showed poorer kinetic performance at GC, costing over 0.5 V to fuel cell systems using MnO_4^-, VO_2^+, and ClO^-. CAN, as the lone exception, lost only around 0.2 to 0.3 V at GC compared to its best catalyst (Figure 5.3.4.1).

Though sensible in hindsight, the oxidants did not show a global preference for Pt over Au or vice versa. For some oxidants, such as CAN and VO_2^+, the less interactive Au electrode

exhibited better kinetic behavior, perhaps (especially in the case of VO_2^+) because adsorptive processes at Pt may have complicated the reaction mechanism. In contrast, MnO_4^-, H_2O_2, and ClO^- all performed significantly better at Pt than Au, likely requiring specific catalysis with less noble Pt.

Overall, MnO_4^- is the most promising oxidant studied, with the highest i_l by an order of magnitude, excluding H_2O_2, and the second-highest E_{onset}. Both MnO_4^- and H_2O_2 show great capability for high power density and high energy density fuel cell systems, but unfortunately, the former is plagued by an inactivating precipitation reaction, and the latter by a gas-releasing, catalytic decomposition mechanism. Future studies that demonstrate prevention of MnO_2 precipitation accumulation or O_2 bubble formation will lead to a new generation of portable energy devices. VO_2^+ has fundamental physical limits on its maximum i_l (via its low D_O), limiting its use to vanadium redox batteries. These systems stand to benefit tremendously in terms of power density and energetic efficiency during rapid charge/discharge by switching from carbon to Au cathodes. ClO^- poisons its cathodes rapidly and is unlikely to serve in future fuel cells. At the moment, CAN was the best practical oxidant studied, as it provides such a high voltage that it compensates for its lower i_l, and operates free of troublesome passivation reactions.

5.5 Acknowledgments

The authors gratefully acknowledge support from the Office of Basic Energy Sciences, Division of Materials Sciences, U.S. Department of Energy, under Grant DE-FG02-05ER46250.

5.6 References

(1) Kakaç, S.; Pramuanjaroenkij, A.; Vasiliev, L. *Mini-Micro Fuel Cells: Fundamentals and Applications*; Springer: Dordrecht, The Netherlands, 2008.

(2) Ferrigno, R.; Stroock, A. D.; Clark, T. D.; Mayer, M.; Whitesides, G. M. *J. Am. Chem. Soc.* **2002**, *124*, 12930-12931.

(3) *CRC Handbook of Chemistry and Physics*; 90th ed.; Lide, D. R., Ed.; CRC Press: Boca Raton, FL, 2010.

(4) Jayashree, R. S.; Gancs, L.; Choban, E. R.; Primak, A.; Natarajan, D.; Markoski, L. J.; Kenis, P. J. A. *J. Am. Chem. Soc.* **2005**, *127*, 16758-16759.

(5) Mota, N. D.; Kirtland, J. D.; Finkelstein, D. A.; Rodriguez, C. A.; Stroock, A. D.; Abruña, H. D. *Submitted.* **2010**.

(6) Markovic, N. M.; Schmidt, T. J.; Stamenkovic, V.; Ross, P. N. *Fuel Cells (Weinheim, Ger.)* **2001**, *1*, 105-116.

(7) Hasegawa, S.; Shimotani, K.; Kishi, K.; Watanabe, H. *Electrochem. Solid-State Lett.* **2005**, *8*, A119-A121.

(8) Miley, G. H.; Luo, N.; Mather, J.; Burton, R.; Hawkins, G.; Gu, L.; Byrd, E.; Gimlin, R.; Shrestha, P. J.; Benavides, G.; Laystrom, J.; Carroll, D. *J. Power Sources* **2007**, *165*, 509-516.

(9) Ponce de León, C.; Walsh, F. C.; Rose, A.; Lakeman, J. B.; Browning, D. J.; Reeve, R. W. *J. Power Sources* **2007**, *164*, 441-448.

(10) Raman, R. K.; Prashant, S. K.; Shukla, A. K. *J. Power Sources* **2006**, *162*, 1073-1076.

(11) Vogel, W. M. *Electrochim. Acta* **1968**, *13*, 1821-1826.

(12) Kjeang, E.; Brolo, A. G.; Harrington, D. A.; Djilali, N.; Sinton, D. *J. Electrochem. Soc.*

2007, *154*, B1220-B1226.

(13) Gu, L.; Luo, N.; Miley, G. H. *J. Power Sources* **2007**, *173*, 77-85.

(14) Li, X.; Heryadi, D.; Gewirth, A. A. *Langmuir* **2005**, *21*, 9251-9259.

(15) Blizanac, B. B.; Lucas, C. A.; Gallagher, M. E.; Arenz, M.; Ross, P. N.; Markovic, N. M. *J. Phys. Chem. B* **2004**, *108*, 625-634.

(16) Prabhu, V. G.; Zarapkar, L. R.; Dhaneshwar, R. G. *Electrochim. Acta* **1981**, *26*, 725-729.

(17) Fetner, N.; Hudson, J. L. *J. Phys. Chem.* **1990**, *94*, 6506-6509.

(18) Matsuda, T.; Hommura, H.; Mukouyama, Y.; Yae, S.; Nakato, Y. *J. Electrochem. Soc.* **1997**, *144*, 1988-1994.

(19) Choban, E. R.; Markoski, L. J.; Wieckowski, A.; Kenis, P. J. A. *J. Power Sources* **2004**, *128*, 54-60.

(20) Sun, M. H.; Velve-Casquillas, G.; Guo, S. S.; Shi, J.; Ji, H.; Ouyang, Q.; Chen, Y. *Microelectron. Eng.* **2007**, *84*, 1182-1185.

(21) Licht, S.; Myung, N.; Peramupage, D. *J. Phys. Chem. B* **1998**, *102*, 6780-6786.

(22) Salloum, K. S.; Hayes, J. R.; Friesen, C. A.; Posner, J. D. *J. Power Sources* **2008**, *180*, 243-252.

(23) Lin, S. C.; Wang, Y. Y.; Wan, C. C.; Chang, J. C. *Bull. Chem. Soc. Jpn.* **1993**, *66*, 3372-3376.

(24) Schurig, H.; Heusler, K. E. *Z. Anal. Chem.* **1967**, *225*, 45-62.

(25) Ciavatta, L.; Grimaldi, M. *J. Inorg. Nucl. Chem.* **1969**, *31*, 3071-3082.

(26) Sekula-Brzezinska, K.; Wrona, P. K.; Galus, Z. *Electrochim. Acta* **1979**, *24*, 555-563.

(27) Freeman, D. B.; Mamantov, G. *Electrochim. Acta* **1976**, *21*, 257-261.

(28) Galus, Z.; Adams, R. N. *J. Phys. Chem.* **1963**, *67*, 866-871.

(29) Skyllas-Kazacos, M.; Rychcik, M.; Robins, R. G.; Fane, A. G. *J. Electrochem. Soc.* **1986**, *133*, 1057-1058.

(30) Skyllas-Kazacos, M.; Grossmith, F. *J. Electrochem. Soc.* **1987**, *134*, 2950-2953.

(31) Kjeang, E.; Proctor, B. T.; Brolo, A. G.; Harrington, D. A.; Djilali, N.; Sinton, D. *Electrochim. Acta* **2007**, *52*, 4942-4946.

(32) Rahman, F.; Skyllas-Kazacos, M. *J. Power Sources* **2009**, *189*, 1212-1219.

(33) Huang, K. L.; Li, X. G.; Liu, S. Q.; Tan, N.; Chen, L. Q. *Renewable Energy* **2008**, *33*, 186-192.

(34) Medeiros, M. G.; Dow, E. G. *J. Power Sources* **1999**, *80*, 78-82.

(35) Cardenas-Valencia, A. M.; Biver, C. J.; Langebrake, L. *J. Power Sources* **2007**, *166*, 273-283.

(36) Kjeang, E.; Michel, R.; Harrington, D. A.; Sinton, D.; Djilali, N. *Electrochim. Acta* **2008**, *54*, 698-705.

(37) Xu, X.; Jiang, R.; Zhou, X.; Liu, Y.; S.Ji; Zhang, Y. *Tetrahedron* **2009**, *877*.

(38) Noyes, A. A.; Garner, C. S. *J. Am. Chem. Soc.* **1936**, *58*, 1265-1268.

(39) Bonewitz, R. A.; Schmid, G. M. *J. Electrochem. Soc.* **1970**, *117*, 1367-1372.

(40) Pletcher, D.; Valdes, E. M. *Electrochim. Acta* **1988**, *33*, 499-507.

(41) Randle, T. H.; Kuhn, A. T. *J. Chem. Soc., Faraday Trans.* **1983**, *79*, 1741-1756.

(42) Hoare, J. P. *Electrochim. Acta* **1972**, *17*, 1907-1919.

(43) Liu, Y.; Xia, X.; Liu, H. *J. Power Sources* **2004**, *130*, 299-305.

(44) Kiekens, P.; Steen, L.; Donche, H.; Temmerman, E. *Electrochim. Acta* **1981**, *26*, 841-845.

(45) Ferro, S.; Battisti, A. D. *Phys. Chem. Chem. Phys.* **2002**, *4*, 1915-1920.

(46) Taylor, R. J.; Humffray, A. A. *J. Electroanal. Chem.* **1973**, *42*, 347-354.

(47) Kirtland, J. D.; McGraw, G. J.; Stroock, A. D. *Phys. Fluids* **2006**, *18*, 073602.

(48) Matsuda, H. *J. Electroanal. Chem.* **1967**, *15*, 325-336.

(49) Elbicki, J. M.; Morgan, D. M.; Weber, S. G. *Anal. Chem.* **1984**, *56*, 978-985.

(50) Bard, A. J.; Faulkner, L. R. *Electrochemical Methods*; 2nd ed.; John Wiley & Sons, Inc.: New York, NY, 2001.

(51) Cotton, F. A.; Wilkinson, G. *Advanced Inorganic Chemistry*; 4th ed.; Wiley: New York, NY, 1980.

(52) *Tables of Physical and Chemical Constants and Some Mathematical Functions*; 16th ed.; Kaye, G. W. C.; Laby, T. H., Eds.; Longman Group Ltd.: Harlow, Essex, UK, 1995.

(53) Greef, R.; Aulich, H. *J. Electroanal. Chem.* **1968**, *18*, 295-307.

(54) Vetter, K. J. *Z. Physik. Chem. (Leipzig)* **1951**, *196*, 360.

(55) Herbelin, J. M.; Andersen, T. N.; Eyring, H. *Electrochim. Acta* **1970**, *15*, 1455-1469.

(56) Petrocelli, J. V.; Paolucci, A. A. *J. Electrochem. Soc.* **1951**, *98*, 291-295.

(57) Paulenova, A.; Creager, S. E.; Navratil, J. D.; Wei, Y. *J. Power Sources* **2002**, *109*, 431-438.

(58) Sherrill, M. S.; King, C. B.; Spooner, R. C. *J. Am. Chem. Soc.* **1943**, *65*, 170-179.

(59) Rahman, F.; Skyllas-Kazacos, M. *J. Power Sources* **1998**, *72*, 105-110.

(60) Kjeang, E.; Michel, R.; Harrington, D. A.; Djilali, N.; Sinton, D. *J. Am. Chem. Soc.* **2008**, *130*, 4000-4006.

(61) Samad, M. A.; Kazacos, M.; Skyllas-Kazacos, M., Int. Pat. No. WO/1995/012219, Int. Pat. Appl. No. PCT/AU94/00711, 1994.

(62) Skyllas-Kazacos, M.; Peng, C.; Cheng, M. *Electrochem. Solid-State Lett.* **1999**, *2*, 121-

122.

(63) Zhong, S.; Skyllas-Kazacos, M. *J. Power Sources* **1992**, *39*, 1-9.

(64) Sum, E.; Rychcik, M.; Skyllas-Kazacos, M. *J. Power Sources* **1985**, *16*, 85-95.

(65) Gattrell, M.; Park, J.; MacDougall, B.; Apte, J.; McCarthy, S.; Wu, C. W. *J. Electrochem. Soc.* **2004**, *151*, A123-A130.

(66) Gattrell, M.; Qian, J.; Stewart, C.; Graham, P.; MacDougall, B. *Electrochim. Acta* **2005**, *51*, 395-407.

(67) Lingane, J. J. *J. Am. Chem. Soc.* **1945**, *67*, 182-188.

(68) Lingane, J. J.; Meites, L. *J. Am. Chem. Soc.* **1947**, *69*, 1882-1886.

(69) Ivakin, A. A.; Voronova, E. M. *Russ. J. Inorg. Chem.* **1973**, *18*, 956-958.

(70) Dzhabarov, F. Z.; Gorbachev, S. V. *Russ. J. Phys. Chem.* **1964**, *38*, 911-913.

(71) Anson, F. C.; King, D. M. *Anal. Chem.* **1962**, *34*, 362-365.

(72) Djordjevic, A. B.; Nikolic, B. Z.; Kadija, I. V.; Despic, A. R.; Jaksic, M. M. *Electrochim. Acta* **1973**, *18*, 465-471.

(73) Czarnetzki, L.; Janssen, L. J. J. *Electrochim. Acta* **1988**, *33*, 561-566.

5.7 Appendix: Derivation of Limiting Current Expression for a Laminar-Flow Fuel Cell

The following equations are taken and derived from Kirtland, J. D.; McGraw, G. J.; Stroock, A. D. *Phys. Fluids* **2006**, *18*, 073602. For a full explanation of the many variables used, please refer to this reference, as it falls outside the scope of our manuscript.

The equation notation used is Eq. # for an equation appearing in the main text, R.# for an equation from Kirtland et al. 2006, and A.# for all equations appearing in the appendix.

From Kirtland et al. 2006: We will let the axis of the primary fluid motion in the channel of a laminar-flow fuel cell be the z-axis. The Sherwood number as a function of position along the z-axis, *Sh*(z), is given as:

Eq. A.1, R.6

$$Sh(z) = -\frac{PeH}{C_{cup}(z)}\frac{dC_{cup}(z)}{dz} = -\frac{d\ln C_{cup}(z)}{d\dfrac{z}{PeH}}$$

For flows that are short compared to entrance length, or $z << PeH$:

Eq. A.2, R.14

$$Sh(z) = \frac{9^{-1/3}}{\Gamma\left(\dfrac{4}{3}\right)}\left(\frac{H\dot{\gamma}}{U}\right)^{1/3}\left(\frac{z}{PeH}\right)^{-1/3} = B_0\left(\frac{z}{PeH}\right)^{-1/3}$$

Combining Eq.'s A.1 into Eq. A.2, we have:

Eq. A.3

$$B_0\left(\frac{z}{PeH}\right)^{-1/3} = -\frac{d\ln C_{cup}(z)}{d\frac{z}{PeH}}$$

Eq. A.4

$$-B_0\left(\frac{z}{PeH}\right)^{-1/3} d\frac{z}{PeH} = d\ln C_{cup}(z)$$

Next, to assess the total amount of oxidant hitting the electrode along the length of the flow channel (L_{tot}), we integrate these terms along the z-axis for the entirety of the flow channel:

Eq. A.5

$$-B_0\int_{z=0}^{z=L_{tot}}\left(\frac{z}{PeH}\right)^{-1/3} d\frac{z}{PeH} = \int_{z=0}^{z=L_{tot}} d\ln C_{cup}(z)$$

Eq. A.6

$$-B_0\frac{3}{2}\left(\frac{z}{PeH}\right)^{2/3}\Bigg]_{z=0}^{z=L_{tot}} = \ln C_{cup}(z)\Big]_{z=0}^{z=L_{tot}} \qquad \text{OR} \qquad -B_0\frac{3}{2}\left(\frac{z}{PeH}\right)^{2/3}\Bigg|_{z=0}^{z=L_{tot}} = \ln C_{cup}(z)\Big|_{z=0}^{z=L_{tot}}$$

Eq. A.7

$$-B_0\frac{3}{2}\left(\frac{L_{tot}}{PeH}\right)^{2/3} + B_0\frac{3}{2}\left(\frac{0}{PeH}\right)^{2/3} = \ln C_{cup}(L_{tot}) - \ln C_{cup}(0)$$

Eq. A.8

$$-B_0 \frac{3}{2}\left(\frac{L_{tot}}{PeH}\right)^{2/3} = \ln\left(\frac{C_{cup}(L_{tot})}{C_{cup}(0)}\right)$$

Eq. A.9

$$\exp\left[-B_0 \frac{3}{2}\left(\frac{L_{tot}}{PeH}\right)^{2/3}\right] = \frac{C_{cup}(L_{tot})}{C_{cup}(0)}$$

In our case, B_0 = 1, since the channel is wider than it is deep (see Kirtland et al. 2006, text following Eq. R.14):

Eq. A.10

$$\exp\left[-\frac{3}{2}\left(\frac{L_{tot}}{PeH}\right)^{2/3}\right] = \frac{C_{cup}(L_{tot})}{C_{cup}(0)}$$

Kirtland et al. 2006 expresses ε as:

Eq. A.11, R.19

$$\varepsilon = 1 - \frac{C_{cup}(L_{tot})}{C_{cup}(0)}$$

Combining Eq.'s A.10 and A.11, we have:

Eq. A.12

$$\varepsilon = 1 - \exp\left[-\frac{3}{2}\left(\frac{L_{tot}}{PeH}\right)^{2/3}\right]$$

Kirtland et al. 2006 provides the expression for molar flow rate, $\dot{N}$ (in mol/s), as:

Eq. A.13, R.20

$$\dot{N} = \left[C_{cup}(0) - C_{cup}(L_{tot})\right]Q$$

Expressing *Pe* in the form $Pe = Q/(WD_O)$ and plugging in Eq. A.11, R.19, we have:

Eq. A.14

$$\dot{N} = C_{cup}(0)PeWD_O\varepsilon$$

We can convert to current by multiplying $\dot{N}$ by Faraday's constant and the number of electrons involved in the electrochemical reaction:

Eq. A.15

$$i_l = nF\dot{N}$$

Or, with $C_{cup}(0) = C_O^*$, and combining Eq.'s A.14 and A.15, we have:

Eq. A.16

$$i_{l,c} = nFC_O^*PeWD_O\varepsilon$$

Combining Eq.'s A.12 and A.16, and rearranging terms for similarity to relevant electrochemical equations, we have the following expression, we also appears in the main text as Equation 5.1.1:

Eq. 5.1.1, A.17

$$i_{l,c} = nFC_{\mathrm{O}}^{*}D_{\mathrm{O}}WPe\left(1-\exp\left[-\frac{3}{2}\left(\frac{L}{PeH}\right)^{2/3}\right]\right)$$

Using the Taylor expansion approximation: $e^{x} \sim 1 + x$, so $1 - e^{x} = -x$, we have:

Eq. A.18

$$i_{l,c} \sim \frac{3}{2}nFC_{\mathrm{O}}^{*}D_{\mathrm{O}}W\left(\frac{L}{H}\right)^{2/3}Pe^{1/3}$$

Again substituting in $Pe = Q/(WD_{\mathrm{O}})$, we have:

Eq. A.19

$$i_{l,c} \sim \frac{3}{2}nFC_{\mathrm{O}}^{*}W\left(\frac{1}{W}\right)^{1/3}D_{\mathrm{O}}\left(\frac{1}{D_{\mathrm{O}}}\right)^{1/3}\left(\frac{L}{H}\right)^{2/3}Q^{1/3}$$

Eq. A.20

$$i_{l,c} \sim \frac{3}{2}nFC_{\mathrm{O}}^{*}W^{2/3}D_{\mathrm{O}}^{2/3}\left(\frac{L}{H}\right)^{2/3}Q^{1/3}$$

Finally, we arrive at the expression used in the main text as Eq. 5.1.2:

Eq. 5.1.2, A.21

$$i_{l,c} \sim \frac{3}{2} nFC_{O}^{*} \left(\frac{D_{O} LW}{H} \right)^{2/3} Q^{1/3}$$

Chapter 6: Superior Oxidants for High-Power and Microfluidic Fuel Cells

Personnel: David A. Finkelstein, Héctor D. Abruña

Department of Chemistry and Chemical Biology, Baker Laboratory,

In Chapter 5, many alternative oxidants for high-power fuel cells were examined, but none were found to be ideal. One of our main conclusions was that maximizing current density was of utmost priority, and that *n* needed to be at least 2 in order for current densities to become significant Voltage is a secondary concern; in an aqueous system, there are strict limits on maximum voltage at common electrocatalysts, so voltage may vary 20-30% between oxidants. Current densities, however, were shown to vary by orders of magnitude. In this chapter, new oxidants with $n \geq 2$ are analyzed in detail, and some are shown to greatly improve maximum current density without introducing compromising side reactions.

6.1 Superior Oxidants Introduction:

From an array of known oxidant reduction reactions,[1] we chose those that we thought would be the most promising. Persulfate, $S_2O_8^{2-}$, has an exceptionally high potential for reduction, in addition to possessing the minimum $2e^-$ necessary for high current density (Table 6.1.1). Iodate, chromate, and dichromate were chosen because they undergo reductions involving $3e^-$ or more (Table 6.1.1), and so should provide even greater current densities. The RDE voltammograms for the various novel oxidants are shown alongside those for the previously employed oxidants in Figure 6.1.1, and the determined mass transport parameters are shown in Table 6.1.2.

Oxidant	Possible Reactions:	E^0 (V vs. Ag/AgCl)
O_2	$O_2 + 2H^+ + 2e^- \leftrightarrows H_2O_2$	0.498
	$O_2 + 4H^+ + 4e^- \leftrightarrows H_2O$	1.032
MnO_4^-	$MnO_4^- + e^- \leftrightarrows MnO_4^{2-}$	0.361
	$MnO_4^- + 4H^+ + 3e^- \leftrightarrows MnO_2 + 2H_2O$	1.482
	$MnO_4^- + 8H^+ + 5e^- \leftrightarrows Mn^{2+} + 4H_2O$	1.310
H_2O_2	$H_2O_2 + 2H^+ + 2e^- \leftrightarrows 2H_2O$	1.579
$Ce(NH_4)_2(NO_3)_6$	$Ce^{4+} + e^- \leftrightarrows Ce^{3+}$	1.523
VO_2^+	$VO_2^+ + 2H^+ + e^- \leftrightarrows VO^{2+} + H_2O$	0.794
	$VO^{2+} + 2H^+ + e^- \leftrightarrows V^{3+} + H_2O$	0.140
ClO^-	$HClO + H^+ + 2e^- \leftrightarrows Cl^- + H_2O$	1.285
	$HClO + H^+ + e^- \leftrightarrows ½Cl_2 + H_2O$	1.414
$S_2O_8^{2-}$	$S_2O_8^{2-} + 2H^+ + 2e^- \leftrightarrows 2HSO_4^-$	1.926
IO_3^-	$IO_3^- + 6H^+ + 6e^- \leftrightarrows I^- + 3H_2O$	0.888
IO_3^-	$IO_3^- + 6H^+ + 5e^- \leftrightarrows I_2 + 3H_2O$	0.998
$HCrO_4^-$	$HCrO_4^- + 7H^+ + 3e^- \leftrightarrows Cr^{3+} + 4H_2O$	1.153
$Cr_2O_7^{2-}$	$Cr_2O_7^{2-} + 14H^+ + 6e^- \leftrightarrows 2Cr^{3+} + 7H_2O$	1.035

Table 6.1.1: Reduction reactions for previously employed and novel oxidants.

	Oxidant	# of e^-	Diffusion Coefficient ($x10^{-5}$ cm^2/s)	Solubility (M)	Current Density[1] (mA/cm^2)	Complication
Previously Employed Oxidants *Increasing Current Density* ↑	$NaMnO_4$	5	1.2	7.3	560	Precipitation
	H_2O_2	2	1.5	42.4	220	Bubbles
	VO_2^+	1	0.25	< 3[2]	43	Reversible Poisoning at Au
	NaClO	1?	1.1	10.7	> 50	Irreversible Poisoning at Pt, Au, GC
	O_2	4	1.3	< 0.001	6.2	
Novel Fuel Cell Oxidants *Increasing Current Density* ↑	$Na_2Cr_2O_7$	6	0.8	7.1	540	Oscillations, Poisoning
	$NaIO_3$	5-6?	1.1	0.5	340	
	Na_2CrO_4	3	0.92	5.4	290	
	$Na_2S_2O_8$	2	0.6	2.3	150	
	CAN	1	0.42	2.6	57	

Table 6.1.2: Mass transport parameters relevant to current density for previously employed and novel oxidants.

[1] The mass-transport limited current density for 100 mM of the given oxidant at 3000 rpm is shown.
[2] VO_2^+ is typically generated from the precursor VO^{2+}, so the solubility for $VOSO_4$ is shown.

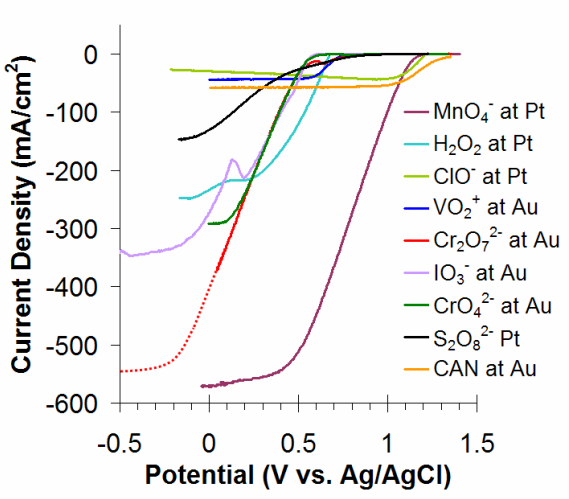

Figure 6.1.1: Metacomparison of old & new oxidants. RDE voltammograms for 100 mM oxidant at its best catalyst in 0.5 M H_2SO_4, rotated at 3000 rpm, are shown.

6.2 Persulfate ($S_2O_8^{2-}$)

With an E^0 of +1.926 V, $S_2O_8^{2-}$ had the highest standard potential of any oxidant studied, and combined with its $2e^-$ reaction (Table 6.1.1), it appeared very promising for delivering both voltage and current. However, like many of the compounds we studied (such as BH_4^- at Au, Section 3.3.2, and H_2O_2 at Pt, Section 5.3.2), the thermodynamics were not realized in an electrochemical setting. At Au in 0.1 M $HClO_4$, $S_2O_8^{2-}$ does not begin its reduction until +0.7 V (Figure 6.2.1), consistent with literature results,[2] and its reaction kinetics were rather slow at every pH, electrolyte, and catalyst studied.

Utilizing $S_2O_8^{2-}$ reduction is difficult, as it is thought to undergo a dissociative adsorption to form adsorbed SO_4^{2-} at Pt surfaces, and the adsorbed SO_4^{2-} blocks Pt for further reaction until SO_4^{2-} is removed at very low potential.[3,4] Our data supported this concept, showing mostly a self-poisoning peak at Pt (Figure 6.2.2). At potentials of +0.2 to +0.6 V, $S_2O_8^{2-}$ appears to show

well-behaved RDE reduction waves, but this is attributed to H_2O_2 produced by $S_2O_8^{2-}$ hydrolysis[5] (compare to H_2O_2 RDE voltammograms in Figure 5.3.2.1).

Some researchers have speculated that OH^- enhances $S_2O_8^{2-}$'s reduction reaction,[2,4] and our results confirmed that $S_2O_8^{2-}$ reduction will proceed to a mass-transport limited current at Pt in 1 M NaOH (Figure 6.2.3). Of course, switching from acidic to basic medium shifts pH dependent reactions negative by ~0.8 V (0.059 V per pH unit via the Nernst equation[6]), so the potential of the reduction becomes significantly less attractive using this approach. $S_2O_8^{2-}$ also shows reduction activity at GC in 1 M NaOH, although the performance is even lower than Pt's.

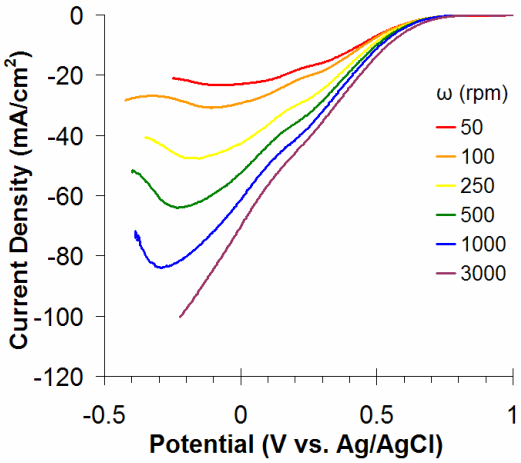

Figure 6.2.1: RDE voltammograms of 100 mM $S_2O_8^{2-}$ in 0.1 M $HClO_4$ at Au, cathodic sweeps, 20 mV/s.

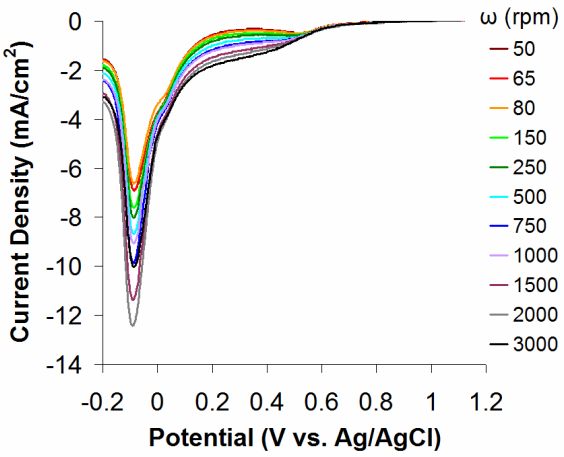

Figure 6.2.2: RDE voltammograms of 100 mM $S_2O_8^{2-}$ in 0.5 M H_2SO_4 at Pt, cathodic sweeps, 20 mV/s.

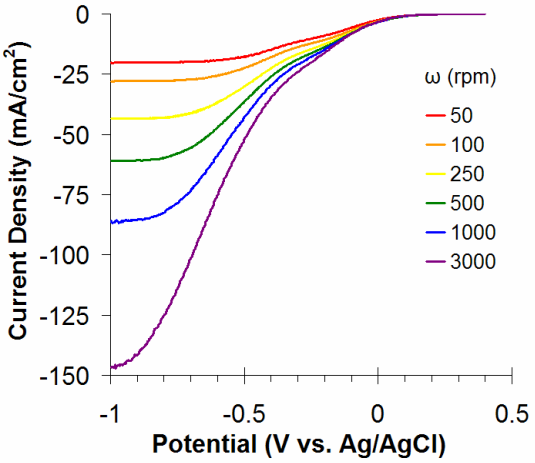

Figure 6.2.3: RDE voltammograms of 100 mM $S_2O_8^{2-}$ in 1 M NaOH at Pt, cathodic sweeps, 20 mV/s.

Despite these drawbacks, $S_2O_8^{2-}$, like CAN, did not appear to undergo any deleterious side reactions or poisoning at Au in acid, and can therefore find immediate utility in fuel cells. Though its onset potential for reduction was much lower than expected, it was still reasonably high, on par with H_2O_2 and O_2, and could produce significantly higher current than CAN (Figure

6.1.1). Many fuel cell researchers currently using H_2O_2, who are frustrated with O_2 bubble formation, can obtain trouble-free operation with only a moderate decrease in activity by switching to $S_2O_8^{2-}$, especially if low overpotentials are used.

6.3 Iodate (IO_3^-)

IO_3^- was a very attractive oxidant, with expected reductions involving 5 and $6e^-$ (Table 6.1.1). Indeed, IO_3^- produced the third-highest limiting current of any of the oxidants studied (0.35 A/cm^2, Figure 6.1.1; RDE voltammograms in Figure 6.3.1). Complications quickly arose, though, when assessing current delivered over time (Figure 6.3.2). Oscillatory behavior manifested, in which the reaction seemed to switch between the 5 and $6e^-$ processes. The Au electrode used would first turn dark, becoming covered with I_2, even though rotating at 3000rpm. Soon after, the thick layer of I_2 would dissipate, ejecting I_2 into solution, leaving behind a shiny Au surface. The process then repeated in a cyclical pattern for several minutes, while the overall current slowly diminished. A similar process has been described under galvanostatic conditions,[7] and may be akin to the Briggs-Rauscher "iodine clock" experiment often performed in undergraduate chemistry labs.

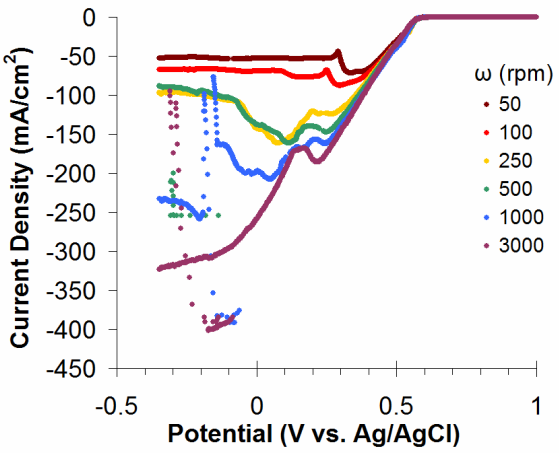

Figure 6.3.1: RDE voltammograms of 100 mM IO_3^- in 0.5 M H_2SO_4 at Au, cathodic sweeps, 20 mV/s.

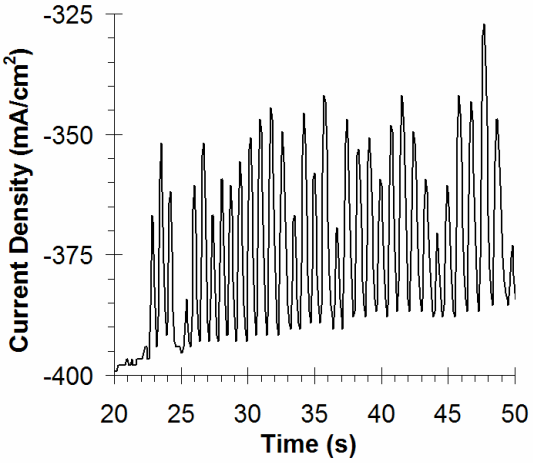

Figure 6.3.2: Oscillations evident for IO_3^- reduction at –0.35 V at Au. Current vs. time is shown for 100 mM IO_3^- in 0.5 M H_2SO_4, 3000 rpm.

Devising a fuel cell to function under such rapid variations in current may pose significant engineering challenges. It is possible that IO_3^- may not undergo such oscillations at higher potentials, or under conditions of kinetic, rather than mass transport control. We will continue to investigate this intriguing reaction, as the initial assessment of current density

indicated that, despite IO_3^-'s minimal solubility (Table 6.1.2), significant power densities could be achieved.

6.4 Chromate (CrO_4^{2-}) and Dichromate ($Cr_2O_7^{2-}$)

The highest-impact findings of our search through novel oxidant chemistries were, by far, the massive current densities afforded by the two chromium species, chromate, CrO_4^{2-}, and dichromate, $Cr_2O_7^{2-}$ (Figure 6.1.1). The activities (onset potential, kinetic rate of reaction, etc.) were identical, with the exception that $Cr_2O_7^{2-}$ produced about double the current density of CrO_4^{2-}, in accord with $Cr_2O_7^{2-}$'s doubled number of accepted electrons (6 vs. $3e^-$). $Cr_2O_7^{2-}$ is unique as an oxidant, possessing two transition metal atoms in the same molecule, doubling the current density at a given concentration while preserving the fast kinetics associated with transition metal electron transfers. Indeed, $Cr_2O_7^{2-}$'s kinetics are immeasurably fast by RDE methodology, with RDE voltammograms appearing as step functions instead of smooth waves (Figure 6.4.1).

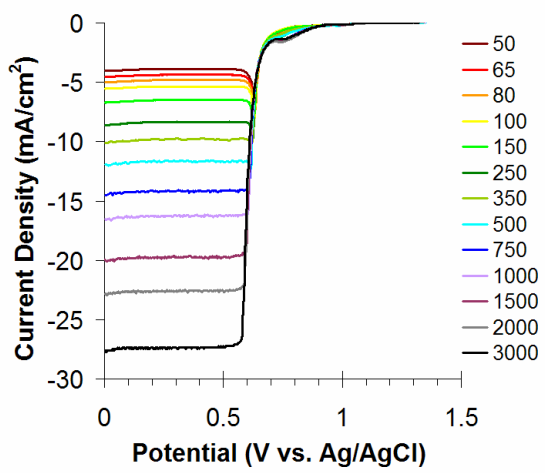

Figure 6.4.1: RDE voltammograms of 5 mM $Cr_2O_7^{2-}$ in 0.5 M H_2SO_4 at Au, cathodic sweeps, 20 mV/s.

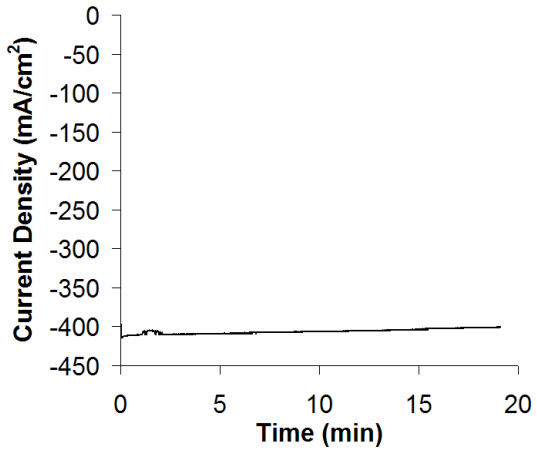

Figure 6.4.2: Poison-free reduction of 100 mM $Cr_2O_7^{2-}$ in 0.5 M H_2SO_4 at Au. Potential held at 0V vs. Ag/AgCl, 3000 rpm.

Like CAN, reduction of $Cr_2O_7^{2-}$ does not appear to have any poisoning or adverse side reactions, and we were able to observe sustained current densities > **0.4 A/cm^2**, specific surface area, for 20 min (Figure 6.4.2). The current was actually expected to be closer to 0.55 A/cm^2

(Figure 6.1.1, based on a 20 times increase in concentration from Figure 6.4.1), but resistances in the RDE cell did not permit the potentiostat to deliver this current at the working electrode. Because $Cr_2O_7^{2-}$ accepts 6 times the number of e^- as CAN, and has a diffusion coefficient about two times greater, its current density is nearly ten times greater (Figure 6.4.1 vs. Figure 5.3.4.1). Though current is significantly higher, $Cr_2O_7^{2-}$ manifests an onset potential about 0.5 V lower (less favorable) than CAN. When coupling to a low-potential fuel like BH_4^- (–1 V), however, this may represent a voltage drop of only about 20-30% for an order of magnitude gain in cathodic current.

In our search of novel oxidants, $Cr_2O_7^{2-}$ was the oxidant most comparable to MnO_4^-, providing a similar current density of ~**0.5 A/cm^2** at 0.1 M concentration (Figure 6.1.1) to match BH_4^-'s current density at just 0.05 M (Figure 1.2.2). Though $Cr_2O_7^{2-}$'s reduction does not begin until 0.5 V more negative (less favorable) than MnO_4^-'s, the reaction is free of poisoning and side reactions, allowing it to be implemented today without further investigation or development. Unlike CAN, $Cr_2O_7^{2-}$ is not expected to etch an Au electrode, since its onset potential for reduction is lower than the potential of Au oxide reduction. Thus, it should not oxidize Au to Au oxide, which would result in removal of oxygen-coordinated Au complexes from the electrode surface. Though we have not studied it as thoroughly in our fuel cell as CAN, as we discovered $Cr_2O_7^{2-}$ later in our oxidants search, our preliminary results are in agreement with our analytical RDE investigation, and we are continuing to study fuel cell operation at higher concentrations and power densities (see Chapter 8).

$Cr_2O_7^{2-}$ also shows activity at a number of other common electrode materials, many of them much less expensive than Au. However, $Cr_2O_7^{2-}$'s activity is highly catalyst dependent, suggesting that it undergoes a Marcus inner-sphere e^- transfer. $Cr_2O_7^{2-}$ is nearly unusable at Pt,

with an onset potential immediately positive of H_2 formation (Figure 6.4.3). $Cr_2O_7^{2-}$'s onset at GC is actually higher than it is at Au, but the kinetics are so slow that significant current is generated at potentials lower than –0.5 V (Figure 6.4.4). $Cr_2O_7^{2-}$ shows reasonable activity at Ag and Pd (Figures 6.4.5 and 6.4.6), although it seems to poison both materials rather quickly. Preliminary experiments indicate that step-cleaning may preserve activity at these materials. $Cr_2O_7^{2-}$ even shows activity at Ni, although Ni becomes covered by a passivating oxide layer at potentials positive of –0.1 V, so the reaction is only accessible at low (unfavorable) potentials (Figure 6.4.7). Nonetheless, $Cr_2O_7^{2-}$'s versatile activity across catalysts indicate that inexpensive metals, or alloys thereof, may serve as adequate catalysts, which could significantly decrease the cost of a $Cr_2O_7^{2-}$ fuel cell.

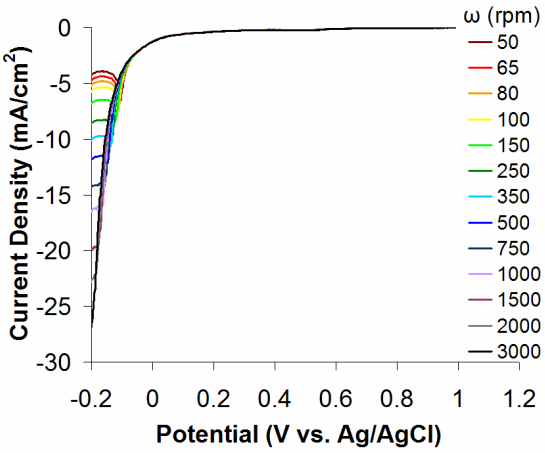

Figure 6.4.3: RDE voltammograms of 5 mM $Cr_2O_7^{2-}$ in 0.5 M H_2SO_4 at Pt, cathodic sweeps, 20 mV/s.

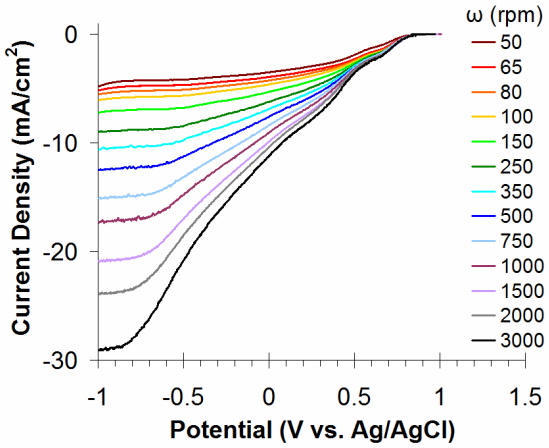

Figure 6.4.4: RDE voltammograms of 5 mM $Cr_2O_7^{2-}$ in 0.5 M H_2SO_4 at GC, cathodic sweeps, 20 mV/s.

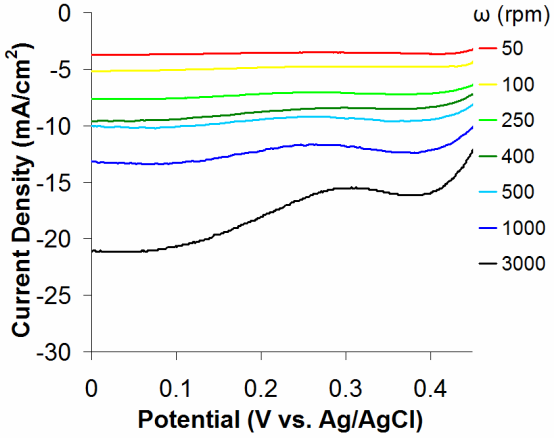

Figure 6.4.5: RDE voltammograms of 5 mM $Cr_2O_7^{2-}$ in 0.5 M H_2SO_4 at Ag, cathodic sweeps, 20 mV/s.

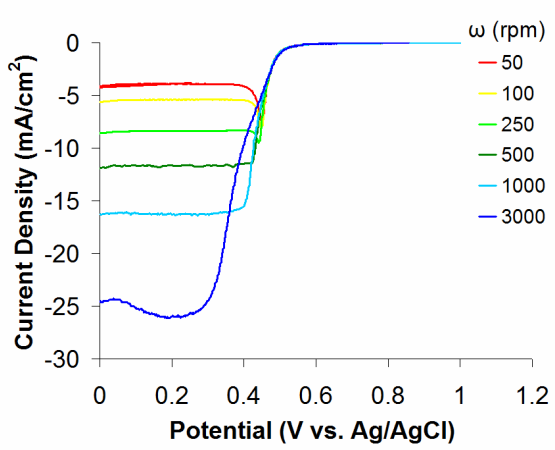

Figure 6.4.6: RDE voltammograms of 5 mM $Cr_2O_7^{2-}$ in 0.5 M H_2SO_4 at Pd, cathodic sweeps, 20 mV/s.

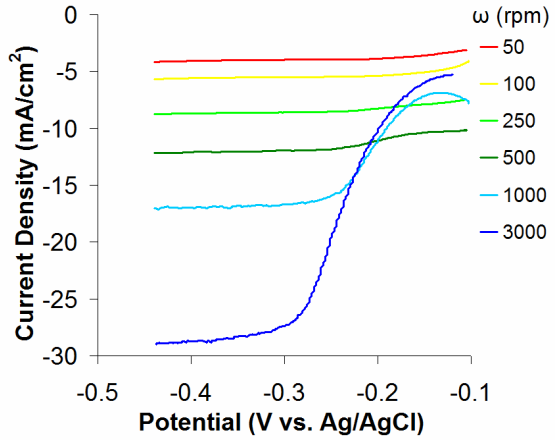

Figure 6.4.7: RDE voltammograms of 5 mM $Cr_2O_7^{2-}$ in 0.5 M H_2SO_4 at Ni, cathodic sweeps, 20 mV/s.

6.5 References

(1) *CRC Handbook of Chemistry and Physics*; 86th ed.; Lide, D. R., Ed.; CRC Press: Boca Raton, FL, 2005.

(2) Burke, L. D.; O'Sullivan, J. F.; O'Dwyer, K. J.; Scanell, R. A.; Ahern, M. J. G.; McCarthy, M. M. *Journal of the Electrochemical Society* **1990**, *137*, 2476-2481.

(3) Muller, L. *Journal of Electroanalytical Chemistry* **1967**, *13*, 275-279.

(4) Nakanishi, S.; Sakai, S. I.; Hatou, M.; Mukouyama, Y.; Nakato, Y. *Journal of Physical Chemistry B* **2002**, *106*, 2287-2293.

(5) Chu, W.; Lau, T. K.; Fung, S. C. *Journal of Agricultural and Food Chemistry* **2006**, *54*, 10047-10052.

(6) Bard, A. J.; Faulkner, L. R. *Electrochemical Methods*; 2nd ed.; John Wiley & Sons, Inc.: New York, NY, 2001.

(7) Radkov, E. V.; Ljutov, L. G. *Journal of Electroanalytical Chemistry* **1988**, *241*, 349-351.

Chapter 7: Membraneless, Room-Temperature, Direct Borohydride / Cerium Fuel Cell with Power Density Over 0.25 W/cm^2

Publication: *Submitted*

Personnel: Nicolas Da Mota[1], Joseph D. Kirtland[2], David A. Finkelstein[1], Claudia A. Rodriguez[1], Abraham D. Stroock[2], Héctor D. Abruña[1]

[1]Department of Chemistry and Chemical Biology, Baker Laboratory,
[2]Department of Chemical and Biomolecular Engineering, Olin Hall
Cornell University, Ithaca, New York 14853

The widespread adoption of fuel cells as an alternative energy technology has been held back by a number of formidable technical challenges. A microfluidic fuel cell is presented which overcomes many of these obstacles. The poisoning and sluggish reaction rate associated with methanol are averted by employing the promising, high-energy density fuel borohydride. The slow reaction of oxygen gas at the cathode is supplanted by the fast, high-voltage reduction of cerium ammonium nitrate. Expensive, ineffective membrane materials are entirely avoided via the use of laminar flow to separate fuel and oxidant streams. The result is a membraneless, room-temperature fuel cell with the highest power density yet recorded per unit mass of catalyst employed for a non-H_2 fuel cell, and has a power density that exceeds that a typical H_2 fuel cell by 50%.

7.1 Experimental Methods

7.1.1 Reagents

All chemicals used were reagent grade, and included $NaBH_4$ (Aldrich), $Ce(NO_3)_6(NH_4)_2$ (Fluka), NaOH (Mallinckrodt), and HNO_3 (EMD). All solutions were prepared with deionized water purified with a Hydro purification system connected in series to a Millipore Milli-Q system (18 MΩ•cm). The anolyte and catholyte were prepared by first deaerating 3 M NaOH and 1 M HNO_3, and subsequently adding 0.15 M $NaBH_4$ and 0.5 M $Ce(NO_3)_6(NH_4)_2$, respectively.

7.1.2 Fuel Cell Components and Operation Overview

The layered fuel cell consisted of a plexiglass jig, the anode, a layer of polydimethylsiloxane (PDMS) to define the anodic microfluidic channel, a polycarbonate (PC) separator, another layer of PDMS for the cathodic channel, the cathode, and an opposing plexiglass jig. Flat (laminar flow) electrodes were made by vapor deposition of metal onto Si wafers, whereas the staggered herringbone electrodes (chaotic flow) were made by first photolithographically etching a grooved pattern onto glass slides, and then coating the slide with vapor- and electro-deposited metal. Solutions were flowed through the microfluidic fuel cell via a multi-channel peristaltic pump (Ismatec IPC), ensuring balanced pressure in the anodic and cathodic chambers.

7.1.3 Fabrication of Fuel Cell Components

All fabrication was performed by Dr. Joseph Kirtland. The PC separator was cut from a 0.2 μm Isopore membrane filter (Millipore). The separator serves as a non-selective convection barrier, assisting in the establishment of laminar and chaotic flows, while allowing all chemical species to diffuse across.

The pattern for the PDMS mold prepared by spinning SU-8 (thickness ~110μm) on a silicon wafer and patterning with an EVG 620 contact aligner. The unexposed SU-8 was developed away to leave a pattern of 5 x 0.1 cm ridges on the silicon wafer. The surface of the master was functionalized with (tridecafluoro-1,1,2,2-tetrahydrooctyl) trichlorosilane (Gelest).

The PDMS was cast as a 0.2 mm thick sheet in the mold to specify 5 x 0.1 cm channel walls (for a 0.5 cm^2 exposed electrode area). The channel is open at the top and bottom to allow fluid contact to both the electrode and the PC separator, providing ionic conduction to the opposite fuel cell chamber. The PDMS was made using a Sylgard® 184 silicone elastomer kit (Dow Corning). Base and curing agent were mixed in a 10:1 ratio, then poured over the mold and all visible bubbles and dust were removed from the PDMS. A transparency was rolled onto the surface, with care taken not to generate bubbles at the PDMS transparency interface. A rigid glass plate (~2mm thick) was placed on the transparency and a large weight (~2kg) was placed on the glass plate such that the transparency was in contact with the top of the SU-8 pattern. In order to avoid problems due to thermal expansion, the PDMS was allowed to cure at room temperature for 3 h, then cured in an oven at 60°C for 12 h to make the gasket firmer and more easily handled.

Laminar flow electrodes were fabricated using electron-beam evaporation techniques (CVC SC4500 Combination Thermal/E-gun Evaporation System evaporation pressure ~$2x10^{-6}$

Torr, evaporation rate ~0.05 nm per second), which deposited both an adhesion layer of 5-10 nm Ti and a subsequent 95 nm layer of Pt onto Si wafers for the laminar-flow electrodes.

7.1.4 Photolithographic Etching of Fuel Cell Components

The staggered herringbone grooves of the chaotic electrodes were patterned onto glass by photolithography and etching with HF. The procedure began with borosilicate glass wafers, 100 mm dia. and 1.7 mm thick (Borofloat, Mark Optics), which were cleaned in buffered HF (6:1 ratio of 40% NH_4F to 50% HF) for 1.5 min, followed by treatment with hot piranha solution (3:1 H_2SO_4 to 30% H_2O_2) in an automated wafer processor (Hamatech HMR900). A hard mask of ~500 nm amorphous Si was deposited in a plasma-enhanced chemical vapor deposition system (IPE 1000 PECVD) at 200°C. Because the amorphous Si deposition is prone to forming particulates that can compromise the integrity of the film, the deposition was carried out in three steps, with both manual and plasma cleaning in-between steps. The completed film was annealed at 400°C on a hot plate for 2.5 h and allowed to cool. A photomask was patterned with the regions to be etched with a GCA Mann Pattern Generator. Photoresist 2.2 μm thick (Shipley 1818) was spun over the Si layer, patterned using the photomask and a contact aligner (EVG 620), and then developed in an automated wafer processor (Hamatech HMR900). The pattern was transferred to the Si film by SF_6 / O_2 reactive ion etch (RIE, Oxford 80). The wafer was then submerged in concentrated HF (50%) for 7.5 min to etch the glass through the pattern in the Si mask to a depth of 50 μm. The photoresist was stripped in acetone and the Si mask was stripped with the SF_6 / O_2 RIE (Oxford 80). The undercut associated with the HF etch generated narrow windows in the Si mask to produce nearly half-cylindrical grooves with quarter-spherical ends. Before metallization of the grooved glass, the buffered HF / piranha clean was repeated

followed by dehydration on a hot plate at 175°C for 5 min. An adhesion layer (10 nm Ti) and seed layer (50 nm Au) were vapor deposited onto the grooved glass using the same procedure as for the laminar flow elecrodes, followed by electroplating with ~4 um of Au to increase conductance and stability of the film. Finally, a top layer of 95 nm of Pt was vapor deposited to complete the chaotic flow electrodes.

Both laminar and chaotic flow electrodes were then coated with a protective layer of photoresist and diced to their final dimensions (1 cm by 7.5 cm) in a KS7100 wafer saw. Inlet and outlet holes were sandblasted through the electrode slides, and the photoresist was stripped in acetone.

7.2 Introduction

Practical implementation of fuel cells faces a number of challenges. The use of hydrogen is hindered by volumetric energy density and storage, while the use of methanol, a more dense fuel by volume, suffers from poisoning and poor kinetics at the anode, as well as membrane crossover and poisoning at the cathode.[1-4] Despite these complications with fuels, the power output of the majority of fuel cells is oxidant-limited, relying on the high-overpotential, kinetically slow reduction of O_2 at Pt.[1] The overwhelming majority of low-temperature fuel cells rely on a proton exchange membrane (PEM), and in practice, this material is almost exclusively Nafion®,[3-5] which outranks Pt as the most expensive component of the fuel cell.

7.3 Results and Discussion

7.3.1 The BH_4^- / CAN System and Laminar vs. Chaotic Flow

Here we present a fuel cell that addresses many of these limitations, resulting in an unprecedented power density for a non-H_2, room temperature fuel cell. A membraneless, microfluidic fuel cell based on a previous design[6,7] (see Section 7.1 for modifications) was used for evaluating the high-voltage redox pair, borohydride (BH_4^-) – cerium ammonium nitrate (CAN), and a transport-enhancing, chaotic-convective flow geometry.[8] The fuel and oxidant both exhibited rapid kinetics at Pt, allowing the fuel cell to be run at room temperature.[9,10] Maximal voltage was realized via asymmetric electrolytes, in which base was used to lower the potential of the fuel, and acid raised that of the oxidant. This unusual advantage was achieved only through the use of laminar flow to separate fuel and oxidant streams, as most fuel cells have comparatively stagnant flows, permitting electrolyte crossover and neutralization. Though laminar flow separation also resulted in limited transport to the anode and cathode, grooved electrodes were employed to create separate convection systems in the two streams, effecting much higher current and power densities (see Section 7.3.4).[8] While most room-temperature MeOH,[3] BH_4^-,[4] and microfluidic[11] fuel cells have power densities on the order of 50mW/cm^2 or less, our fuel cell generated 270 mW/cm^2, with 400 mA/cm^2 delivered at 0.65 V (Figure 7.3.1.1).

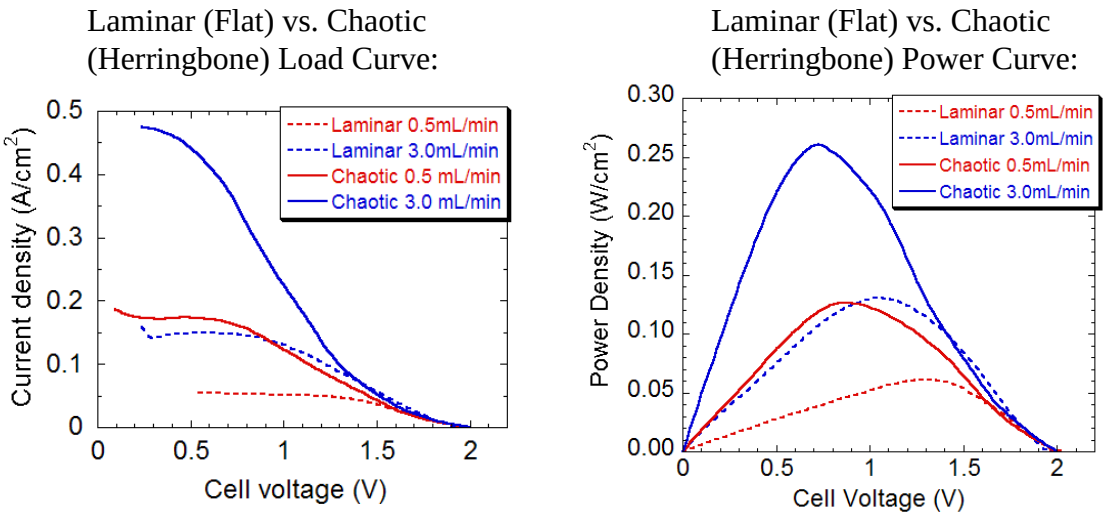

Figure 7.3.1.1: Load curves (left panel) and power curves (right panel) for fuel cell operation with 0.15 M $NaBH_4$ in 3 M NaOH and 0.5 M CAN in 1M HNO_3. Dotted lines show operation with flat, laminar-flow electrodes. Solid lines show operation with staggered-herringbone patterned, chaotic-convective electrodes, used to enhance transport of fuel and oxidant to the electrode via chaotic-convective flow.

7.3.2 Comparisons to Conventional Fuel Cell Systems

Comparisons between our system and other high-power fuel cells are difficult, largely because our electrodes are essentially flat (total area = geometric area), whereas in most reports, porous carbon supports with nanoparticulate catalysts are used to boost the microscopic electrode area to many times the geometric area. Power densities are then determined using only the geometric area. Comparing power generated per catalyst loading provides a very different assessment, especially since our vapor-deposited, 95nm thick Pt electrodes hold just 0.2 mg Pt/cm^2, on the order of an H_2 fuel cell,[12] while high-performing MeOH and BH_4^- fuel cells typically use 2-8 and 1-2 mg Pt/cm^2, respectively. The best MeOH fuel cells generate 2-30 mW/mg Pt, BH_4^- fuel cells 10-220 mW/mg catalyst (Pt, Pd, Ni, or Au), typical H_2 fuel cells

about 800 mW/mg,[13] and our fuel cell 1,230 mW/mg Pt (Figure 7.3.2.1). Additionally, MeOH and BH_4^- are typically employed at concentrations of 1.5-3 M, which is 10-20x our 0.15 M BH_4^-, and operating temperatures for the BH_4^- fuel cells are often 60°C or higher.[3,4] Several vanadium-based microfluidic fuel cells with similar current and power densities also used porous electrodes and 2M fuel, though they enjoyed the advantage of non-Pt, carbon catalysts.[14,15] Only specialty H_2 fuel cells exceed the power per catalyst loading presented here.[13]

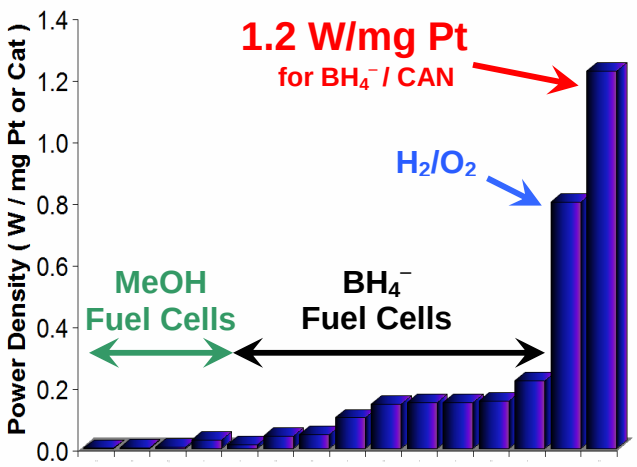

Figure 7.3.2.1: Specific power density normalized to weight of catalyst for BH_4^- / CAN fuel cell vs. other reported and common fuel cells.

It must be noted that the electrodes were only stable when they included a 4 μm layer of Au beneath the 95 nm Pt, which served to smooth out the rough edges of the herringbone pattern and prevent etching of Pt from the surface. However, this layer does not make contact with solution and is unnecessary for catalysis, and in fact would lower the power output of the fuel cell if exposed.[9] Efforts are underway to replace this layer with Cu so that Au does not add to the cost of these fuel cells.

7.3.3 Electrochemical Aspects of the BH_4^- / CAN System

Direct BH_4^- fuel cells are of great current interest due to BH_4^-'s theoretical yield of $8e^-$/molecule at –1.2V vs. NHE and lack of anode poisoning, but many investigations use Au rather than Pt anodes, resulting in significant system power loss,[9] and none have used CAN ($1e^-$ at 1.7 V vs. NHE) as an oxidant.[4] This fuel and oxidant pair is uniquely suited to the voltage-boosting, asymmetric electrolyte system employed, as BH_4^- is more stable in base and hydrolyzes to H_2 in acid,[16,17] while CAN is most soluble in nitric acid and precipitates as $Ce(OH)_4$[18] in base. Both fuel and oxidant begin their reactions at the practical limits of an aqueous system, with current onsets immediately positive of H_2 and negative of O_2 production, respectively, at Pt, for a practical maximum open-circuit voltage (OCV) of about 2.4 V for a pH 0 and 14 system.[9,10] Our system nearly realized this full potential, with observed OCV varying between 2-2.2 V. The fast kinetic processes translated a 0.5 V sacrifice in voltage to a gain in power of 75 mW/cm^2 (Figure 7.3.1.1).

Though the selected fuel and oxidant showed exceptional performance, several limitations in power density were noted. BH_4^-'s hydrolysis in bulk solution is first order with respect to $[BH_4^-]$,[16] so higher $[BH_4^-]$ required additional base to avoid excessive H_2 bubble formation, which disrupted both laminar and convective flow in the fuel cell. This resulted in a pratical limit of 0.15 M for $[BH_4^-]$. Plots of electrode potential vs. cell voltage (Figure 7.3.3.1) indicated that BH_4^- limited power output at higher voltages, so overall this restriction on $[BH_4^-]$ prevented higher power densities from being realized. We found that 0.5 M CAN in 1 M HNO_3 matched the fuel performance under these conditions. If higher $[BH_4^-]$ can be effected, CAN will eventually become limiting, as we found it to be soluble only to about 2.5 M. It must be noted that these low concentrations of fuel and oxidant translate to low volumetric energy

density for the system as a whole. Despite the observation that Au has greater CAN reduction kinetics than Pt,[10] Pt was employed as the cathode, as we found that CAN etched Au to black nanoparticles during high currents and prolonged operation.

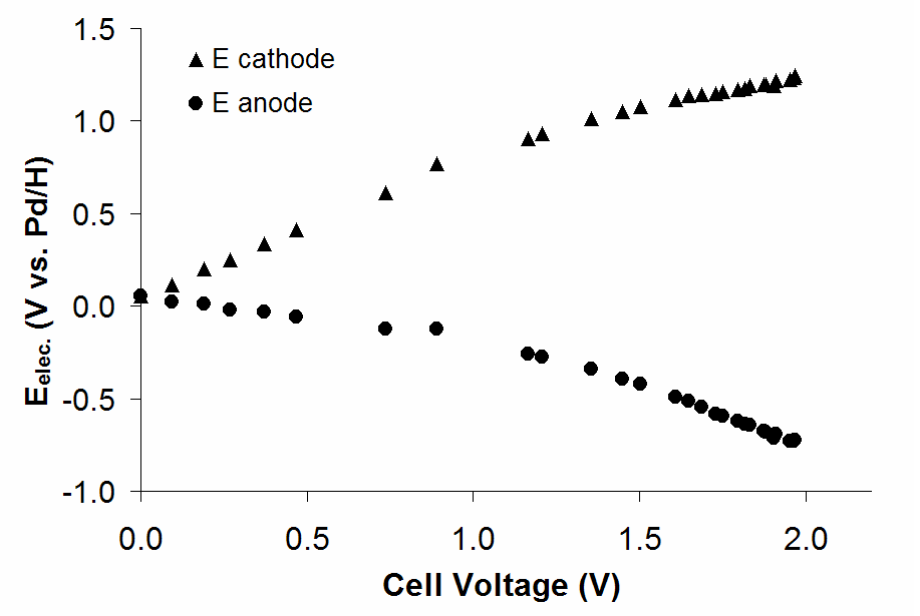

Figure 7.3.3.1: Plot of anode and cathode potentials vs. cell voltage during operation of the BH_4^- / CAN microfluidic fuel cell. Between a cell voltage of 2.0 and 1.0 V, the anode potential changes more dramatically than the cathode potential (sacrificing more potential to drive the corresponding electrode reaction), indicating that BH_4^- is more limiting than CAN in the high-power region of fuel cell operation.

7.3.4 Transport Enhancement via Chaotic (Convective) Flow

Employing a microfluidic, laminar flow system provides the exceptional advantage of fuel cell operation without a membrane,[19] as demonstrated by our group and other workers.[6,11] However, the layered fluid motion that separates fuel and oxidant streams also keeps unused

layers of fuel and oxidant from reaching the anode and cathode, respectively, and results in the lower current densities shown by the dotted lines in Figure 7.3.1.1, as well as lower fuel conversion efficiencies. To overcome this challenge, a staggered-herringbone pattern was imprinted onto the anode and cathode, causing the fuel and oxidant streams to separately convect, bringing unreacted fuel and oxidant to their respective electrodes without causing the two streams to mix,[8] as shown in Figure 7.3.4. Maximum current densities more than tripled, and maximum power doubled (Figure 7.3.1.1), consistent with simulations.[8]

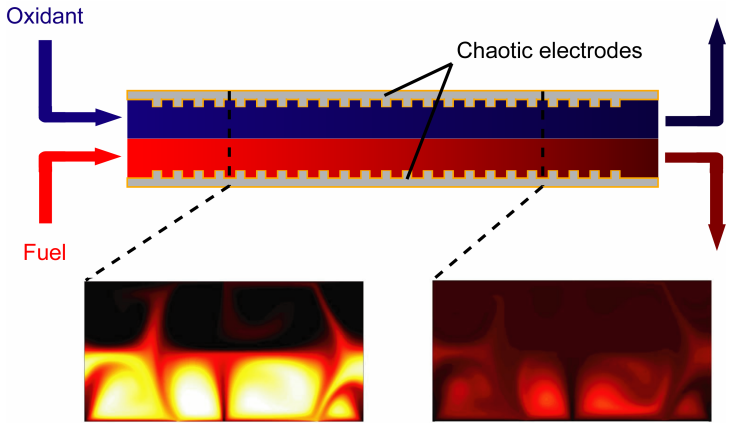

Figure 7.3.4.1: Visualization of theoretical, chaotic-convective flows using the staggered-herringbone electrodes, creating separate convection cells in the fuel and oxidant streams. Since the convective cells apply opposing forces, they deflect off one another (and the polycarbonate separator), preventing the two streams from mixing. Diffusion-limited transport is thus overcome by the disruption of laminar flow, adding a convective element to fuel and oxidant transport.

7.4 Conclusion

Our system represents a significant step forward in the development and understanding of fundamental electrochemistry and fluid mechanics essential to the establishment of practical fuel cells. By eliminating the PEM, avoiding sluggish anode kinetics and poisoning, preventing cathode poisoning from fuel crossover, replacing O_2 with a higher-power oxidant, and enhancing materials transport to the electrodes, the fuel cell presented here overcomes many of the existing challenges to fuel cell technology. The unprecedented power and current densities of about 0.25 W/cm^2 and 0.5 A/cm^2, respectively, were only achievable through the use of laminar flow to allow asymmetric fuel and oxidant electrolytes, and the use of staggered herringbone micromixers to enhance transport and efficiency. Though the Pt catalyst utilization was exceptionally high, the use of Au as a surface-smoothing underlayer needs to be eliminated to reduce total precious metal content. Overall power densities, efficiencies, and volumetric energy densities must still be addressed, and will likely require enhancing the stability of BH_4^- at high concentrations, finding a more soluble oxidant than CAN, and developing superior microfluidic transport.

7.5 Acknowledgments

The authors gratefully acknowledge support from the Office of Basic Energy Sciences, Division of Materials Sciences, U.S. Department of Energy, under Grant DE-FG02-05ER46250.

7.6 References

(1) Kakaç, S.; Pramuanjaroenkij, A.; Vasiliev, L. *Mini-Micro Fuel Cells: Fundamentals and Applications*; Springer: Dordrecht, The Netherlands, 2008.

(2) Kordesch, K.; Simader, G. *Fuel Cells and Their Applications*; Wiley-VCH: Weinheim, 1996.

(3) Dillon, R.; Srinivasan, S.; Aricò, A. S.; Antonucci, V. *Journal of Power Sources* **2004**, *127*, 112-126.

(4) Ma, J.; Choudhury, N. A.; Sahai, Y. *Renewable and Sustainable Energy Reviews* **2010**, *14*, 183-199.

(5) Jayashree, R. S.; Egas, D.; Spendelow, J. S.; Natarajan, D.; Markoski, L. J.; Kenis, P. J. A. *Electrochemical and Solid State Letters* **2006**, *9*, A252-A256.

(6) Cohen, J. L.; Westly, D. A.; Pechenik, A.; Abruña, H. D. *Journal of Power Sources* **2005**, *139*, 96-105.

(7) Cohen, J. L.; Volpe, D. J.; Westly, D. A.; Pechenik, A.; Abruña, H. D. *Langmuir* **2005**, *21*, 3544-3550.

(8) Kirtland, J. D.; McGraw, G. J.; Stroock, A. D. *Phys. Fluids* **2006**, *18*, 073602.

(9) Finkelstein, D. A.; Mota, N. D.; Cohen, J. L.; Abruña, H. D. *J. Phys. Chem.* **2009**, *113*, 19700-19712.

(10) Finkelstein, D. A.; Kirtland, J. D.; Mota, N. D.; Stroock, A. D.; Abruña, H. D. *Submitted* **2010**.

(11) Kjeang, E.; Djilali, N.; Sinton, D. *Journal of Power Sources* **2009**, *186*, 353-369.

(12) Winter, M.; Brodd, R. J. *Chem. Rev.* **2004**, *104*, 4245-4270.

(13) Taylor, A. D.; Lucas, B. D.; Guo, L. J.; Thompson, L. T. *Journal of Power Sources* **2007**, *171*, 218-223.

(14) Kjeang, E.; Michel, R.; Harrington, D. A.; Djilali, N.; Sinton, D. *J. Am. Chem. Soc.* **2008**, *130*, 4000-4006.

(15) Kjeang, E.; Proctor, B. T.; Brolo, A. G.; Harrington, D. A.; Djilali, N.; Sinton, D. *Electrochim. Acta* **2007**, *52*, 4942-4946.

(16) Morris, J. H.; Gysling, H. J.; Reed, D. *Chem. Rev.* **1985**, *85*, 51-76.

(17) Pecsok, R. L. *J. Am. Chem. Soc.* **1953**, *75*, 2862-2864.

(18) Sherrill, M. S.; King, C. B.; Spooner, R. C. *J. Am. Chem. Soc.* **1943**, *65*, 170-179.

(19) Morse, J. D. *Int. J. Energy Res.* **2007**, *31*, 576-602.

Chapter 8: The BH_4^- / $Cr_2O_7^{2-}$ Fuel cell

Personnel: David A. Finkelstein, Corey Letcher, Lori Sandberg, David Jones, David Watts, Héctor D. Abruña.

Department of Chemistry and Chemical Biology, Baker Laboratory,

In Chapter 7, the superior power density of a BH_4^- / CAN fuel cell relative to MeOH and H_2 fuel cells was discussed, yet in Chapter 5, it was determined that CAN is a relatively low current density oxidant. In this chapter, BH_4^- is paired with $Cr_2O_7^{2-}$, an oxidant with a current density an order of magnitude higher than CAN (Table 6.1.2). $Cr_2O_7^{2-}$ also offers over double CAN's solubility and faster kinetics, with its only apparent drawback being a decrease in voltage of 0.4 V (Figure 5.3.4.1 vs. Figure 6.4.1), or about 18% of open-circuit voltage (Figure 7.3.1.1). Additionally, this chapter examines long-term operation of a BH_4^- / $Cr_2O_7^{2-}$ fuel cell using an *in-situ* application of the pulse cleaning method described in Section 3.5. The preliminary results indicate that the BH_4^- / CAN system represents just a starting point for showcasing the possible energy storage and conversion properties of BH_4^-, and that the BH_4^- / $Cr_2O_7^{2-}$ system represents a higher power, higher energy application of BH_4^- fuel cell technology.

8.1 BH_4^- / $Cr_2O_7^{2-}$ Current and Power Densities

In the BH_4^- / $Cr_2O_7^{2-}$ fuel cell, fuel and oxidant are used at their best catalysts determined by analytical measurement, with Pt serving as the anode for BH_4^- (Section 3.3.5), and Au serving as the cathode for $Cr_2O_7^{2-}$ (Section 6.4). Initial studies of BH_4^- / $Cr_2O_7^{2-}$ ran into great difficulty, without production of well-behaved load or power curves. The concentration of $NaBH_4$ was dropped ten times from that studied with CAN,[1] to 0.015 M. $Na_2Cr_2O_7$ was used at a

concentration 60% below that proportionately expected from CAN (0.02 instead of 0.05 M), in a somewhat arbitrary manner; $Cr_2O_7^{2-}$ generates inherently higher current density but provides less voltage than CAN, so it was not immediately clear what concentration of $Cr_2O_7^{2-}$ would be optimal with the given amount of BH_4^-.

Individual load curves for the fuel and oxidant (half-cell studies) at these concentrations were performed to confirm which would serve as the limiting reagent. BH_4^- produced up to about 80 mA/cm^2 at 4 mL/min (Figure 8.1.1), while $Cr_2O_7^{2-}$ generated >100 mA/cm^2 (Figure 8.1.2). Thus, it was clear that BH_4^- would inevitably become limiting at higher currents and lower voltages in the fuel cell.

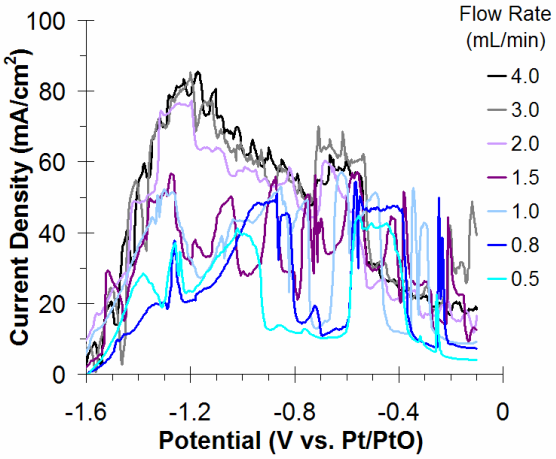

Figure 8.1.1: Fuel load curves for a laminar-flow fuel cell run in half-cell configuration using a Pt/PtO pseudoreference electrode. The fuel is 0.015 M $NaBH_4$ in 3 M NaOH at Pt, convected at the flow rates indicated.

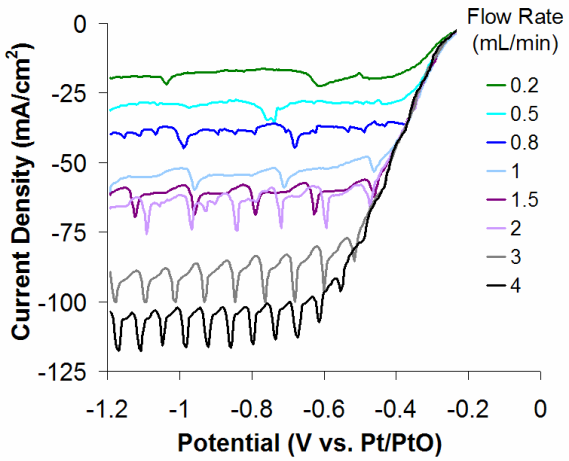

Figure 8.1.2: Oxidant load curves for a laminar-flow fuel cell run in half-cell configuration using a Pt/PtO pseudoreference electrode. The oxidant is 0.02 M $Na_2Cr_2O_7$ in 0.5 M H_2SO_4 at Au, convected at the flow rates indicated.

The overall fuel cell load curve, which reflects a mixture between the individual anodic and cathodic load curves, achieved a current density of only about 60 mA/cm^2 at 4 mL/min (Figure 8.1.3). This is somewhat below what was expected based on the individual load curves, but importantly, the overall load curve precisely mirrored the analytical RDE voltammogram for BH_4^- (Figure 3.3.6.1.a), supporting the earlier conclusion that BH_4^- would serve as the limiting reagent. Observing the entire BH_4^- voltammogram, including the low-potential region at Pt hydrides and the high-potential region at Pt surface oxide, is critical to the operation of the fuel cell. This indicates that BH_4^- is so much more limiting than $Cr_2O_7^{2-}$ that $Cr_2O_7^{2-}$ can bring Pt to the positive end of its oxide region, and clean off any adsorbed, poisoning boron species that have accumulated,[2] which is the basis of the pulse-cleaning method (Section 3.5). It is notable that because this cleaning method utilizes the oxidizing ability of the oxidant at the cathode *in-situ* to clean the anode, the fuel cell as a whole is self-cleansing, without requiring any outside energy input for the cleaning step.

The fuel cell performance, providing a maximum current of ~55 mA/cm^2 and 50 mW/cm^2 at 1 V and 3 mL/min (Figures 8.1.3 and 8.1.4) is very impressive. If this performance scaled proportionately when increasing [$NaBH_4$] to 0.15 M and [$Na_2Cr_2O_7$] to 0.2 M, it would be expected to produce **0.6 A/cm^2** and **0.5 W/cm^2**, under *laminar flow alone*. In contrast, the BH_4^- / CAN system delivered just 0.15 A/cm^2 and 0.125 W/cm^2 at 1 V under identical flow conditions, using 2.5 times more oxidant (Figure 7.3.1.1). In fact, under laminar flow, the BH_4^- / $Cr_2O_7^{2-}$ system is expected to deliver approximately double the power density of BH_4^- / CAN using the chaotic mixers. If chaotic mixing were applied to BH_4^- / $Cr_2O_7^{2-}$, a power density exceeding 1 W/cm^2 and approaching 5 W/mg Pt (based on Figure 7.3.2.1) would become feasible, and for just 0.15 M fuel. This would be a truly unprecedented power density and Pt utilization, well beyond that established for H_2 / O_2 fuel cells[3] and multiple orders of magnitude beyond that demonstrated for a MeOH fuel cell.[4] It is also a significant step forward for the Abruña group, as previous laminar flow fuel cells based on 0.5 M formic acid delivered <0.1 mW/cm^2.[5] More testing is required to realize this power density, and a system redesign is likely necessary to minimize the impact of small resistances, which will undoubtedly be magnified at such large current densities.

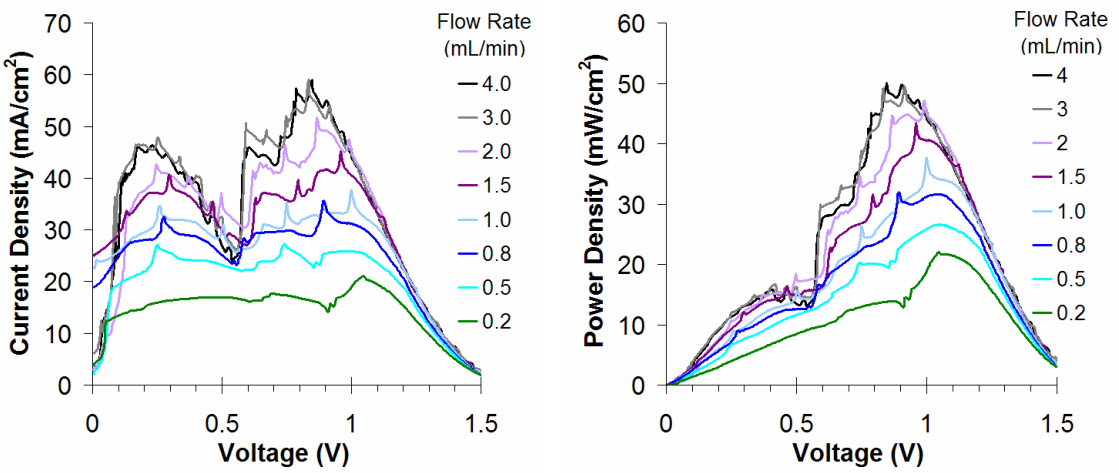

Figures 8.1.3 and 8.1.4: Load curves and power curves for a laminar-flow fuel cell using 0.015 M $NaBH_4$ in 3 M NaOH at Pt as fuel, and 0.02 M $Na_2Cr_2O_7$ in 0.5 M H_2SO_4 at Au as oxidant.

8.2 BH_4^- / $Cr_2O_7^{2-}$ Performance with Pulse-Cleaning

Though the projected available power densities from BH_4^- / $Cr_2O_7^{2-}$ system are considerable, they will not play a role in future energy systems if BH_4^- poisoning cannot be mitigated. A BH_4^- / $Cr_2O_7^{2-}$ fuel cell at the lower concentrations of 0.015 M $NaBH_4$ and 0.02 M $Na_2Cr_2O_7$ was operated using the pulse cleaning method described in Section 3.5. The fuel cell was operated at 0.9 V for 120 s, and brought close to short-circuit current at nearly 0 V for 5 s to clean. As described above in Section 8.1, this was expected to bring Pt to a potential of Pt oxide formation and remove any adsorbed boron species, cleaning the electrode. Figure 8.2.1 shows how the pulse cleaning appears during the operation of the fuel cell with a high-precision peristaltic pump. The current produced has a number of small spike-like decreases, which correspond to decreases in the flow rate for each pulsation from the peristaltic pump. The larger decreases in current, where the current drops to nearly 0 mA/cm^2, reflect the pulse-cleaning steps that bring the fuel cell to nearly 0 V. For this system, low voltage actually results in near zero

current (Figure 8.1.3), since BH_4^- oxidation is inactive at Pt oxides. In general, the current produced in Figure 8.2.1. slowly drops from about 38 mA/cm^2 to 35 mA/cm^2 during operation, but is then fully restored by the cleaning step.

In this mode of pulse cleaning, stable fuel cell operation for greater than 7 h was observed (Figure 8.2.2). In fact, current increased during the first 2 h of operation, likely because the Pt anode became cleaner during operation. The gradual decrease in current over the last 5 h of operation is probably attributable to the bulk hydrolysis in the prepared solution of BH_4^- used as fuel, as this is an expected time-dependent process.[6] Electrode poisoning from adsorbed compounds is typically much faster than this slow decay, occurring over a time scale of minutes rather than hours, as seen in Figure 8.2.1.

It is also significant that this fuel cell operated completely trouble-free from H_2 bubble formation at the Pt anode, supporting previous analytical findings that hydrolysis at a Pt surface occurs only in the high-potential region for oxidation, rather than the low-potential region of surface hydrides (Sections 3.3.5 and 3.3.6).[2] Hydrolysis-free operation of a BH_4^- fuel cell using a Pt anode is, as of the time of this writing, unprecedented in the BH_4^- literature.

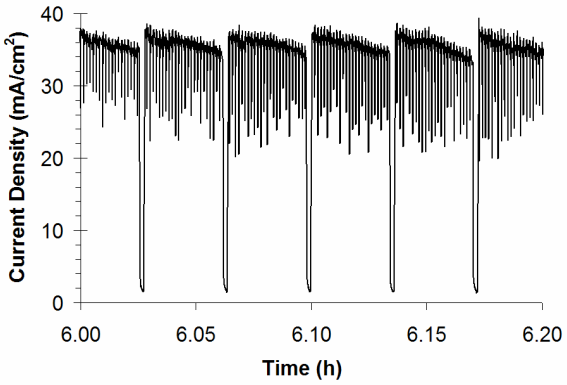

Figure 8.2.1: Current vs. time for a BH_4^- / $Cr_2O_7^{2-}$ fuel cell under pulse cleaning to Pt oxide region. Fuel cell run at 0.9 V for 120 s, cleaned for 5 s for each cycle. Solutions as described in Figure 8.1.3.

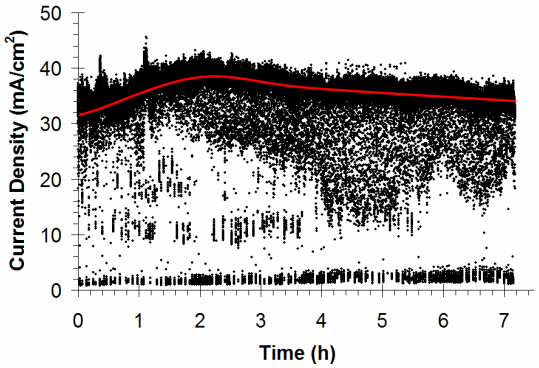

Figure 8.2.2: Current vs. time for a BH_4^- / $Cr_2O_7^{2-}$ fuel cell under pulse cleaning to Pt oxide region, demonstrating continuous operation for >7 h. The fuel cell was run at 0.9 V for 120 s and cleaned for 5 s in each cycle. Fuel and oxidant solutions are as described in Figure 8.1.3.

The BH_4^- / $Cr_2O_7^{2-}$ system appears to hold significant promise as a future energy system, and has only begun to be explored. Operation at concentrations approaching the solubility limit for $NaBH_4$, 15 M, or $Na_2Cr_2O_7$, 7 M,[7] will become necessary to avoid excessive water weight in the device design. Improved fuel cell designs will be necessary to overcome the <10% efficiency seen in the laminar-flow fuel cell design, which is the case even under chaotic mixing. Additionally, BH_4^- is currently synthesized from Na metal under high pressure,[8] which is unfavorable from an energy storage perspective. A "redox flow battery," or reversible fuel cell, would be a much more favorable system, but it is unclear if any reversible reactions exist that involve the 6 to 8 e^- necessary to produce the high power densities described here. Fortunately, both BH_4^- and $Cr_2O_7^{2-}$ show significant activity at less precious metals than Pt and Au, offering an important cost flexibility that does not currently exist for H_2 or MeOH fuel cells. Research on BH_4^- fuel cells will undoubtedly offer faster gains in cost and performance compared to the current alternatives.

8.3 References

(1) Mota, N. D.; Kirtland, J. D.; Finkelstein, D. A.; Rodriguez, C. A.; Stroock, A. D.; Abruña, H. D. *Submitted.* **2011**.

(2) Finkelstein, D. A.; Mota, N. D.; Cohen, J. L.; Abruña, H. D. *Journal of Physical Chemistry* **2009**, *113*, 19700-19712.

(3) Taylor, A. D.; Lucas, B. D.; Guo, L. J.; Thompson, L. T. *Journal of Power Sources* **2007**, *171*, 218-223.

(4) Dillon, R.; Srinivasan, S.; Aricò, A. S.; Antonucci, V. *Journal of Power Sources* **2004**, *127*, 112-126.

(5) Cohen, J. L.; Westly, D. A.; Pechenik, A.; Abruña, H. D. *Journal of Power Sources* **2005**, *139*, 96-105.

(6) Pecsok, R. L. *Journal of the American Chemical Society* **1953**, *75*, 2862-2864.

(7) *CRC Handbook of Chemistry and Physics*; 86th ed.; Lide, D. R., Ed.; CRC Press: Boca Raton, FL, 2005.

(8) Kakaç, S.; Pramuanjaroenkij, A.; Vasiliev, L. *Mini-Micro Fuel Cells: Fundamentals and Applications*; Springer: Dordrecht, The Netherlands, 2008.